From Subduction to Collision: Results from Seismic Profiling, Gravity Modeling, and Earthquake Finite Fault Inversions in Taiwan Region

by

Wu-Cheng Chi

B.S. (Chinese Cultural University) 1991

M.S. (San Jose State University) 1995

A dissertation submitted in partial satisfaction of the

requirements for the degree of

Doctor of Philosophy

in

Geophysics

in the

GRADUATE DIVISION

of the

UNIVERSITY OF CALIFORNIA, BERKELEY

Committee in charge:

Professor Douglas Dreger, Chair

Professor Roland Bürgmann

Professor James Rector, Jr

Professor Donald L. Reed

Spring 2003

The dissertation of Wu-Cheng Chi is approved:

Chair	Date
	Date
	Date
	Date

University of California, Berkeley

Spring 2003

From Subduction to Collision: Results from Seismic Profiling, Gravity Modeling, and Earthquake Finite Fault Inversions in Taiwan Region

By

Wu-Cheng Chi

Abstract

From Subduction to Collision: Results from Seismic Profiling, Gravity Modeling, and Earthquake Finite Fault Inversions in Taiwan Region

By

Wu-Cheng Chi

Doctor of Philosophy in Geophysics

University of California, Berkeley

Professor Douglas Dreger, Chair

This study used (1) 132-channel reflection profiles, forward gravity modeling, and (2) finite source inversions of earthquakes to analyze crustal evolution from subduction to collision in the region of Taiwan. Reflection and gravity data in the offshore region shows that the accretionary prism in the subduction zone is mainly sedimentary; however, due to tectonic wedging in the initial collision zone, high-density basement materials are incorporated into the rear of the accretionary prism and may extend northward to compose a portion of high-density rocks that underly southeastern Taiwan.

Further to the north in the mature collision zone was the site of the 1999, Chi-Chi, Taiwan earthquake. For this earthquake and its large aftershocks, we inverted strong motion data for finite source processes to study the deep fault structures. The mainshock ruptured on a shallow eastward-dipping fault possibly rooted in the proposed decollement of thin-skin deformation model. Several aftershocks either nucleated in or ruptured the basement indicating active deformation below the decollement, suggesting basement-

involved deformation.

Interpreting finite-source results requires a thorough understanding of the uncertainty in the parameters. Further more, near-realtime applications of finite-source inversions for estimation of near-fault strong ground motion requires well constrained fault orientation and hypocentral parameters. With this in mind, we tested a wide range of hypocenters and focal mechanisms, and the corresponding fits of the synthetics to the observed waveforms when studying the aftershock source parameters. As a result, we obtained optimal waveform fits and determined how the errors reported in hypocenters and focal mechanisms affected the inverted waveforms and the sensitivity of the waveform fits. For example, if the hypocenter was within 5 km of the optimal hypocenter and the focal mechanism was within 20 degrees of optimal strike, dip, and rake, the waveform fits deteriorated less than 20-percent.

For GPS stations near the aftershock region, the GPS displacements predicted from the aftershock slip models can explain 80-percent of the post Chi-Chi mainshock GPS signals, showing that care must be exercised when interpreting post-seismic deformation signals when there are numerous, moderate-sized aftershocks, and/or aftershocks that are shallow.

Table of Contents

Acknowledgements

I want to thank Dr. Douglas Dreger for his guidance. A Ph.D. student is inspired when he sees how his advisor makes things happen in such a positive way that the student will benefit from these experiences. I want to thank Dr. Donald L. Reed for showing me how to seek the life that I really wanted. I have learned so much by working with him in front of a computer and out at sea. He reminds me of what Gibran said: "The teacher who walks in the shadow of the temple, … gives not of his wisdom but rather of his faith and his lovingness." I am grateful to Dr. Anastasia Kaverina and Dr. Peggy Hellweg. They have taught me science and at a same time, have been my friends through my good times and bad. I am fortunate to have been given the opportunity to go with the geomorphology group to do field work in Taiwan following the Chi-Chi earthquake. That was one of my greatest moments as a graduate student at Berkeley. Dr. Mark Richards is thanked for his help. I want to thank Drs. Barbara Romanowicz, James Rector, Roland Bürgmann, and Lane Johnson for providing an excellent learning environment for students. Dr. Chi-Yuen Wang is thanked for his help during my studies. I want to thank Dr. Greg Moore for teaching me ProMAX and sharing the Hawaiian beach, Dr. Char-Shine Liu for his guidance, Dr. Honn Kao for showing me a vision, Dr. John Wakabayashi for talking science passionately with me. I am honored to have worked with the following researchers, staff, and students: Dr. Bob Uhrhammer, Dr. Lind Gee, Dr. Mark Murray, Charley Paffenbarger, Doug Neuhauser, Dr. David Schmidt, David Dolenc, Dr. Christiane Stidham, Dennis Templton, Dr. Janine Webber-Band, Christina Jordan, Rick McKenzie, Adam Underwood, Ling Kong, Yuen-Cheng Gung,

Sierra Boyd, Junkee Rhie, Matt D'Alssio, Mark Panning, Akiko To, Albert To, Andre Basset, Dr. Hrvoje Tkalcic and Aimin Cao.

I want to share my degree with Ching-Yen Chu, my lovely wife. She has always been there for me, which is a hard thing to do sometimes. Katrina Chi, my daughter, is thanked for being such a cute girl during the writing of this dissertation. The George family have been great for the last 11 years and I thank them for providing a home away from home. I want to thank my Mom for her love. She has sacrificed so much so I could get this far.

The publishers of Bull. Seism. Soc. Am. and Geophys. Res. Lett. are thanked for granting me the permissions to include our published manuscripts in chapter 3 and chapter 4.

Chapter 1

Introduction

Taiwan, located in one of the most active mountain belts in the world, is an excellent natural laboratory for studying tectonic processes. Due to the dense population of this seismically active island, the Taiwanese government has initiated several large-scale geological and geophysical projects so that they can better understand the regional tectonics and help mitigate seismic hazards. As a result, several geophysical datasets, which are noteworthy in their size and scope, have been collected over the past decade. We have analyzed two datasets (1) 2400 line-kilometers of marine geophysical data and (2) the strong motion waveform data of the 1999 Chi-Chi, Taiwan earthquake sequence recorded on a state-of-the-art seismic network (Figure 1.1) to study the deep crustal structures both in the subduction zone offshore and the arc-continent collision zone on land (Figure 1.1).

South of Taiwan, the oceanic lithosphere of the South China Sea, which is part of the Eurasian plate, is subducting beneath the oceanic lithosphere of the Philippine Sea plate. At Taiwan, the Eurasian plate carries the thicker crust of the Chinese passive margin into the convergent boundary with the Philippine Sea plate and subduction changes into arc-continent collision. Due to the oblique angle between the edge of the passive margin and the convergent boundary, the NW-SE relative plate motion to the northwest causes the contact between the ocean-continent boundary and the convergent

boundary to migrate southward along the convergent boundary at rates estimated to be from 84 mm/yr (Suppe, 1981), 96 mm/yr (Byrne, 1998), to 102 mm/yr (Lundberg et al., 1997). This geometry makes it possible to apply the concept of time-space equivalence to Taiwan (Suppe, 1984), allowing studies of the evolution of crustal structures from the younger stage in the south to the mature stage in the north.

In the 1980s, oil companies made available a vast amount of on-land reflection and well-logging data that were used to develop the critical taper model of Suppe (1981) and Davis et al. (1983). In their model, the mountain building process is described by analogy as a pile of sand being pushed by a bulldozer (Figure 1.2). The angle between the topographic slope and the decollement, the major shallow-dipping detachment fault that separates the overriding plate from the rigid, down-going plate, is called the taper angle, and is modeled as a function of material strength and pore-fluid-pressure on the decollement. This model has provided an enormously successful way of studying geodynamic process quantitatively, assuming a rigid downgoing plate without much basement-involved deformation (e.g. Malavieille et al., 2002). On the other hand, tomographic studies of Taiwan by Rau and Wu (1995) show that the Moho depth under Taiwan can reach at least 40 km; they interpreted this to mean that the basement has been internally deformed and thickened. These so-called thin-skinned and thick-skinned models of convergent deformation are the matter of much debate. In this study, we tested these models with seismologic data using active and passive sources, and other geologic and geophysical data to interpret crustal structures found at depths ranging from 0 to 30 km.

We have processed and interpreted the multi-channel seismic reflection data collected with the R/V Maurice Ewing of Columbia University. A transect across the rear of the accretionary prism in the initial collision zone (EW9509.49) showed evidence of tectonic wedging, supporting a previous interpretation of Reed et al. (1992). We performed seismic stratigraphic analyses on the sedimentary strata above the tectonic wedge to infer possible deformation within the wedge. Interpretations of multichannel seismic data were used to constrain a 2-D crustal density model that is consistent with the observed free-air gravity anomaly in the region. Results from more than 350 sensitivity tests show evidence of high-density material within the tectonic wedge. Gravity modeling on a transect further south in the subduction zone, using a seismic profile reprocessed by Nguyen et al. (1998) as a constraint, shows a low-density accretionary prism. These results suggest that the prism is mostly composed of sedimentary materials, including the region of tectonic wedging along the rear of the prism. As the collision process becomes more mature, blind thrusts incorporate both forearc sediment and high-density basement material into the tectonic wedge.

In 1996, Taiwan launched an ambitious program to set up a very dense strong motion network. In total, more than 600 strong motion stations were installed in a region comparable in size to the greater Bay Area in California. As a result, the 1999 Chi-Chi, Taiwan earthquake and its aftershocks were well-recorded; providing an opportunity for studying the earthquake source processes from Mw=5.8 to Mw=7.6. The finite fault inversions of the mainshock show that it ruptured a shallow dipping plane possibly

rooting into the decollement, consistent with the thin-skinned model. For the finite fault inversions of the aftershocks, more than 1000 sensitivity tests were performed using a wide rage of hypocenter and focal parameters to derive an optimal slip model for each event. A preferred slip model from one of the large aftershocks gives a shallow-dipping fault plane attitude that is consistent with the interpretations of the deep reflection data in that region (Wang et al., 2001) and two aftershocks have slip along the southern extension of the mainshock slip region. On the other hand, several aftershocks show strong evidence of basement-involved deformation. One of the strike-slip aftershocks nucleated within the basement but ruptured upward and generated a very large slip patch within the overlying sedimentary strata. Another basement-involved aftershock occurred beneath the city of Chaiyi and caused substantial damage. This study is the first showing that basement structures in Taiwan can be seismogenic and can influence the crustal structures above the decollement.

This study has many far-reaching implications. Reflection and gravity study documented a mechanism to exhume basement materials to shallow depths. The finite fault inversion study can be used to identify blind thrusts under metropolitan regions, to study the stress interaction and perturbation due to the Chi-Chi earthquake sequence, and are being used to improve seismic attenuation relationships for engineering purposes. Our results suggest that large aftershocks might have contributed significantly to the observed postseismic GPS deformation. From our finite fault studies we were able to document the accuracy of the input earthquake source parameters with respect to acceptable fits of the synthetics to the observed waveforms, which has implications for

applications of finite-source inversions for near-realtime strong ground motion simulation (e.g. Dreger and Kaverina, 2000).

The thesis is organized in the following way. Chapter 2 describes the accretionary prism structure south of Taiwan using seismic reflection and gravity data. This chapter has been accepted for publication in Tectonophysics, pending some revision. Chapter 3 presents a strong motion model of the Chi-chi mainshock source process, and chapter 4 presents the source of one of the aftershocks. These chapters have been published in BSSA (Chi et al., 2001) and Chi and Dreger (2002), respectively. Chapter 5 is a compilation of finite-source results for 6 of the large Chi-Chi aftershocks and presents a through examination of the resolution of fault orientation parameters using strong motion waveform data.

In summary, we have studied the crustal evolution of Taiwan from subduction to collision and found basement-involvement in structures associated with the collision. We also have found that pre-existing basement structures can be seismogenic and can modify the structures above the decollement.

Figure 1.1: Topography and tectonic framework of Taiwan (modified from Angelier et al., 1997). Taiwan is located along the convergent boundary between the Eurasian plate (EP) and the Philippine Sea plate. Dashed lines mark the interpreted plate boundaries. The crustal structures become more complex from the region of subduction in the south to arc-continent collision in the north. Red and yellow lines mark regions of analyses of seismic reflection and gravity in the subduction zone, and the initial collision zone, respectively. The blue circle marks the epicenter of the Chi-Chi, Taiwan earthquake. Shading shows bathymetry from Hsu et al. (1998).

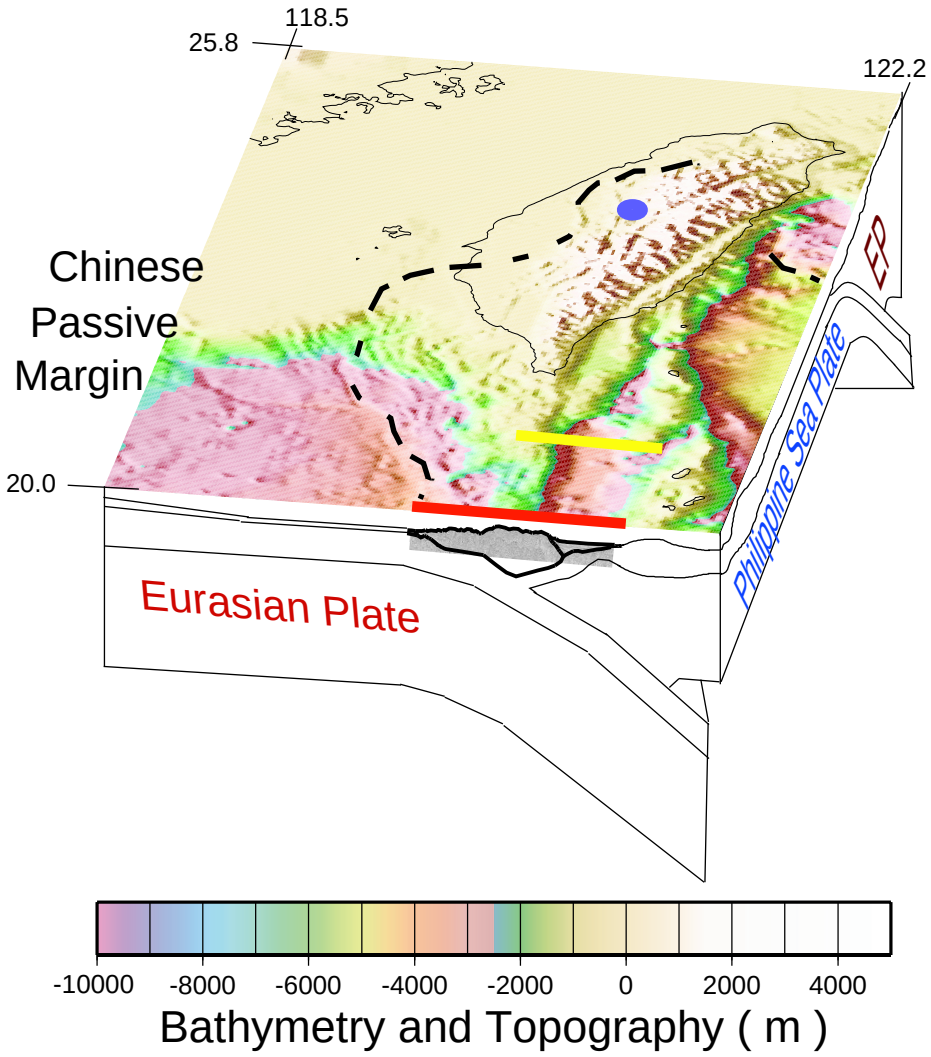
118.5
25.8
122.2
Chinese
Passive
Margin
20.0
EP
Philippine Sea Plate
Eurasian Plate
-10000
-8000
-6000
-4000
-2000
0
2000
4000
Bathymetry and Topography (m)

Figure 1.2: The critical taper model (Suppe, 1981, Davis et al., 1983) was first proposed to explain the structures of Taiwan. This schematic cross section shows that the onland Taiwan accretionary prism has a topographic slope of 2.9^{o} on the trench side, 6^{o} on the eastward-dipping decollement, and 6^{o} topographic slope along the rear of the accretionary prism. Suppe (1981) proposed that Taiwan is in an equilibrium state and that the accretionary prism will grow to maintain the critical taper angle.

Taiwan

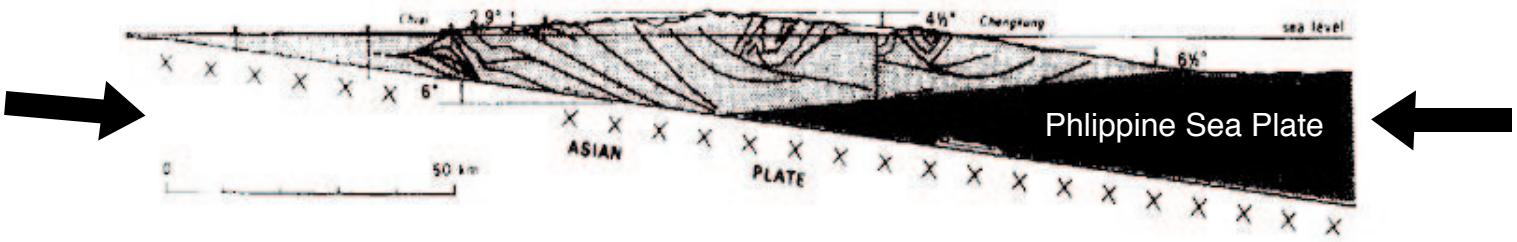

Chapter 2

Tectonic Wedging along the Rear of the Offshore Taiwan Accretionary Prism

2.1 Abstract

The structural geometry, kinematics and density structure along the rear of the offshore Taiwan accretionary prism were studied using seismic reflection profiling and gravity modeling. Deformation between the offshore prism and forearc basin at the point of incipient collision, and southward into the region of subduction, has been interpreted as a tectonic wedge, similar to those observed along the front of mountain ranges. This tectonic wedge is bounded by an east-dipping roof thrust and a blind, west-dipping floor thrust. An east-dipping sequence of forearc-basin strata in the hanging wall of the roof thrust reaches a thickness in excess of 4 km near the tip of the interpreted tectonic wedge. Section restoration of the roof sequence yields an estimate of 4 km of shortening, which is small compared with that inferred in the collision area to the north, based on the variation in distance between the apex of the prism and the island arc.

Previous studies propose that either high-angle normal faulting or backfolding has exhumed the metamorphic rocks along the eastern flank of the Central Range in the collision zone on land. To better constrain the initial crustal configuration, we tested 350 crustal models to fit the free-air gravity anomaly in the offshore region to study the density structure along the rear of the accretionary prism in the subduction and initial

collision zones before the structures become more complex in the collision zone on land. The gravity anomaly, observed in the region of subduction (20.2^{o}N), can be modeled with the arc basement forming a trenchward-dipping backstop that is overlain by materials with densities in the range of sedimentary rocks. Near the point of incipient collision (20.9^{o}N), however, the free-air gravity anomaly over the rear of the prism is approximately 40 mgals higher, compared with the region of subduction, and requires a significant component of high density crustal rocks within the tectonic wedge. These results suggest that the forearc basement may be deformed along the rear of the prism, associated with the onset of collision, but not in the subduction region further to the south.

2.2 Introduction

A tectonic wedge (Wentworth et al., 1984) is a wedge-shaped structure bounded by a roof thrust along its upper surface and a floor thrust beneath (Figure 2.1). Tectonic wedges have been recognized in a number of regions, including the California Coast Ranges (Wentworth et al., 1984; Unruh et al., 1995; Wakabayashi and Unruh, 1995; Jachens et al., 1995), the Rocky Mountain front (Lawton et al., 1996), and Himalayan orogen (Jadoon and Frisch, 1997). The floor thrust is buried under the tectonic wedge and commonly occurs as a blind thrust that is difficult to map based on surface observations. The hanging wall of the roof thrust (roof sequence) can be composed of a dipping sequence of thick basin sediments. Backthrusting in the form of tectonic wedging has been identified along the rear of several submarine accretionary prisms and thrust belts

(Westbrook et al., 1988; Silver and Reed, 1988; Torrini and Speed, 1989; Silver et al., 1990; Reed and Silver, 1995). To avoid confusion, in this article we use "wedge" to indicate tectonic wedge and "prism" to indicate accretionary prism. In addition to their tectonic significance, these features can form structural traps for petroleum and may also be seismogenic (Wentworth et al., 1984).

Deformation along the rear of the offshore Taiwan accretionary prism in the region of subduction has also been interpreted as a tectonic wedge (Reed et al., 1992; Lundberg et al., 1992, Lundberg et al., 1997). There are two competing models that have been used to explain deformation further to the north, along the eastern flank of the Taiwan Central Range, which lies in an analogous position as the rear of the offshore prism. One model has proposed two parallel, steeply dipping normal faults that allow uplift and exhumation of high to medium-grade metamorphic rocks of continental origin in the Central Range (Crespi et al., 1996; Byrne and Crespi, 1997a; Lin et al., 1998). This feature may project southwards along the east coast of the Hengchun peninsula and into the offshore along the eastern flank of the submarine Hengchun Ridge, which forms the rear of the accretionary prism. On the other hand, Fisher and Willett (1998) proposed that backfolding within a double-vergent orogen above a west (trenchward)-dipping back stop may explain the onland structures in a manner that is similar to the backthrusting model interpreted for the offshore. Strike-slip faulting is also active in the Longitudinal Valley and offshore, but cannot by itself account for the large amounts of uplift in both regions. On land deformation may also be complicated by the incoming thick passive margin, but a reliable geodynamic model in the offshore region where the structures are simpler may help constrain the initial models for the arc-continent collision zone. The

major difference between these models is the nature of deformation along the eastern flank of the Central Range, high-angle normal faulting or backfolding associated with thrusting, and the geometry of the arc basement, which acts as a backstop against which deformation takes place. In this study we use geophysical data to better constrain the deformation style in the offshore region, and to examine the involvement of the forearc basement along the rear of the prism.

Here we use migrated multichannel depth sections and gravity modeling to examine the geometry and kinematics of deformation along the rear of the prism in the offshore, near the region of incipient collision, and southwards to the region of subduction. Multichannel data are first used to interpret deformation in this region as reflecting a tectonic wedge related to compression due to crustal shortening. Next, we show that, in the subduction zone, the shortening at shallow depth along the rear of the prism is small, compared to that observed to the north along the Taitung Trough where arc-continent collision began 1-2 Ma. Finally, we provide constraints on the nature of the basement (backstop) geometry in the regions of subduction and the earliest phases of arc-continent collision. At the very least, we determine whether or not basement rocks (or the backstop) are involved in the deformation at this point. The results of gravity modeling are consistent with a tectonic wedge composed mainly of sedimentary material at the latitude of 20.2^{o}N, which overlies the west-dipping basement of the island arc, while at 20.9^{o}N, the in-situ or underplated basement rocks may become involved in deformation and uplifted. This interpretation implies that the sedimentary materials within the tectonic wedge must be part of the accretionary prism or have been incorporated into the tectonic wedge by duplexing of forearc basin strata above a

trenchward dipping backstop in the subduction region. As the subduction changes into collision, however, high density materials associated with the forearc basement, are deformed, possibly in a mode that is compatible with the double vergent orogen model (Willett et al., 1998; Fisher et al; 1998; Malavieille et al., in press).

2.3 Tectonic Setting

The Taiwan collision zone is located along the boundary between the Eurasian plate and Philippine Sea plate where the Chinese continental margin has been juxtaposed with the northern segment of Luzon island arc (Bowin et al., 1978). South of the island, oceanic lithosphere of the South China Sea is subducting eastward beneath the Philippine Sea plate along the Manila Trench (Figure 2.1) (Bowin et al., 1978; Taylor and Hayes, 1980).

The initial collision probably began in the late middle Miocene (Teng, 1990) and is currently propagating southward at a rate of 55 to 120 mm/yr (Lundberg et al., 1997; Byrne and Crespi., 1997b; Suppe, 1984). The geometry of the plate boundary, plate motion, and continental-ocean boundary in the Eurasian plate produces a southward propagation of the collision, allowing the concept of time-space equivalence to be applied to the evolution of the collision complex (Suppe, 1984). This concept states that evolution of the collision can be studied by constructing a series of cross sections, oriented east-west, through the subduction zone in the south to the more mature collision zone on Taiwan in the north. However, this concept remains controversial. Malavieille

(2002) has proposed that the deformation of the accreted arc terminated abruptly just south of Taiwan. Based on 2D and 3D physical modeling, Chemenda et al. (2001) also proposed that the Longiudinal Valley Fault, a major structure in Taiwan, is propagating to the south.

Recent kinematic studies of Taiwan island have greatly improved the understanding of deformation at shallow depths of the collision complex (e.g. Yu, 1995; Suppe et al., 1984; Lu et al., 1995; Hu et al., 1997; Lee et al., 1997; Angelier et al., 1997; Crespi et al., 1996; Lee et al., 1991). Detailed GPS surveys over the last decade (Yu et al., 1997) show a significant component of shortening between the offshore island Lanyu and the eastern flank of the Central Range. It is not known, however, how much shortening is taking place to the south of this region since GPS data are not available in the offshore region of the subduction zone where the structures are submerged.

The submarine accretionary prism consists of three distinct structural domains: a lower slope domain along the inner slope of the Manila Trench, an upper slope domain composed largely of the submarine Hengchun Ridge, and a backthrust domain along the rear of the submarine accretionary prism at the boundary between the Hengchun Ridge and the North Luzon Trough (Reed et al., 1992). These domains are found in both collision and subduction regions of the forearc. In the submarine portion of the collision, the backthrust domain (Figure 2.2) exhibits several west-dipping backthrusts and the North Luzon Trough, a forearc basin, is truncated by the juxtaposition of the rear of the prism with the island arc (Lieske et al., 1992; Lundberg et al., 1997). In the region of subduction, the forearc basin strata have been uplifted along the rear of the prism and dip

eastward. Reed et al. (1992) inferred that uplift in this region resulted from the insertion of a tectonic wedge of prism material between a 2.5 sec-thick sequence of the forearc basin strata and the arc basement.

2.4 Data Acquisition and Processing

A multi-channel seismic (MCS) survey was conducted in the offshore regions surrounding southern Taiwan during the TAICRUST experiment with the R/V Maurice Ewing from Columbia University in 1995 (Reed et al., 1996; Liu, et al., 1997; Moore et al, 1997). Here we use MCS and gravity data collected along line EW9509.49 of the expedition and R/V Vema line V3618.49 (Nguyen et al., 1998) across the forearc basin in the region of subduction to the south.

2.4.1 Reflection data

The MCS data acquisition system included an 8420 in^3 air gun array, composed of 20 airguns, and a 4.2 km-long 132-channel streamer. Shot interval was 50 m with recordings to 16 seconds. The data were processed at the University of Hawaii using the ProMAX processing package. Additional post-stack processing and plotting were completed at San Jose State University using SIOSEIS. The overall processing sequence, described in Berndt and Moore (1998), included resampling at 4 msec, geometry, true amplitude recovery, FK demultiple in both the shot and receiver domains, dip move out, velocity analysis, radon filter, 40-fold weighted stack at 12.5 m CDP spacing, time variant frequency filter, FK or FD migration and automatic gain control. Different

migration schemes have been tested and we found finite-difference (FD) migration gave better results for this section. The migration velocity was modified iteratively to reduce undermigration and overmigration artifacts at the same time. We then converted the profile to depth using the velocity models from interactive analysis (Figure 2.3). The Vema line is processed in similar fashion and the details are described in (Nguyen, 1998.)

2.4.2 Data Analysis

The North Luzon Trough is a forearc basin associated with the Manila Trench subduction zone in the region of line EW9509.49. Stratal reflections in the eastern portion of the basin are horizontal to sub-horizontal and lap onto the western flank of the island arc (Figure 2.2). These strata thicken to the west, towards the accretionary prism, and reach a total thickness of 2.5 sec in two-way travel time (TWTT) or greater than 4 km. Hirtzel (1996) divided the high amplitude, continuous reflections into 9 seismic sequences, of which, the reflections in the upper three (1-3) seismic sequences diverge eastward and resemble growth strata that mark the onset of an episode of uplift due to tectonic wedging. These strata are ultimately incorporated into the rear of the accretionary prism by backthrusting in the region of collision in the formation of the Huatung Ridge (Reed et al., 1992). The forearc basin sediments were derived from a combination of sources, including the island arc, onland collision complex, and through submarine erosion of the prism (Lundberg et al., 1992, 1997; Hirtzel et al., 1994). Mass wasting along the rear of the accretionary prism also contributes debris to these deposits (Lundberg et al., 1992; Hirtzel et al., 1994).

The surface of the arc basement generally dips to the west, however, a 7 km-wide basement high with a relief of about 700 m is buried under the forearc strata in the vicinity of line EW9509.49. This feature may represent the western extent of the submerged portion of the island arc. To the west, the forearc basement dips smoothly to the west and may extend under the tectonic wedge, although the basement reflector is weak and not imaged beneath the prism.

On the west side of the North Luzon Trough, thick packages of reflections are tilted eastward along the rear of the prism. More than 1100 meters of seafloor relief separates the apex of the tilted forearc basin reflections from the flat-lying sequences in the North Luzon Trough. Minor conjugate thrust faulting, at a spacing of 2-3 km, is common within the forearc basin strata. Reed et al (1992) interpreted the uplift of these sequences as a result of backthrusting in the form of tectonic wedging.

Seismic sequences in the hanging wall of the roof thrust above the tectonic wedge (Figure 2.2) show evidence of complex tectonic deformation, although a detailed analysis of this feature is beyond the scope of this study. A westward decrease in stratigraphic thickness causes an increase in bedding dip from 5 to 30 degrees at greater depths. We follow the seismic sequence designation of Hirtzel (1996) to study the geometry of the youngest to the oldest strata, sequence 1 to sequence 9, respectively (Figure 2.2). The thickness of sequence 1 increases from 500 m over the tectonic wedge to 800 m at the center of the forearc basin. Sequences 2 and 3 show erosional truncation, and the most dramatic changes in thickness from 300 m to 900 m, thereby forming divergent patterns of reflectors within seismic sequences. The thicknesses of sequences 4 through 9 vary

from 1200 m to 2700 m, with the axis of an anticlinal fold in these strata shifted 4.5 km to the west of that observed in sequences 2 and 3. Thus the fold axis is partially eroded in sequences 3 and 4, and somewhat disrupted by the west-dipping reflectors in sequences 5-9. West-dipping reflectors extend through the tectonic wedge and upwards across stratal reflections of the roof sequences. These features may be fault planes, which ultimately result in the incorporation of forearc-basin strata into the rear of the prism (Reed et al., 1999), although additional processing is required to rule out origins as diffractions, overmigration artifacts, or out-of-plane effects. The amount of offset across these protothrusts is less than the resolution of our data (< 40 m), thus is interpreted as very small. The seismic character of sequences 1 through 3 is chaotic, resulting from debris flow deposits along the rear of the prism (Hirtzel, 1996). The floor thrust observed in line EW9509.49 can be traced at least 1.5 km further to the west than recognized in previous studies.

Another fold (Fold B in Figure 2.2) is observed to the west of the crest of the main fold in forearc strata in the hanging wall of the roof thrust. The thickness of sequence 1 increases from 400 m to 800 m westward in this fold. One east vergent fault-bend fold underlies sequence 1. Bedding has been offset by this fault. Sequences 2 and 3 have a relatively constant thickness of 300 m. Several possible west-dipping fault plane reflections are interpreted under sequences 2 and 3. Sequences 4 through 9 are not recognized in this area. We have tested different migration schemes and different migration velocities to better image this portion of the profile and found that the FD method reduces high frequency noise, and that higher migration velocities will cause overmigration artifacts.

2.4.3 Tectonic Wedge

We estimated the minimum shortening of forearc basin strata above the tectonic wedge by restoring the tilted units to an original, horizontal geometry. This calculation assumes no change in the length of bedding surfaces, little or no oblique movement, and horizontal deposition of sediments in the hanging wall of the roof thrust.

The forearc basin strata were flattened with a resulting shortening estimate of less than 2 km within the roof sequence. The amount of shortening related to the small-offset fault planes and folding in the roof sequences is less than 1 km. Additional shortening to the west of these units, if it exists, cannot be measured due to chaotic character of the reflections, presumably related to deformation associated with sediment accretion along the Manila Trench during the early history of the prism.

Structures associated with shortening within the forearc strata can be divided into three packages (Figure 2.4). The amount of shortening following the deposition of sequence 1 is approximately 0.5 km while the shortening following deposition of sequences 4 to 9 ranges from 0.8 to 1.2 km. The units with different amounts of shortening are separated by the wedge-shaped sequences 3 and 4, suggesting non-uniform rates of either shortening or sedimentation.

2.4.4 Gravity Data Analysis

Using the shallow crustal geometry derived from MCS data, we model the free-air gravity anomaly to constrain the geometry of the arc basement beneath the rear of the prism. We construct a transect of the entire forearc, from the arc to the trench, in the vicinity of the seismic interpretation of line EW9509.49 using the regional gravity data compilation of Hsu et al (1998) sampled at a 1 km spacing. The extended transect will provide additional constraints for the long wavelength components of the anomaly in gravity modeling. These data were compared with the free-air gravity anomaly obtained along line EW9509.49 (Figure 2.5). The gravity anomalies are similar in the two datasets, except that data on line EW9509.49, which crosses only a portion of the forearc, includes an additional short wavelength component of the anomaly, not resolved in the regional compilation.

The initial model geometry of the forearc basin and rear of the prism (Figure 2.6) was derived from the interpretation of MCS data. The densities of the forearc strata were inferred from the empirical velocity-density function by Godfrey et al. (1997) who compiled the Vp velocities and rock density data collected across the ancient forearc basement of the Great Valley and eastern slope of the Coastal Range of California. From the figure by Godfrey et al. we assigned 2.0, 2.1, 2.2, 2.3, 2.4, 2.5 g/cm^3 for P velocities of 1.9, 2.2, 2.5, 2.8, 3.3, and 3.8 km/s, respectively. Igneous basement rocks and mantle rocks were assigned densities of 2.85 and 3.3 g/cm^3, respectively. The prism velocity is inferred from OBS refraction studies (Nakamura, personal communication, 1999). The geometry of the arc (Figure 2.6) was derived from a crustal model based on the ocean-bottom seismograph (OBS) data by Chen and Nakamura (1998). Because the OBS data were collected 120 km to the north, in the active collision, we will use this cross section

as the maximum thickness for the arc in the subduction region. Depth to the magnetic basement estimates by Liu et al. (1992) was used to define the top of the subducting oceanic crust on the trenchward side of the accretionary prism. However, there is a gap of 40 km from the easternmost data point in the magnetic basement compilation to the westernmost identification of the arc basement beneath of the floor thrust on line EW9509.49. The dip of the subducting slab in this region is not well constrained by earthquake event locations and its sensitivity in influencing the calculated gravity anomaly will be tested in this study. At greater depths, the location of the slab is a bit better constrained by the depth phases of the deep earthquakes, as suggested by Bautista et al. (2001). Thermal modeling of subduction zones by Anderson et al. (1978) was used as the first order approximation of the temperature field in the region. The densities of the lower crust and mantle rocks were then estimated from the phase equilbria relations presented in Hacker (1996). The thickness of the lithosphere was inferred as a wet, olivine-dominated, thermal boundary layer and estimated from the ages of the oceanic lithosphere in the Philippine Sea and South China Sea derived from magnetic data (Hilde and Lee, 1984; Taylor and Hayes, 1980) using Turcotte and Schubert (1982, p. 164, equation 4-126):

$$y_L = 2.32(\kappa t)^{1/2}$$

where y_L is the thickness of the oceanic lithosphere, κ is the thermal diffusivity, and t is the age of the lithosphere.

For oceanic crust with an age of 30 Ma, the lithosphere thickness is about 72 km. Like many other gravity studies, we choose not to introduce this complexity, below the Moho, into our gravity model because the great depth and the long wavelength of the structure should not produce the shorter-wavelength gravity anomaly over the tectonic wedge, which is the object of this study.

2.4.5 Gravity Model in the Vicinity of Line EW9509.49

Figure 2.7 shows the gravity model the vicinity of line EW9509.49. The densities within the forearc basin vary from 2 g/cm^3 in shallow sediments to 2.38 at sub-bottom-depths of 4 km. The bodies in our model with densities of 2.85 g/cm^3 are inferred to be igneous crust. The arc crust is modeled by a 5-km thick body with an upper surface dip of less than 15 degrees to the west. A high density body (2.85 g/cm^3) with an area of 40 km^2 at depths between 4.5 and 10 km was embedded into the tectonic wedge. Because the geometry of this block is not well constrained, we can only approximate the area of the high density materials needed to model the free-air anomaly.

The sub-bottom depth of the Moho near the trench is about 7 km, with a 6 km-thick igneous crust (Chen and Jaw, 1996). The dip of the subducting plate is about 3 degrees under a wedge-shaped body of deformed strata of the lower slope domain composed of sedimentary units with a density of 2.3 g/cm^3. The dip of the subducting plate increases to greater than 7 degrees below deformed units of the upper slope domain, which is modeled with a shallow block of 2.42 g/cm^3 and a deeper block of 2.52 g/cm^3, inferred from a velocity model derived from a refraction studies 100 km north of this transect (Nakamura, unpublished data). The prism reaches a maximum thickness of 10

km. The dip of the subducting plate increases again to 50 degrees between a depth of 15-20 km. Using the phase equilibria by Hacker (1996) and temperature modeling of Anderson (1978), we estimated the subducting slab starts to metamorphose to blueschist facies at depths of 15 km, then to eclogite facies at a depth of 50 km. These features were included in the model, although they have little effect on the gravity anomaly at the wavelength we have modeled over the tectonic wedge.

To understand the robustness of the results, we perturbed block densities in the model to assess their influence on gravity anomaly over the tectonic wedge (Figure 2.7). This exercise also serves to assess the contribution of each density block to the gravity anomaly. In particular, we were able to document the dominant wavelength of the gravity anomaly signals generated by each block for a range of density perturbations. Densities of 6 blocks, including 3 sedimentary layers in the forearc basin, the upper/lower layers in upper slope domain, and high density block in the tectonic wedge, were perturbed by ± 0.3 g/cm^3 with ± 0.1 g/cm^3 increments to predict the gravity anomaly variations.

We first examined the contribution of sediment density in the upper-slope domain to the gravity anomaly. The upper slope domain, across the Hengchun ridge, is divided into a top and a bottom layer to account for the vertical density gradient. Because we modeled the gravity anomaly across the whole subduction zone, we were able to use the simple and better-studied density structure on the trench side to further constrain the densities of the upper domain layers. Due to the shallow depth of this block, each 0.3 g/cm^3 of perturbation of the top upper domain layer will give ~50 mgal, long-wavelength,

gravity variation over the crest of the accretionary prism, which tapers off to ~7 mgal at the edge, just above the tectonic wedge. The bottom layer of the upper slope domain was created to represent the more deeply buried, higher density material. Because the thickness of this block varies little and because it is deeper, the perturbations in the modeled anomaly have very long wavelengths, especially over the tectonic wedge. Each 0.3 g/cm^3 change will cause a variation of less than 40 mgal, which tapers off to ~4 mgal at the edge, just above the tectonic wedge. For the high density materials in the tectonic wedge block, each change of 0.3 g/cm^3 will result in a less than 18 mgal variation over the tectonic wedge. Thus density variation within the tectonic prism exerts the strongest control on the modeled anomaly. Geometry of the forearc strata provides important constraints in our gravity analysis. However, densities of the strata is less influential: for each 0.3 g/cm^3 perturbation we found the calculated gravity anomaly only varies by 9, 9, and 5 mgal for the top, middle, and bottom layers, respectively.

By incorporating the structures near the trench into our models we were able to better constrain our overall density model, including in the vicinity of the tectonic wedge. The preferred model fits the long-wavelength gravity signal well, but does not account for some local features. In particular, our preferred model over- and under-predicts the gravity anomaly by 4 mgal over the portions of tectonic wedge, suggesting that there might be complex density variations at shallow depth in this region. The reflection profile in this region does not provide adequate control to add more geometric complexity to our model.

Sub-horizontal structures in the lower crust and mantle have little influence on the gravity anomaly at the rear of the prism. For example, an increase in the thickness of the arc crust to 9 km will result in an 8 mgal decrease in the free-air anomaly over the forearc basin. Changes in the thickness of the lithosphere have less influence on the free-air anomaly. Moreover, the short wavelength of the free-air anomaly over the rear of the prism requires a shallow crustal source and cannot be modeled to a first order with a deep source of the anomaly.

2.4.6 Gravity Model of Vema line V3618.49

To compare deformation at different stages of subduction, we also modeled the crustal structure across the forearc region, approximately 70 km south of line EW9509.49. Nguyen et al. (1998) interpreted reprocessed MCS data collected along line V3618.49 by R/V Vema from the Lamont-Doherty Earth Observatory (LDEO). The geometry of the trench and dip of the subducting slab appear to be similar in the two regions (Kao et al., 2000). The depth section constructed along this line (Figure 2.8), showing the geometry of the accretionary prism, was imported into the model, with a similar configuration of the subducting slab as used in the gravity model formulated in the vicinity of line EW9509.49.

The structure of the accretionary prism in this region is described in Nguyen (1998). The prism is composed of three structural domains (Figure 2.9), similar to that observed to the north. A sedimentary layer with a thickness from 200 to 600 m overlies a shallow east-dipping ($<10^{o}$) oceanic crust under the lower slope domain. The width of

the lower slope domain decreases by 30 km compared with that in the vicinity of the line EW9509.49. There is a sharp boundary from the lower slope domain to the upper slope domain, marked by a 1.5 km high scarp. The width of the upper slope domain is 25 km in this region. In the backthrust domain, a sedimentary tectonic wedge overlies a west dipping back stop, which is an extension of the top of the arc basement. The structure of the backthrust domain at first appears to be similar to that observed along line EW9509.49 and the sediment thicknesses in the two forearc regions are equivalent. The west-dipping fault plane reflections within the tectonic wedge and extending into the roof sequence are not present on line V3618.49. However, the data acquisition and processing schemes used in generating these two sections are significantly different.

The gravity anomaly can be modeled with a continuous west-dipping back stop extending under the tectonic wedge (Figure 2.9) to the top of the subducting plate. Moreover, the entire prism, including the tectonic wedge, in the region of subduction can be modeled using density ranges of sedimentary rocks (2.3-2.52 g/cm^3).

Figure 2.9 shows the sensitivity tests for modeling along line V3618.49. Because we are mainly interested in the density structure along the rear of the accretionary prism, we only tested the 2-layer models of the upper slope domain, and the 3 layers of the forearc strata. Again we found the density perturbation of the forearc strata causes little effect: less than 6 mgal, 8 mgal, 5 mgal of gravity anomaly due to changes from ±0.3 g/cm^3 of density perturbations for top, middle, and bottom layers, respectively. For the upper slope domain, the changes are 55 mgal for 0.3 g/cm^3 increase in the top layer and 35 mgal for lower layer.

2.5 DISCUSSION

Shortening resulting in uplift and deformation of the roof sequence within the forearc basin in the vicinity of line EW9509.49 is less than 2 km, based on the line balancing analysis. Factors that contribute errors in estimating the shortening include: errors in velocity field that was used to generate depth-corrected cross section, 3D complexity, non-horizontal deposition of forearc basin strata used in restoration, and layer-parallel shortening in high porosity sediments.

The excellent signal to noise ratio and well-defined stratigraphy within the forearc strata make interactive velocity analysis relatively straightforward. By applying DMO to the sub-horizontal reflectors, we reduced the errors due to shallow dipping reflectors. Unfortunately we do not have refraction data to cross check our velocity model used for depth conversion. However, even if we increase the velocity by 100%, the increase in shortening will not exceed 3 km, thus the errors from depth conversion should not be large.

We have examined the SeaMARC II and 6-channel MCS data collected by the R/V Moana Wave in the region (Reed et al., 1992). This dataset shows no dramatic change of stratigraphy across the tectonic wedge. As a result, strike-slip movement, at least in the forearc basin strata, does not pose severe problems for retrodeforming analysis in this particular cross section. Oblique slip may have occurred along faults further to the west or is higher on the rear slope of the prism.

The east dipping seafloor, above the roof sequence, suggests non-horizontal deposition of sediments within the roof sequence. However, the dips are relatively small and will result in less than 30% overestimate of shortening for a bathymetric slope of less than 20%. The retrodeformed cross section uses a constant thickness for each sequence, which is different from the growth strata found in sequences 2 and 3. Thus this is not an "area-balanced" retrodeformation.

One uncertainty in line balancing in compressional regimes comes from layer-parallel shortening before the onset of folding, some of it associated with dewatering. Thus our estimates should be interpreted as the minimum shortening. We estimate that the deformed forearc strata have lengths of about 10 km, translating into 4 km of shortening for a 40 % parallel shortening before folding.

We also examined the forearc strata within line V3618.49 and found sequences 1 and 2 are less folded, indicating even less shortening compared with the region of line EW9509.49.

2.6 Implications of the Shortening

We will assume that the variation in distance between the crest of the island arc to the apex of the accretionary prism is a first-order measure of crustal shortening within the forearc region related to the closure of the forearc basin in the region of collision. The distance between the crest of the accretionary prism to the arc is more than 50 km greater in the subduction zone region at a latitude of 20.2^{o}N than in the collision zone at 22.7^{o}N. Several west-dipping faults were imaged in the collision region, showing increasing

shortening along the rear of the prism from south to the north (Reed et al., 1992; Lundberg et al., 1997, Malavielle, in press). Tang and Chemenda (2000) proposed that forearc basin basement starts to subduct underneath the collided Luzon Arc in the collision zone. Assuming a constant shortening of 40 mm/yr, similar to that observed in recent GPS studies between the islands southeast of Taiwan and the east side of the Central Range (Yu et al., 1998), we estimated that the decreased width is equivalent to 1-1.5 m.y. of shortening. Using the time-space equivalence graph (Figure 2.1b) we converted the time duration into distance along the convergent boundary, which is 100-150 km south of the 22.7^{o}N. This analysis suggests that the southernmost point of significant shortening is located between 21^{o} and 21.5^{o}N, which corresponds to the location where the forearc basin starts to collapse as in the modern setting. If the shortening rates between the accretionary prism and the island arc are less than 40 mm/yr, the initial shortening point would be further south.

Even though the observed difference in shortening seems to fit the time-space equivalence concept well, we can not exclude other alternative mechanisms that may account for larger shortening on land compared with the offshore region. For example, the incoming passive margin in the collision zone may result in shortening in other regions of the forearc, such as the active backthrusting west of the tectonic wedge, which may accommodate part of the missing shortening in the subduction region. The intensive deformation in that region makes it very difficult to identify any offsets due to potential backthrusts. However, the bathymetry of the eastern slope of the prism shows little variation from the subduction region to the point of incipient collision, suggesting similar shortening rates in the back thrust domain, west of the tectonic wedge, prior to collision.

We have mapped fault-plane reflectors that propagate into the roof sequence near the point of incipient collision. The small offsets of the strata in the roof sequence across these faults suggest that the deformation is relatively young and the amount of shortening is small. On the other hand, the shortening within the tectonic wedge must be larger than that of the roof sequence, in order to generate the 4-km uplift. Unfortunately we do not have good geometry and kinematics data within the tectonic wedge to study more detailed shortening in that region.

2.6.1 Implications of free-air gravity modeling in the vicinity of the tectonic wedge

It is not the purpose of this study to constrain all the elements of the subduction zone. However, we hope to develop a framework, and from sensitivity tests, identify the major structures that contribute to the free-air gravity anomaly observed over the rear of prism in the regions of subduction and initial collision.

The results of our gravity modeling indicate that the prism in the region of subduction along line V3618.49 is mainly sedimentary. Once the mantle and the subducting slab are added to the model, derived from the MCS data, the gravity anomaly required either a very thick forearc crust (greater than 50km), or as a more reasonable alternative, low-density materials composing the rear of the prism and the tectonic wedge.

The free-air anomaly along line EW9509.49 shows a 70 mgal increase from forearc basin to backthrust domain, compared a 30 mgal increase over the same region

along V3618.49 in the area of subduction. The differences in bathymetry along these 2 transects can contribute 20 mgal of the gravity anomaly deficiency. The magnitude of the gravity anomaly decays as the inverse of the square of distance, thus shallow bathymetry, being closer to the sea surface where gravity data was observed, has big influence on the predicted anomaly. In our study, the bathymetry is well constrained by swath-mapping and MCS data. The remaining anomaly deficiency must be related to different density structures at depth. Sensitivity tests show that either the entire backthrust domain must be assigned a density of 2.6 g/cm^3 or that a high density (2.85) body composes a significant portion of the material under the roof thrust.

We prefer the high density body interpretation over the uniform 2.6 g/cm^3 tectonic wedge interpretation because density of 2.6 g/cm^3 is approaching the upper bound for siliclastic sediments (Turcotte and Schubert, 1982), yet we have identified several bottom-simulating reflectors (BSRs) along the rear of the accretionary prism in this region which suggests that this region is mostly sedimentary, at least to a subbottom depth of several hundred meters. Also, the high density body in the tectonic wedge modeled in line EW9509.49 may extend northward along rear of prism to a region that shows tomographic evidence for a high velocity body (Cheng et al., 1998).

Several mechanisms may account for the incorporation of high density materials into the tectonic wedge along line EW9509.49. High-density basement rocks could be incorporated into the tectonic wedge from the basement beneath the forearc basin, similar to a mechanism proposed by Godfrey et al. (1997) to explain the tectonic wedging in California. Because the shortening of the roof sequence along line EW9509.49 is about 1

km greater than that of line V3618.49, part of the uplifted basement could be due to the differential shortening of the lower crust under and within the tectonic wedge. Basement-involved tectonic wedges have been proposed in other regions around the world, including Canada, USA, and Australia (Price, 1986; Godfrey et al., 1997; Mitra and Mount, 1998; Flottmann and Hand, 1999).

These small (< 40 km^2 in cross section view) high density bodies could also be interpreted as underplated materials derived from the downgoing lithosphere. Based on paleogeographic and geochronologic data, the melange and ophiolitic materals found in an analogous position in the collision zone onland have been interpreted as part of the South China Sea lithosphere (e.g. Liou et al., 1977, Suppe, 1988). If this is the case, our gravity models do not capture the evolution and transport of these bodies from the subduction region to the initial collision region.

The gravity study also shows that the prism can be modeled with a double vergent orogen type of deformation, especially in the region of subduction. The trenchward dipping arc basement acts as a backstop that can cause backthrusting and backfolding where accompanied by shortening. The gravity anomaly in the latitude of 20.2^{o}N suggests no dramatic uplift or deformation of basement. In contrast, gravity modeling results suggest that the basement materials have been uplifted at the latitude of 20.9^{o}N. We can not rule out the possibility of an arcward dipping fault, as proposed in the collision region farther to the north, based on the gravity modeling alone. The gravity anomaly can be modeled with a trenchward dipping back stop, and uplifted basement

rocks in the region of incipient collision, which is consistent with the model of a double vergent orogen, at least in this region of the initial collision.

2.7 SUMMARY

The structure of the boundary between the accretionary prism and forearc basin in the subduction zone, offshore southern Taiwan, resembles that associated with tectonic wedges found elsewhere in the world. Multichannel seismic data provide new constraints on the structural geometry in this region. The tectonic wedge is bounded by a 30^{o} east-dipping roof thrust, and a 15^{o} west-dipping floor thrust. The tip of the tectonic wedge is buried under 4 km of forearc strata. The strata of the roof sequence are tilted eastward and uplifted more than 1 km due to tectonic wedging. We performed line retrodeformation to estimate the minimum shortening within the roof sequence above the tectonic wedge, which is less than 2 km over last few million years. Bedding parallel shortening can add another 4 km of shortening. This shortening is very small compared with the current shortening in the collision measured by GPS, which predicts more than 40 km of shortening over 1 million years. The difference in shortening can be explained by a shift in the location of crustal shortening from the trench in the subduction region to other regions of forearc in the collision zone, including the region between the Hengchun Peninsula and the island of Lanyu (Yu et al., 2001).

Gravity modeling suggests that the tectonic wedge and the rear of the accretionary prism are mainly composed of sediments in the region of subduction at the latitude of

20.2°N. However, basement rocks may exist along the rear of the accretionary prism in the collision region beginning at 20.9°N and may extend northward to outcrops on land. These results imply that a trenchward dipping arc basement acts as a backstop to a double vergent orogen or that a fundamental change in deformation style must occur between the point of incipient collision in the offshore and the Central Ranges in order to accommodate an east-dipping fault on land.

2.8 Acknowledgements: We thank Dr. G.K. Westbrook and Dr. K.D. McIntosh for their careful reviews and constructive criticism. We also want to thank the captain and the crew members of the R/V Maurice Ewing of the Columbia University. Especially, line EW9509.49 used in this study was surveyed after we encountered 5 typhoons in the one-month cruise. WCC thanks Matthew d'Alessio for helpful discussion. Most of the figures were generated using GMT and SIOSEIS. Dr. Paul Henkart is thanked for his help on SIOSEIS. This research is partially funded by NSF Grant OCE-9416583 to Dr. Donald Reed at San Jose State University.

Figure 2.1: (a) Location map. Lithosphere beneath the South China Sea is subducting southeastward at a rate of 85 mm/yr under the Philippine Sea plate along Manila Trench. The thick gray line marks the location of line EW9509.49 crossing the initial arc-continent collision region. Line AA' marks the location for a seismic profile in Figure 2.2. Line BB' marks the location for Figure 2.7. Line CC' marks the location for Figure 2.6. Line DD' marks the location for Figure 2.9. Circles mark the line V3618.49 collected by R/V Vema crossing the subduction zone. An example of the upper and lower slope domains and the backthrust domain is shown in Figure 2.9. (b) Due to the oblique angle of the Chinese Passive Margin with respect to the trench, the collision is currently propagating southward along the trench at a rate of 102 mm/yr (Lundberg et al., 1997). (c) A cartoon showing a tectonic wedge bounded by a roof thrust along the top and a floor thrust at the bottom. The location of the schematic tectonic wedge profile is marked by AA' in the regional map.

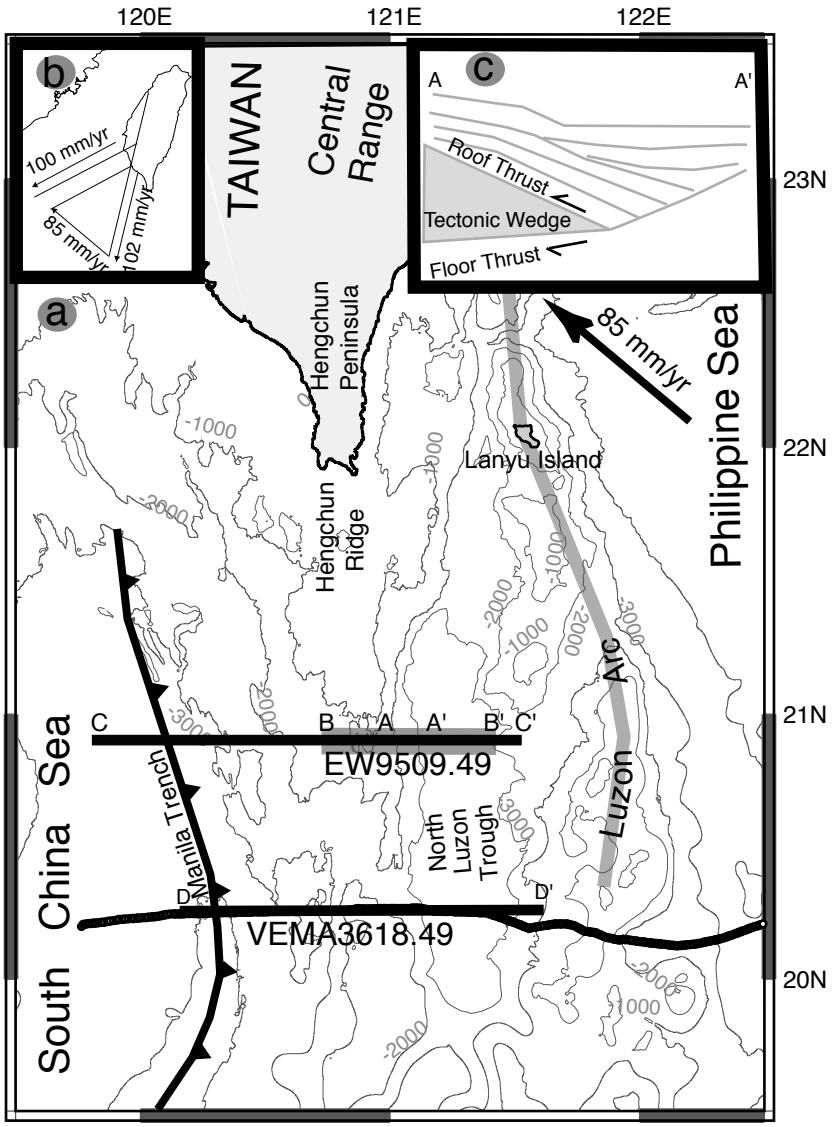
120E
121E
122E
23N
22N
21N
20N
a
b
c
TAIWAN
Central Range
100 mm/yr
85 mm/yr
102 mm/yr
A
A'
Roof Thrust
Tectonic Wedge
Floor Thrust
Hengchun Peninsula
85 mm/yr
Philippine Sea
Lanyu Island
Hengchun Ridge
Arc
Luzon
C
B
A
A'
B'
C'
EW9509.49
South China Sea
Manila Trench
North Luzon Trough
D
D'
VEMA3618.49
-1000
-2000
-3000

Figure 2.2: Uninterpreted and interpreted portions of MCS line EW9509.49 that shows features within the west-flank of the forearc basin and the backthrust domain. For the forearc strata, we follow the seismic sequences by Hirtzel (1996). Note folding (Fold A) due to thickening and advancing of the tectonic wedge. Also see west dipping fault plane reflections within the tectonic wedge that propagate into the roof sequence. A fault propagation fold (Fold B) is above the tectonic wedge to the west. See Figure 2.1 for the location of this cross section.

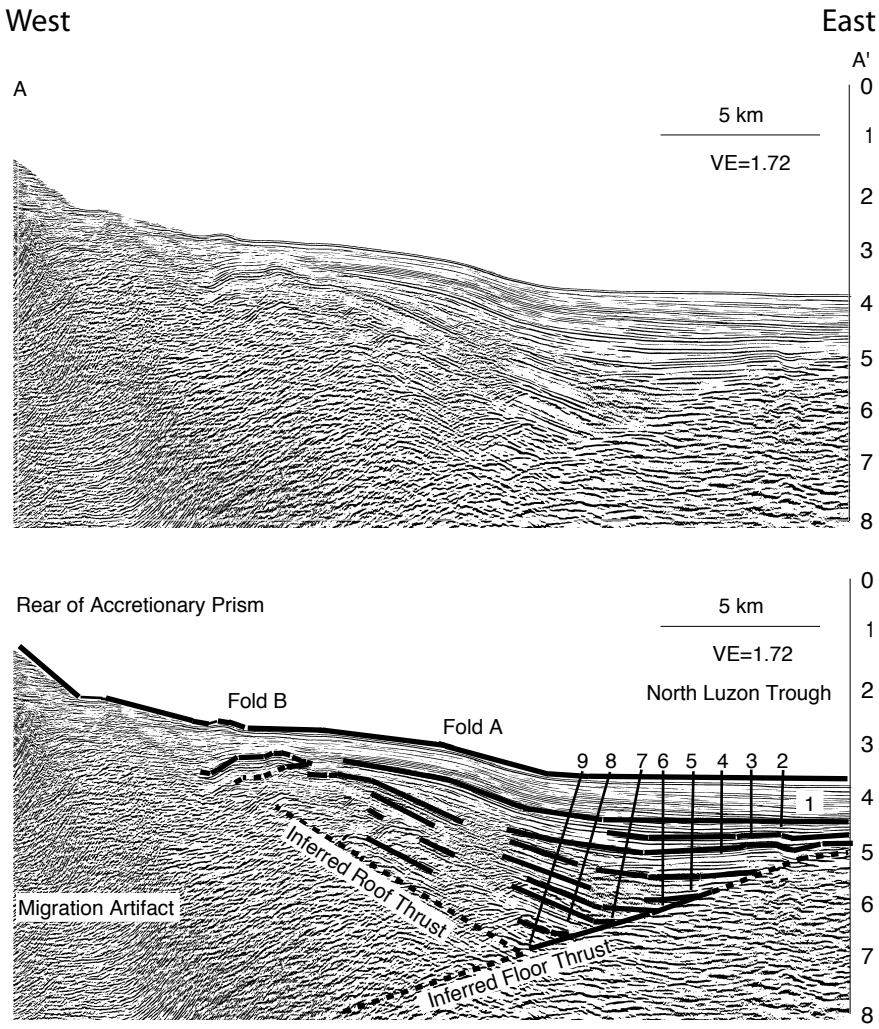
West
East
A
A'
5 km
VE=1.72
0
1
2
3
4
5
6
7
8
Rear of Accretionary Prism
5 km
VE=1.72
North Luzon Trough
Fold B
Fold A
9 8 7 6 5 4 3 2
1
Inferred Roof Thrust
Migration Artifact
Inferred Floor Thrust

Figure 2.3: The velocity section and uninterpreted section of the entire MCS line EW9509.49. The depth section in Figure 2.2 is converted from time to depth using this velocity field, depicted in gray color contours in the upper panel. For location see Figure 2.1. The thick lines in the upper panel show the geometry of the density model, as explained in the gravity modeling section of the text.

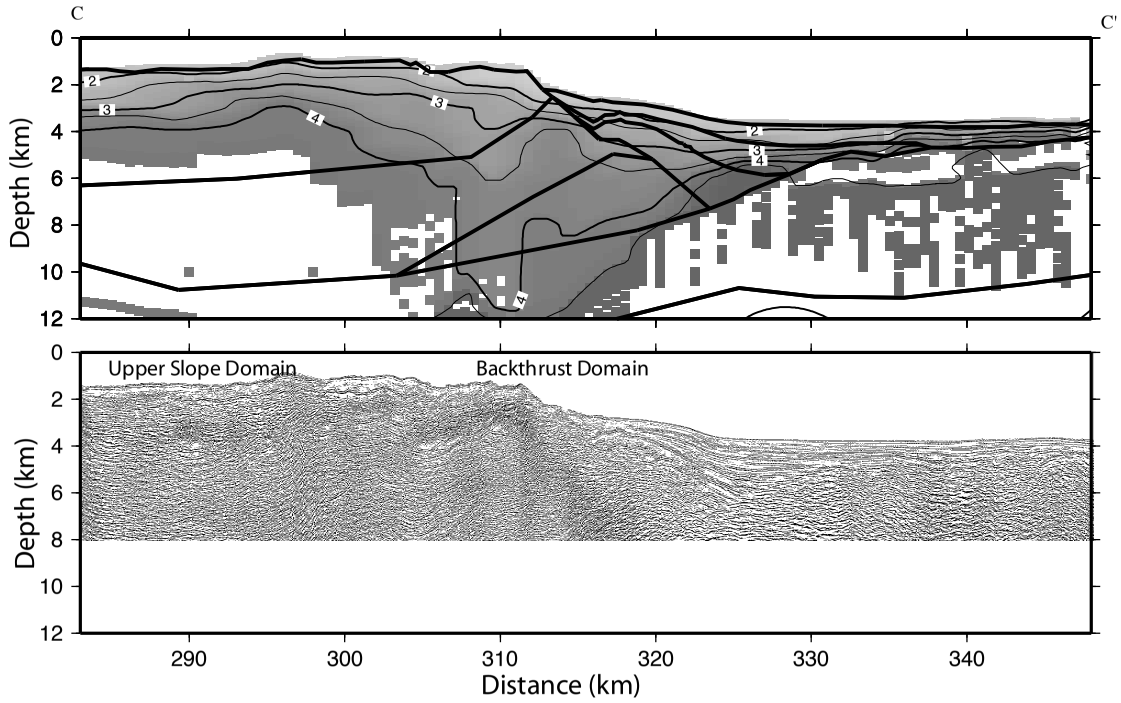
C
C'
Depth (km)
0
2
4
6
8
10
12
2
3
4
Upper Slope Domain
Backthrust Domain
290
300
310
320
330
340
Distance (km)

Figure 2.4: Line balanced cross section of line EW9509.49. The forearc basin strata are divided into three major packages. Shortening within these packages shows less than 2 km of shortening. The wedge-shaped sequences 3 and 4 (the middle package) suggest non-uniform rates of either shortening or sedimentation. The lines used for balancing are the seafloor and the bases of sequences 1, 4, and 9. We do not consider bedding parallel shortening in this figure but will discuss it in the text.

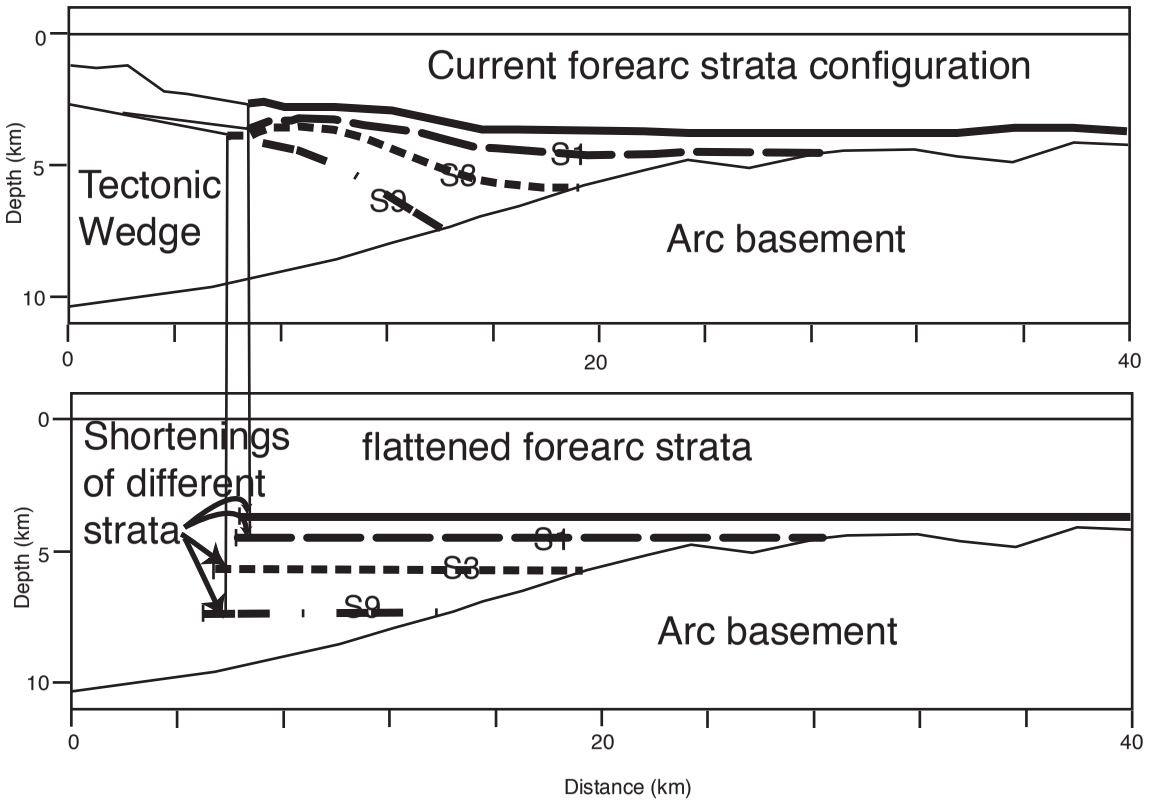
Current forearc strata configuration
Tectonic
Wedge
S1
S3
S9
Arc basement
Depth (km)
0
5
10
0
20
40
Shortenings
of different
strata
flattened forearc strata
S1
S3
S9
Arc basement
Depth (km)
Distance (km)

Figure 2.5: Gravity data at the latitude 20.9^{o}N from Hsu et al. (1998) is marked by solid line. It is very similar to the gravity data collected on board R/V Ewing, marked by the circled line, which lacks the portion on the trench side. For comparison, we added the gravity data along the Vema line at latitude of 20.2^{o}N. We have shifted the anomaly horizontally and vertically for comparison. Note the low gravity anomaly over the backthrust domain in the V3618.49 line. To correlate the gravity anomaly with geologic features, see figures 2.6, 2.7, 8 and 2.9.

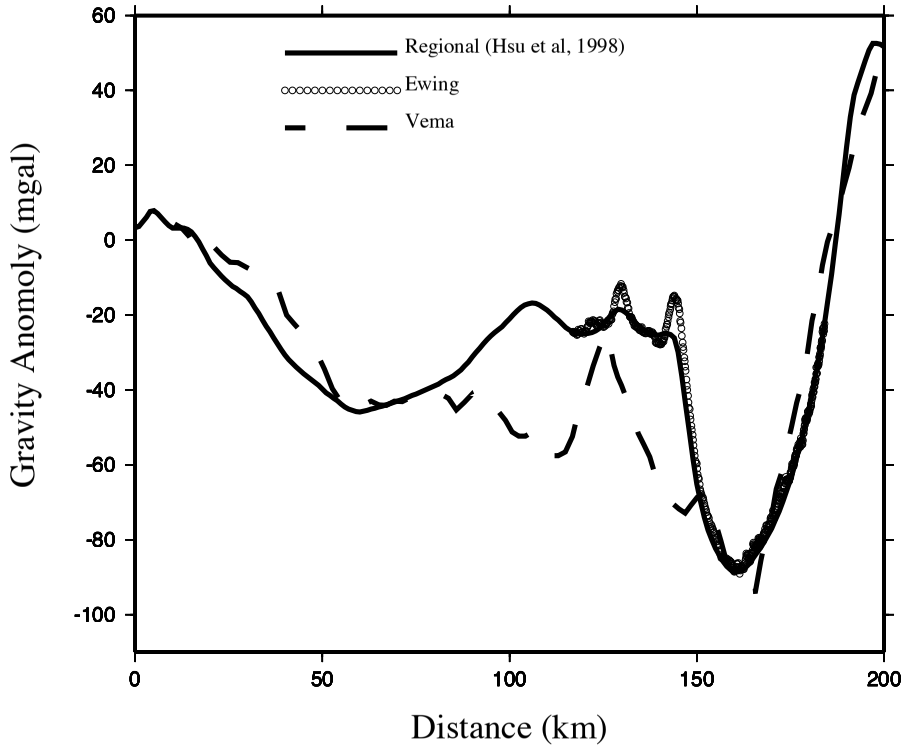
Regional (Hsu et al, 1998)
Ewing
Vema
Gravity Anomoly (mgal)
Distance (km)
60
40
20
0
-20
-40
-60
-80
-100
0
50
100
150
200

Figure 2.6: Forearc geometry and density along the Ewing line for the gravity modeling. In the upper panel, the circles are the observed free-air gravity anomaly from Hsu et al. (1998). The thick line is the predicted gravity anomaly from the preferred model. The thin line is the result from a deeper slab model. In the lower panel, seismicity from the Bulletin of the International Seismological Centre Database (time span 1915-2000, marked as dots) and CNSS (time span 1960-1997, marked as stars) catalogs in the region within 35 km of the Ewing lines are plotted as circles for reference. The magnitudes of these earthquakes range from Ms=4.5 to 6.5. The thick lines show the geometry of our preferred model while the thin lines show a model from a sensitivity test using a steeper, deeper slab. The forearc basin in the rectangular outline is expanded to better show the density structures. The accretionary prism is modeled as being composed of three domains, a lower slope domain near the trench (D=2.3 g/cm^3), a upper slope domain making the offshore Hengchun Ridge (D=2.42 g/cm^3 for the top layer and D=2.52 g/cm^3 for the bottom layer), and a backthrust domain along the rear of the prism that includes the tectonic wedge (D=2.85 g/cm^3). Forearc strata have densities ranging from 2 to 2.38 g/cm^3, based on the results from interactive velocity analysis.

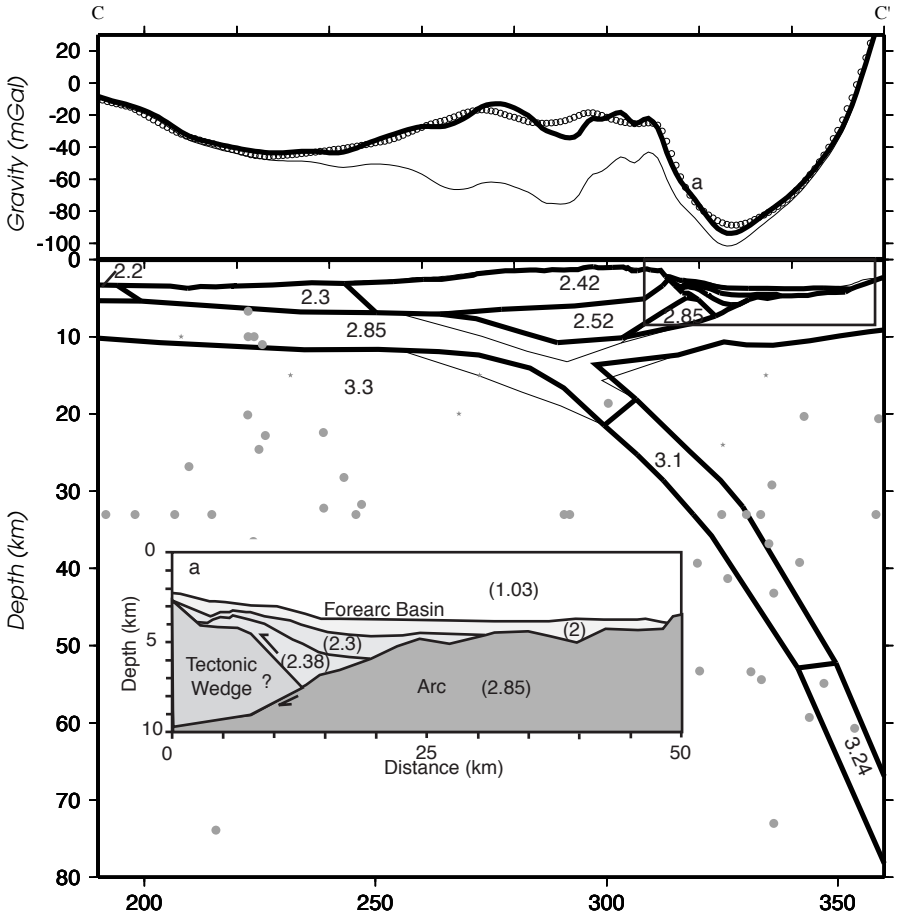
C
C'
Gravity (mGal)
20
0
-20
-40
-60
-80
-100
a
2.2
2.3
2.42
2.52
2.85
2.85
3.3
3.1
3.24
Depth (km)
0
10
20
30
40
50
60
70
80
200
250
300
350
a
(1.03)
Forearc Basin
(2)
(2.3)
(2.38)
Tectonic
Wedge
?
Arc
(2.85)
Depth (km)
0
5
10
0
25
50
Distance (km)

Figure 2.7: Shallow density model overlaying reflection profile from line EW9509.49. The upper 2 panels show results from density sensitivity tests by perturbing ±0.3 g/cm^3 of the top and bottom layers of the upper slope domain and the high-density block in the tectonic wedge, and the 3 layers in the forearc strata.

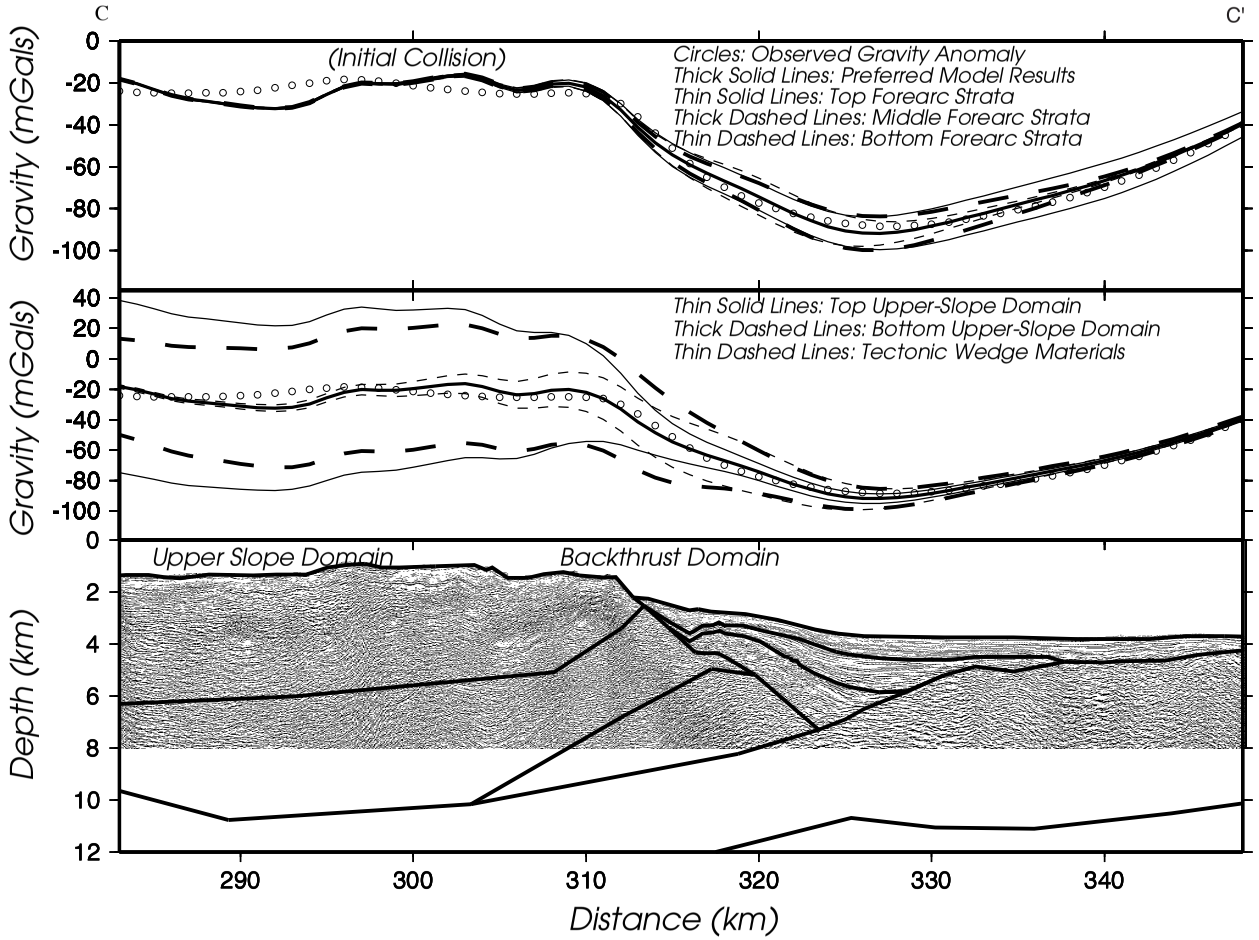
C
C'
(Initial Collision)
Circles: Observed Gravity Anomaly
Thick Solid Lines: Preferred Model Results
Thin Solid Lines: Top Forearc Strata
Thick Dashed Lines: Middle Forearc Strata
Thin Dashed Lines: Bottom Forearc Strata
Gravity (mGals)
0
-20
-40
-60
-80
-100
Thin Solid Lines: Top Upper-Slope Domain
Thick Dashed Lines: Bottom Upper-Slope Domain
Thin Dashed Lines: Tectonic Wedge Materials
Gravity (mGals)
40
20
0
-20
-40
-60
-80
-100
Upper Slope Domain
Backthrust Domain
Depth (km)
2
4
6
8
10
12
290
300
310
320
330
340
Distance (km)

Figure 2.8: The gravity modeling across subduction zone in the vicinity of line V3618.49. The geometry of the accretionary prism is based on the work by Nguyen (1998). Note the tectonic wedge is mainly composed of low density materials in this model. Similar to Figure 2.5, we have used thick lines to represent the model and the predicted gravity anomaly from our preferred model, while thin lines are for a steeper slab model plotted for reference. The range of the magnitudes of the earthquakes from (ISC and Harvard catalogs) is from Ms=4.3 to 6.5.

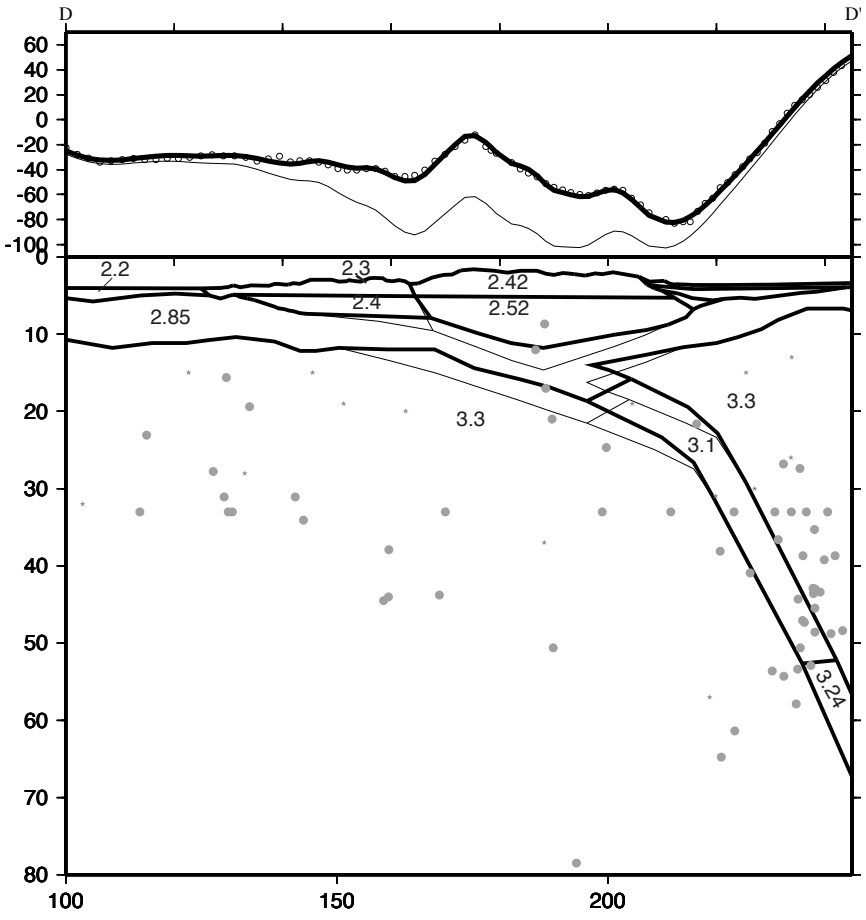
D
D'
60
40
20
0
-20
-40
-60
-80
-100
0
10
20
30
40
50
60
70
80
100
150
200
2.2
2.3
2.42
2.4
2.52
2.85
3.3
3.3
3.1
3.24

Figure 2.9: Shallow density model overlaying reflection profile from Vema line V3618.49. In the upper panel, the circles are the observed gravity anomaly; the thick solid line is the preferred model; the thin solid lines, thick dashed lines, and thin dashed lines are the gravity anomalies result from perturbing ±0.3 g/cm^3 of the top, middle, and bottom forearc strata, respectively. In the middle panel, the thin solid lines and the thick dashed lines are the gravity anomalies from the density sensitivity tests by perturbing ±0.3 g/cm^3 of the top and bottom layers of the upper slope domain. The lower panel shows the geometry of the density model superimposed on reflection data. The small dots are the seismicity from ISC and Harvard catalogs.

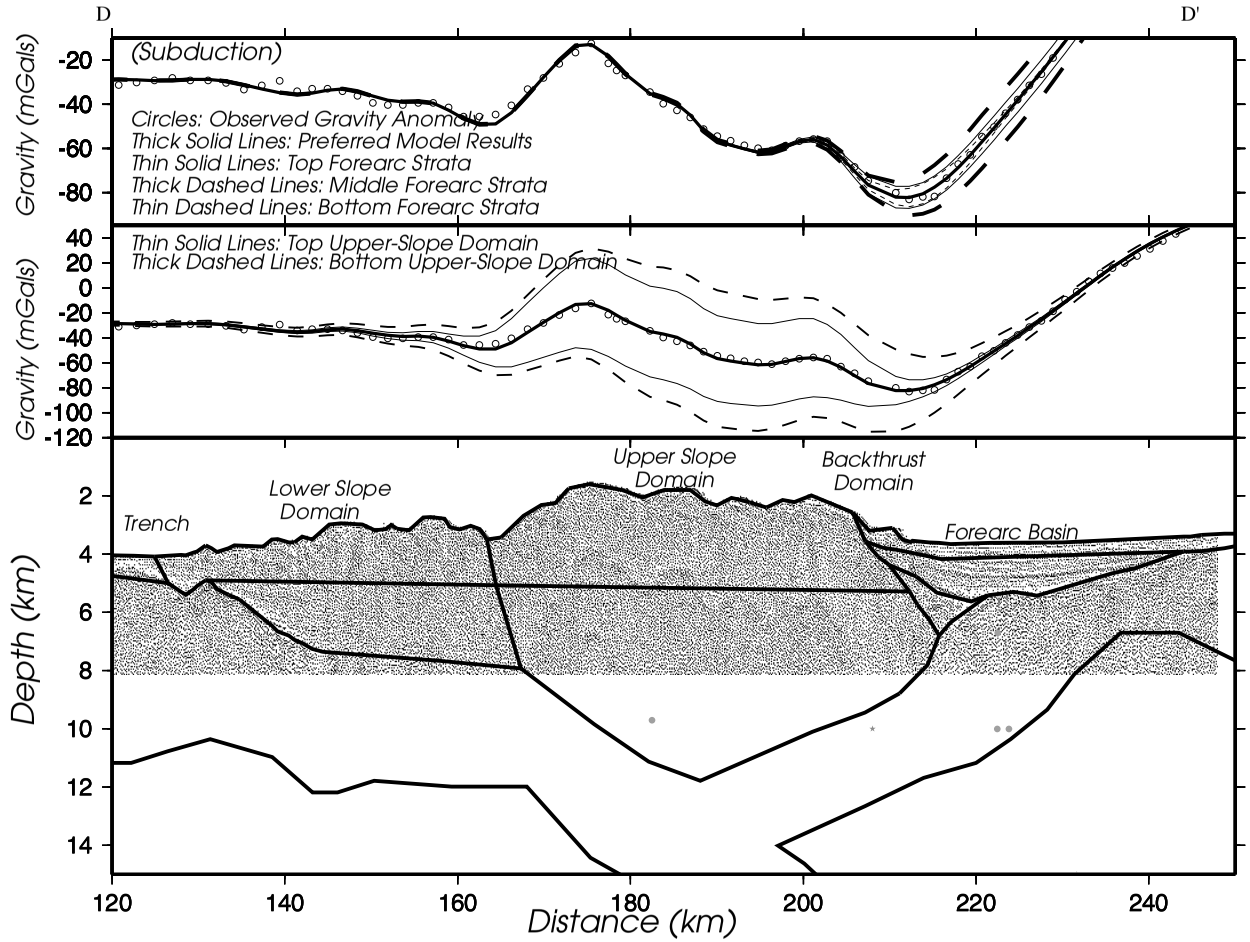
D
D'
(Subduction)
Gravity (mGals)
-20
-40
-60
-80
Circles: Observed Gravity Anomaly
Thick Solid Lines: Preferred Model Results
Thin Solid Lines: Top Forearc Strata
Thick Dashed Lines: Middle Forearc Strata
Thin Dashed Lines: Bottom Forearc Strata
Gravity (mGals)
40
20
0
-20
-40
-60
-80
-100
-120
Thin Solid Lines: Top Upper-Slope Domain
Thick Dashed Lines: Bottom Upper-Slope Domain
Trench
Lower Slope Domain
Upper Slope Domain
Backthrust Domain
Forearc Basin
Depth (km)
2
4
6
8
10
12
14
120
140
160
180
200
220
240
Distance (km)

Chapter 3

Finite Source Process of the 1999 Taiwan (Chi-Chi) Earthquake Derived from a Dense Strong Motion Network

3.1 Abstract

The 1999 Chi-Chi earthquake (Mw=7.6)(20 September 1999, 17:47:15.9 UTC)(located at 23.853^{o}N, 120.816^{o}E, and depth of 7.5 km) inflicted severe regional scale damage to Taiwan. The strong motion wavefield was captured by a dense network of stations (with average station spacing of 5 km), which represents the most complete strong motion dataset to date to use to study the kinematic source process of an earthquake. We inverted velocity waveforms recorded by 21 stations for the spatial variation in slip on a planar fault model composed of 416 subfaults, each with a dimension of 3.5 km by 3.5 km. The fault model has a strike of N5^{o}E and a dip of 30^{o}E, and the inversion solves for the direction and magnitude of the slip. To account for possible temporal source complexity, we allowed each subfault to slip within 10 overlapping time windows, each with a duration of 3 sec. The results show that the source is composed primarily of three major asperities, the first of which is mainly dip slip, extending from the hypocenter to the northern end of the surface rupture. In this asperity, slip occurred in two pulses separated in time by 5 sec. The dislocation rise time

for each pulse is short (3-4 sec), yielding an approximate average slip velocity of 80 cm/sec. The second asperity is located at shallow depth near the northern end of the rupture where very large ground velocities were observed. This asperity is on average oblique and shows a temporal rake rotation from pure dip-slip to strike-slip. The rotating rake suggests a low initial shear-stress on the northern end of the fault. Slip in this asperity is dominated by a large pulse with a dislocation rise time of 8 sec. A station near the northern end of the surface rupture recorded a peak velocity of 390 cm/sec, which we find to be due to the constructive interference of energy radiated from the first two asperities. The third asperity is located south of the epicenter. The total moment from the three asperities is 4.1×10^{27} dyne-cm, which was released over a period of 30-35 sec within an area of 900 km^2. Synthetics calculated from the three-asperity model explain 85% of the data and represent 98% of the total variance reduction. Our results indicate that slip is confined to the shallow region of the fault, deep slip patches are less constrained, and that the slip distribution may be representative of fault segmentation along the Chelungpu fault system.

3.2 Introduction

The 1999 Chi-Chi earthquake (Mw=7.6)(20 September 1999, 17:47:15.9 UTC)(located at 23.853^{o}N, 120.816^{o}E, and depth of 7.5 km) inflicted severe regional damage to the island of Taiwan. It also generated the most complete near source strong motion dataset available with an average station spacing of 5 km. Combined with the considerable volume of geologic and geophysical data collected in this region over the

past decades, this event provides an excellent opportunity to study the rupture process of a large earthquake and its relation to regional tectonics.

The Chi-Chi earthquake has a predominantly thrust focal mechanism (Figure 3.1; strike = 5^{o}, dip = 34^{o}, and rake = 65^{o}) derived from the first motions of the strong-motion records (Chang et al., 2000). Teleseismic solutions (strike = 37^{o}, dip = 25^{o}, and rake = 96^{o}; Harvard centroidal moment tensor [CMT]) and (strike=26^{o}, dip = 27^{o}, and rake = 82^{o})(Yagi and Kikuchi, 1999) compare well, but show some variation, which may be due to coseismic rake rotation or a non-planar fault surface. Surface slip measurements indicate variation in rake along an 80-km N-S-trending surface rupture along Chelungpu Fault (Central Geological Survey [CGS], 2000). The surface rupture was mapped from Chusan (Bamboo mountain) to the vicinity of Shanyi (Figure 3.1a) where it bends east and develops a complex en echelon pattern. Field observations also show that the greatest surface offset (greater than 8 m vertically) occurred near the northern end of the fault (CGS, 1999). Coincidentally, Shanyi (Figure 3.1a) is also the end of a previously identified seismic belt that extends 40 km SE to Puli (Wu and Rau, 1998, Rau and Wu, 1998; Lin, 2000).

The strong motion data recorded by the Taiwan Strong Motion Instrumentation Program (TSMIP) of the Central Weather Bureau (CWB) (Lee et al, 1999) shows evidence of strong northward directivity judged by the larger Horizontal Peak Ground Velocity (HPGV) to the north then to the south (Figure 3.1b). This effect is also evident in the horizontal peak ground acceleration (HPGA) on the footwall. In addition, footwall

stations close to the surface break have HPGA values less than 300 cm/sec^2 while the hangingwall stations have HPGA values greater than 500 cm/sec^2. This pattern is seen to extend 60 km north of the northernmost surface rupture. The hanging-wall amplification is less pronounced in HPGV, indicating it is frequency dependent because the integration to velocity from acceleration enhances lower frequency components. The highest HPGA (1100 cm/sec^2) is located close to the epicenter in the hanging wall on the southern segment. However, the HPGV increased northward on the hanging wall until it reached the highest value (390 cm/sec) at the northern end of the surface rupture where there is greater than 8 m vertical offset. The spatial separation between HPGA and HPGV suggests that there are differences in the rupture dynamics of the northern and southern ends of the fault, where in the north energy was radiated at relatively lower frequency compared to the south. The damage in this region is mainly due to the surface rupture and strong ground motion (Chiu and Huang, 2000). The HPGA and HPGV also indicate that there might be strong 3D path effects, which would be anticipated from the tomographic results of Cheng (2000). In fact, stations situated in sedimentary basins do show larger amplitudes and greater waveform complexity.

Yagi and Kikuchi's (1999) preliminary teleseismic inversion, reported on their website, showed a northward rupture propagation. Ma et al. (2000) inverted the strong motion, teleseismic, and GPS data and found the rupture was complex with variable slip direction and rupture velocity, and these results are consistent with the results of Mori et al, (2000) using teleseismic data, and with those presented in this study. Yagi and Kikuchi (2000) inverted strong motion, teleseismic, and GPS data and found a

heterogeneous slip rate. They also identified three asperities on the fault: one 10 km west of the epicenter, one 20 km north, and one about 40 km northwest and updip where large surface offsets were observed. Preliminary studies indicate a complex spatial and temporal source process with relative low rupture velocity (< 2.5 km/sec) and long dislocation rise time (Chi et al., 2000; Ma et al., 2000; Mori et al., 2000; Wu et al., 2000; Yagi and Kikuchi, 2000). In order to better understand the earthquake rupture process, we have derived a finite source model using the strong motion dataset provided by CWB of Taiwan (Lee et al., 1999). The methodology used is similar to that of Hartzell and Heaton (1983), and used in recent studies of the Hector Mine earthquake in Southern California (Dreger and Kaverina, 2000, Kaverina et al., 2000). The objective of this study is to determine the slip distribution, the fault geometry, the kinematics of the rupture process, and to assess the resolution of the source parameters. We have conducted detailed sensitivity tests on station distribution, fault plane dimension, varying rake, rupture velocity, and also studied the contribution to the waveforms from each of the major asperities in our preferred model.

3.3 Finite Source Methodology

We used strong motion data to invert the representation theorem (equation 1) for finite source parameters (e.g. Hartzell and Heaton, 1983). The observed seismogram is related to the spatiotemporal integration of slip distributed on a plane where,

$$U_n(x,t) = \int d\tau \iint \left[\mu \hat{n}_i u_j(\xi,\tau) \right] \cdot G_{ni,j}(x,\xi;t-\tau) \, d\Sigma(\xi) \quad (1)$$

where U_n is the nth component of observed velocity, μ is the rigidity, $\hat{n}_i$ is the fault orientation unit vector, u_j is the fault slip, $G_{ni,j}$ is velocity Green's function, x is a vector describing the relative location of the source and receiver,ξ, τ are spatial and temporal variables of integration, and $d\Sigma(\xi)$ is the area differential, Σ is a function of the spatial variable ξ.

The subscript letter n refers to the ground motion component and i and j are orientation indices. The quantity $\mu \hat{n}_i u_j$ (x,t) is equivalent to m(x,t), which describes the spatial and temporal seismic moment tensor. $U_n(x,t)$ is the spatio-temporal slip information to be determined by inverting the data.

We use a linear least-squares inversion of observed velocity seismograms to compute the spatio-temporal slip distribution. Several constraining equations are also applied to improve the stability of the inversion. First, the slip is required to be everywhere positive. Second, a Laplacian smoothing operator is applied to minimize the fluctuation of slip in adjacent subfaults. The weight of the Laplacian operator is a free parameter, and we examine a range of values before settling on a weight that succeeds in providing a suitably smooth model that also results in a good level of fit to the waveform

data and scalar moment derived from long period data. Third, we use surface slip constraints, which are implemented by first projecting the measured surface offsets (CGS, 2000) onto the modeled fault plane. The difference between the projected observed slip, and slip on the corresponding subfaults is minimized. The surface slip constraint controls the distribution of slip in the shallowest row of the finite fault model, and has negligible impact on the deeper subfaults.

For each subfault we simultaneously invert for pure reverse dip-slip and left-lateral strike-slip. The vector sum of the two components then gives the total subfault slip and the slip direction. Following the approach of Hartzell and Heaton (1983) we use a multi-time window method to account for temporal heterogeneity in fault slip. This parameterization allows us to first assume a constant rupture velocity and a circular rupture front, as well as a constant dislocation rise time for a given time window. However, by allowing each subfault to rupture in subsequent time windows we allow the overall rupture velocity and rise time to vary spatially. For example, slip that occurs only in later time windows is interpreted as having a lower rupture velocity while slip that occurs in several consecutive time windows is interpreted as having a longer rise time. Each of the individual time functions are normalized to unit area so that they integrate to total slip for the given time window. We use a minimum time function of 3 sec, which is defined as an isosceles triangle, and each subsequent window is delayed by one-half the duration (1.5 sec). The summation of the integrated time function then results in the total slip for a given subfault, and the time window duration effectively defines the maximum corner frequency and controls the ability to model higher frequencies in the data.

3.4 Station Selection and Green's Function Computation

We used the strong motion data from the instrument-response-corrected ASCII files disseminated on CDROM by Lee et al. (1999). The acceleration data were integrated to velocity and filtered between 0.02 and 0.5 Hz before being re-sampled at 10 samples per sec. A total record span of 50 sec is used. Because there might be timing problems at some stations (Lee et al., 1999), we have done several tests to avoid stations with apparent timing-errors. First we aligned the acceleration seismograms to check the arrival-time moveout (Figure 3.2). There was only one obvious timing error among the 30 stations that we initially considered for the inversion, and this station was removed from consideration. In Figure 3.2 we compare the first P arrival time calculated from the 1D velocity model that we use to compute Green's functions (Table 3.1) with a record section of vertical component acceleration waveforms. Overall the mean deviation between the observed and predicted arrival times is -0.1 sec with a standard deviation of 1.4 s. In all cases the deviation is less than the duration of one time window (3 s), and therefore has minimal impact on the inversion results. The source of the arrival time scatter could be due to clock errors, lateral heterogeneity, and difficulty in observing the initial onset due to the emergent nature of the P waveforms. In addition, Huang (2000) produced an animation of the observed wavefield across the network. In that study time-shifts were applied to some of the original data to make the wave propagation spatially coherent, and self-consistent. We compared our unfiltered acceleration data with Figure 3.2 of Huang (2000) and found the timing differences are generally less than 1 s. We

also compared our data with the animation, and even though these data are filtered to periods between 10-20 s, we found reasonably good agreement. Based on the aforementioned results, we feel justified using the absolute timing for the 21 stations, and are confident that the 1D velocity model used to compute Green's functions is a good approximation to the average crustal structure.

We further culled the dataset to maximize azimuthal coverage without overweighing a particular azimuth (Figure 3.1a), and to remove stations, which appeared to be more strongly influenced by 3D heterogeneity. We examined particle motion plots for the entire dataset and compared them spatially with a recently available 3D tomographic model (Cheng, 2000). Several basin stations show large amplitudes and complex waveforms compared to adjacent hard rock stations. These basin stations were removed and replaced with a hard rock station if possible.

A frequency-wave number methodology written by Chandan Saikia (Saikia, 1994) was used to calculate a set of Green's functions based on the 1D velocity model provided in Table 3.1, and published in a recent 3D tomographic study by Rau and Wu (1995). This 1D model has been well tested by routine regional moment tensor studies of local and regional events (c.f. Kao and Cheng, 2000), and is shown in Figure 3.2 to agree well with the first arrival times of the data used in this study. Because of the large dimension of the fault model and the regional station coverage, Green's functions were calculated for a source-receiver range of 2 km to 200 km with an increment of 3 km, and for a source depth range of 2 to 17 km with an increment of 3 km. The calculated

Green's functions were filtered in the same manner as the data. Several stations are located close to the fault trace, less than the 2 km minimum Green's function distance. We note that the center point of the shallowest 3.5 by 3.5 km subfault is at a depth of 0.9 km and 1.5 km laterally from the surface rupture. Because the surface slip constraint controls slip in the shallowest row of subfaults, the range of Green's function distances and depths is appropriate for the small-distance shallow-depth subfault-station pairs.

3.5 Preferred Model and Sensitivity Analysis

The location of the surface rupture and its offsets used in our fault plane parameterization were based on the field investigation by the CGS (1999). Surface evidence indicates that the fault geometry of the mainshock was complex. However, to begin the source modeling we considered a single 112 km by 45.5 km single fault plane with a strike of N5^{o}E to separate the hangingwall stations from the footwall stations. The dip is 30^{o}E, based on a combined regional broadband network (BATS)/teleseismic study by Kao and Cheng (2000). The fault plane is composed of 416 subfaults, each with a dimension of 3.5 km by 3.5 km. Each subfault was permitted to rupture in any of 10 3-sec isosceles-triangle time windows, each separated by a 1.5-sec delay. However, we also examined simpler time models, which will be discussed shortly. For each time window both pure dip-slip and pure strike-slip are solved for. Ten time windows on 416 subfaults each with dip-slip and strike-slip components translates to 8320 unknowns. Forty-one 50-sec seismograms from 21 stations sampled at 10 sps were used in the inversion, and translates to 20,500 data points. The data are most certainly correlated, thus the actual

number of data is less. The surface slip data, smoothing, and slip positivity constraining equations provide stability in the inversion.

We performed more than 80 inversions to reach our preferred model (Figure 3.3), which is presented here to define its principle features. As Figure 3.3 shows there are 5 regions of the slip model designated by the letters A-E. These regions represent areas of moment release that appear to be distinct, and are herein referred to as asperities A-E. A detailed discussion of these features and the interpretation is provided in the later section (Interpretation of Preferred Model). Before discussing the interpretation it is instructive, however, to examine the sensitivity of the finite fault slip inversion to factors such as station selection, station geometry, style of slip, rupture velocity and rise time heterogeneity to determine, which of these features are robust.

3.5.1 Station Sensitivity

To examine the possibility of unmodeled 3D propagation effects at some stations and because of the possibility of unknown timing errors in the data (Lee et al., 1999) we conducted a Jackknife test to investigate the sensitivity of the inversion to each station. Our initial choice of stations was governed by a desire to maximize azimuthal coverage and was predicated on the data being consistent with Huang (2000), and the first-arrival travel-time moveout as described previously. The sensitivity of groups of stations, such as those located on the hanging block, the foot block, and the northern end of the surface

rupture was studied. In addition, the sensitivity of the inversion to rupture velocity, time heterogeneity, and slip direction was explored.

As previously discussed there is a pronounced footwall/hangingwall effect in the observed HPGA (Figure 3.1b), and we tested inversions using only stations located on either the footwall or hangingwall blocks. Having poor azimuthal coverage, the footwall station inversion results in extensive, excessive slip (averaging 6.1 m over the entire fault plane). The scalar moment is 1.75×10^{28} dyne-cm and the variance reduction (VR)[VR= $1- (\sum(\text{synthetics-data})^2/\sum(\text{data})^2)$] is 92%. The inversion using only the hanging block stations results in the same level of fit (VR=92%) although more stations were used. The average slip is 4.1 m, and the distribution is more coherent forming asperities similar to the preferred results (Figure 3.3), which uses 21 stations (Figure 3.1a). The scalar moment was found to be 7.46×10^{27} dyne-cm for this inversion. Figure 3.1b indicates that for HPGV the hangingwall amplification is not as strong, and it is not a factor in the inversion results. In fact, the derived scalar moment from the hangingwall stations is less than for the footwall stations. Thus it seems that the most important consideration is the completeness of the coverage. The hangingwall stations have greater azimuthal coverage and therefore provide greater constraint on the distribution of slip.

The largest HPGV and surface displacements were observed at the northern end of the surface rupture. Station TCU068 recorded a HPGV of 390 cm/sec and is sited on the hangingwall close to the location of the maximum surface offset (8 m vertically). When this station is omitted from the inversion, the slip model is largely unchanged,

however, the level of slip in asperity B is reduced by half. Other nearby stations such as TCU029, 045, 052, 128, 065, 072, and 071 were also found to constrain asperity B (Figures 3.1a, 3.3).

The stations that control slip in the middle of the fault include TCU052, 065, 068, 071, 072, 075, 074, 079, 089, 078, and 128 (Figure 3.1a). Most of these are located on the hanging block above the rupture plane. These stations were found to have two important effects. First, they resolve heterogeneity within asperity A (Figure 3.3), and second, they suppress slip on the deeper portions of the model (e.g. asperities D and E). Additionally, stations HWA056, 058, and 032 are located on the hanging block to the east of the rupture plane (Figure 3.1). These stations were found to provide an important constraint on the deeper slip where the net effect was to suppress slip in asperities D and E.

At the southern end of the surface rupture and the fault model, stations CHY024, 028, 035, 074, and 080 require slip to be located to the south of the epicenter (asperity C in Figure 3.3). These stations also seem to have moderate sensitivity to asperity A and almost no sensitivity to asperity B. Some slip south of the epicenter is consistent with the results of Yagi and Kikuchi (1999).

In summary, the 21 stations that we used maximize azimuthal and footwall/hangingwall coverage of the rupture plane. These stations have been verified to be consistent with the P-wave traveltime from the 1D velocity model we have assumed

for the Green's functions, and do not appear to suffer from significant timing errors. This subset of stations resulted from the analysis of 30 stations, where stations exhibiting either significant timing errors or possible influence from 3D structure were replaced by another nearby station.

3.5.2 Slip Direction Sensitivity

Surface offsets and GPS data indicate that the slip in the earthquake was predominantly dip-slip, however, these data together with slightly oblique long-period thrust focal mechanisms suggest a significant strike-slip component. The finite source inverse method recovers variable slip direction by simultaneously solving for the reverse dip-slip and strike-slip (in this case left lateral) components. The vector sum of the two components gives the slip magnitude and direction. We first tested an inversion where slip was allowed to only be pure thrust. This calculation had the full 10-time window parameterization, and the results are shown in Figure 3.4a. For this inversion a VR of 80% was obtained, which is less than the 87% result obtained for the preferred model (Figure 3.3). This inversion recovered the slip in asperities A and B. Another inversion was performed, which allowed only left-lateral strike-slip. This inversion resulted in a VR of 60%, and recovered large slip at the base of the fault model. To examine the significance of the variable slip direction in the preferred model, we used the F test. Three F-ratios of the variances of the simplified models to the preferred model were computed. The variances of the simplified models were normalized by 20500 (data points) - 4160 (model parameters)=16340 degrees of freedom, and the variance of the

preferred model was normalized by 12180 degrees of freedom (representing twice the model parameters). The F-statistics of the preferred model to the pure dip-slip and strike-slip models are 1.52 and 3.06, respectively, and both exceed the critical F-value of 1.04 representing statistical significance greater than the 99th percentile assuming uncorrelated data. The data are certainly correlated, however, and the actual significance level is less. Nevertheless our detailed analysis of the velocity seismograms presented later and other independent data sets indicate that oblique slip is required.

3.5.3 Rupture Velocity Sensitivity

Rupture velocity sensitivity for the 10-time window parameterization was investigated (Figure 3.5) and we found that a value of 2.6 km/s gave the largest variance reduction, although there is a wide range (2-2.9 km/s) that also gave good results. Values of rupture velocity less than or greater than the optimal value tend to rearrange slip in time, where slower rupture velocities produce large slip in the early time windows and faster values tend to map slip to later times. Generally we find that the data require a substantial time delay in the occurrence of major slip. Asperities A, B, C, and D are observed in all runs where the rupture velocity is altered, although there is some variation in the distribution of slip between the asperities.

3.5.4 Dislocation Rise Time Sensitivity

Our preferred model has 10 time windows to account for rupture velocity and dislocation rise time variation. To establish a baseline we performed an inversion with only one time window. We used one 3 sec window that ruptures upon the arrival of a circular rupture front propagating at 2.6 km/sec, and obtained a variance reduction of -23 %. By adding a 7.5-sec delay on the rupture time to account for the delay in arrival of larger amplitude energy as observed in the raw accelerograms (Figure 3.2) the VR increased to -2.9 %. Increasing the dislocation rise time from 3 sec to 6 sec increased the VR to 43% and a dislocation rise time of 12 sec gave VR=32 %. All of these simplified inversions fail to adequately explain the data, although they do demonstrate that the data favors a dislocation rise time of approximately 6 s. The F statistic for the best single time window run (dislocation rise time of 6 seconds) with respect to the preferred model is 4.42. The improvement in fit over the critical F value (F=1.04) indicates that the multiple time window inversion provides a very significant improvement in fit.

3.5.5 Forward Tests of Finite Source Model

To examine the resolution of the preferred model we simulated seismograms using only portions of the total model (e.g. regions bounded by white lines in Figure 3.3). Asperity A (Figure 3.6) released a moment of 1.53×10^{27} dyne-cm and contributed most to the synthetic waveforms at stations from the central part of the fault and to the south. For example, stations TCU071, 072, and 075 are modeled quite well using only the slip from asperity A. In comparison stations TCU039, 128, 068, and 052 are poorly modeled. Asperity B has a scalar moment of 1.3×10^{27} dyne-cm and contributes most to stations

near Shanyi (TCU068, 052, 128, 039, 029, 045). This asperity is shallow and is responsible for the large HPGV and static surface offsets. This asperity contributes to the later portions of seismograms located south of TCU052, and does not contribute at all to stations located south of the epicenter in the 50 sec that we model (c.f. Figure 3.7 and Figure 3.1a). Asperity C releases 7.6×10^{26} dyne-cm and contributes most to stations near Chusan. Asperity D contributed only to the waveforms at HWA058. There is no clear pulse from the forward modeling of asperity E.

Inspecting the forward-modeled waveforms we found that in-phase energy from asperities A and B enhanced the major northward pulse and resulted in the very high HPGV at TCU068. For the stations within latitudes 23.75^{o}N-24.05^{o} N asperity A contributed the early part of the waveform while Asperity B contributed the later part of the waveform. Stations near the SW corner of the fault plane required asperity C. Figure 3.8 shows the fit to the data for the model without asperities D and E (our preferred model). The contribution from all slip except asperities D and E results in a variance reduction of 85.1%, compared with 87.1% for the total slip model, showing that only 2% improvement in fit came from asperities D and E. Thus about 98% of the total variance reduction comes from slip in shallow asperities. The small waveform contribution from asperities D and E and their effect of elevating the scalar moment over the long-period estimates leads us to caution their interpretation.

3.6 Interpretation of the Preferred Model

In the previous section we found that with the available station coverage we can resolve the slip in asperities A-C of the preferred model (Figure 3.3), and that slip in asperities D-E contributes little to the fit to the velocity waveforms. Additionally, we found that models that allow for variable rake, and multiple time windows significantly improve the fit to the data. In this section, we examine these features in more detail and interpret the results.

The slip in each of the 10 time windows is shown in Figure 3.9. Asperity A had 1 m of slip that ruptured in the first two time windows. The slip then subsided until the sixth time window (9 seconds later), when the major rupture occurred. Asperity B was found to be very complex and showed temporal rake rotation. It initiated at depth in the early time windows, and the rake rotates from mainly strike-slip to dip-slip. In the sixth time window the shallow patch started to rupture with initially pure reverse slip, which is seen to rotate to strike-slip though the time windows 7-9. The total slip shown in Figure 3.3 is obtained by summing the contributions from each of the time windows. The total slip near the hypocenter is about 8 m. Near the northern end of the fault it reached 23 m, however, it is concentrated on a single subfault. Asperity C reached a peak of 3 m of slip.

The dislocation rise times at four locations (Figure 3.3) are studied in detail (Figure 3.10). Using a rupture velocity of 2.6 km/sec, all of them showed an 8-10 sec delay except the one at the hypocenter. Location 1 near the maximum slip site of asperity B showed very high particle velocity (240 cm/sec) that is comparable to the maximum recorded HPGV of 390 cm/s at station TCU068. At this site the dislocation started 28

sec after the origin time, and has a dislocation rise time of about 8 sec. Location 2 is along the boundary between asperity A and asperity B. It shows a similar pattern to location 1 but with lower peak velocity (86 cm/sec) and 5-sec dislocation rise time. Location 3 within asperity A shows a peak particle velocity of 168 cm/s and 10 sec delay. The dislocation rise time is about 5 sec. At the hypocenter (Location 4) there were two pulses 5 sec apart with a peak particle velocity of 110 cm/s. On average the particle velocity ranges from 70-250 cm/sec, and the stress drop ranges from 2 to13 MPa for the primary asperities. Both quantities seem to increase northward. The different HPGA/HPGV ratios in the northern part of the fault compared to the south are probably related to the differences in moment rate. Figure 3.10 shows that the duration of the pulses in the southern half of the fault is shorter (approximately 2-8 sec, Location 3) while on average they are longer in the northern half of fault (4-12 sec). The rupture process seems more complex in the south, where two source pulses are observed. The relatively short duration of the 2 pulses may contribute to proportionally more high frequency radiation, thus leading to the large observed HPGA. In contrast, the northern end of the fault had only a single large pulse, which for some stations is partly due to constructive interference from both asperities A and B, producing the high HPGV in that region. The overall duration of the single pulse is longer, leading to a lower corner frequency and lower HPGA.

Next, we compare the moment rate function, spatial variation of the dislocation rise time, and perturbations to the rupture front (Figure 3.11). The moment rate function is derived by integrating the moment distribution in the space domain, where this

duration is the convolution of the dislocation rise time and rupture time integrated over the fault surface. There is a weak initiation, which is seen in the raw accelerograms (Figure 3.2). After the first 5 sec the moment rate is seen to increase steadily and peaks between 19 and 25 sec after the origin time. The moment rate function then decreases rapidly. The low levels of moment rate at times greater than 35 sec may not be well resolved. The total moment of 4.1×10^{27} dyne-cm is about 53% of the moment derived from a teleseismic inversion study by Lee et al. (2000). However, it is larger than the 1.77×10^{27} dyne-cm of Kao and Chen (2000), 2.4×10^{27} dyne-cm of Yagi et al (2000), and 2-4 $\times 10^{27}$ dyne-cm of Ma et al.(2000). It is 21% larger than the Harvard CMT estimate (3.38×10^{27} dyne-cm). We speculate that the larger moment comes from our use of higher frequency velocity seismograms while Kao and Chen (2000), Ma et al. (2000), Yagi (2000) use displacement seismograms. Another possibility is due to the 1D model used for the Green's function calculation. Lack of low velocity layers at shallow depths will reduce the amplitude of the Green's function, thus increasing the slip magnitude (e.g. Wald et al., 1996). Complex 3D crustal velocity structure might also influence wave propagation paths, however, the site selection process in this study removed sites that either displayed or would be expected to have significant 3D influence.

The rise time was derived by counting the number of time windows that have continuous slip greater than 50 cm (Figure 3.11b). The results for each subfault ranges between 6-10 s, with little systematic variation. We have also plotted the wavefront time that includes the delay until slip in a single window exceeds 50 cm (Figure 3.11c). This figure shows the rupture velocity was variable and overall slower than 2.6 km/s.

The rupture front slowed substantially as it propagated into the region between asperities A and B, suggesting a change in the dynamic properties of the rupture. Asperity B exhibits a temporal rake rotation (Figure 3.9), which suggests that this part of the fault had a low initial stress and large stress drop (Guatteri and Spudich, 1998). Alternatively, it could be that the fault was strong and needed a dynamic perturbation to initiate the rupture. The rupture front is seen to delay as it reaches asperity B, suggesting that it has higher relative strength and a dynamic stress increase due to failure of other patches of fault needed to grow for asperity B to fail. (e.g. Ward, 2000). Apparently this change in the dynamics of the rupture process conspired to produce very large offsets and large particle velocities, but relatively low radiation at high frequencies (Figure 3.1). The interference of waves radiated from asperities A and B could also affect the spectrum and the HPGA and HPGV ratio.

Finally, the fault dimensions are important in the study of this earthquake because slip consistently occurred at the NE corner and the bottom of the fault plane model. To examine the resolution of the deep slip we extended the fault width by 25 more kilometers from the bottom and found that it resulted in unrealistically large slip (greater than 25 m). As the previous sensitivity tests showed, this large slip can be introduced by just small variation of waveform, and therefore with the available strong motion data, slip in asperities D-E is not well constrained. In fact, the addition of more stations to the east suppresses this slip without affecting the slip in asperities A-C. The northern bend of the surface rupture near asperity B could be related to the large slip along the Shanyi-Puli

belt. Such unmodeled complexity could result in the rake rotation that we obtained. Investigation of non-planar slip models will be the focus of future work.

3.7 Conclusion

We inverted the dense strong-motion data from the CWB to study the finite source process of 1999 Chi-Chi earthquake. More than 80 inversions using 41 velocity seismograms were performed and our best model is comprised of three shallow asperities, which account for 98% of the total waveform fit. Deeper asperities are poorly constrained and likely artifacts. Asperity A, mainly dip-slip, extends from the hypocenter to the northern end of the surface rupture. There are two pulses in this asperity separated by 5 sec, each with a duration of 3-4 sec. The particle velocity reaches 80 cm/sec. Asperity B, which is mainly left-lateral oblique slip, is confined within the region from the town of Puli to the northern end of the surface rupture. It is dominated by a large pulse with a dislocation rise time of 7 sec resulting in a particle velocity of 240 cm/s. The high HPGA near the epicenter may be due to the multiple short duration rupture pulses in that region. The high HPGV at the northern end of the surface rupture is related to the single long duration pulse, which in part results from the constructive interference of waves from both asperities A and B. The rotation of rake of asperity B suggests that this region of the fault had relatively low initial stress and large stress drop. However it may also be due to the assumption of a single planar fault geometry, although surface slip measurements (CGS, 2000) and GPS (Yu et al., 2001) indicate that oblique slip is required in this region of the fault. The observed northward directivity is mainly due to

Asperity B due to its significant strike-sip component. Asperity C is located south of epicenter and is comprised of many smaller patches of slip. The total moment from those three asperities is 4.1 x 10^{27} dyne-cm, released over a period of 30-35 sec. A range of rupture velocity between 2.0 and 2.9 km/sec provided good fit, with the best being 2.6 km/sec. The multiple time window analysis revealed that the rupture front slowed as it entered asperity B suggesting that it had low initial stress and required dynamic stress increases due to adjacent slipping patches of fault before failing (e.g. Ward, 2000), or that the actual rupture occurred on a surface different from the modeled planar fault. The slip distribution that we obtain is mainly confined within a triangular area bounded by the towns Shanyi, Puli, and Chusan that seems to correlate with topography and pre-event seismicity, and may be an expression of fault segmentation.

3.8 Acknowledgments

We thank the Central Weather Bureau for maintaining the strong motion network that made this study possible. We also thank Dr. Willie Lee and Professor Leon Teng for facilitating the prompt release of strong motion data. We are grateful to the Central Geological Survey for providing the surface rupture information. We thank David Schmidt for his review of this paper and constructive criticism. This research is partially funded by the Soong's Foundation fellowship. The author (WCC) wishes to thank Professors Dietrich and Kirchner for supporting his trip to Taiwan to investigate the surface faulting from their NSF grant EAR-0000893.

Figure 3.1.a. Topographic and location map. For the location of this figure, see the rectangular box in (b). The focal mechanism of Kao and Chen (2000) is predominantly thrust. The dots show the surface rupture mapped by the CGS (1999) that extends from Chusan to the vicinity of Shanyi where the surface rupture then bends eastward and forms en enchelon pattern. Some surface fissures were found at Puli. The locations of 21 (7 on the footwall and 14 on the hanging wall) stations used in our final inversion are shown as triangles. The letters A, B, C below the station names identify the asperities that contributed to the seismogram at that station (see section on Preferred Model and Sensitivity Analysis for details). There is a topographic low region bounded by the towns Shanyi, Puli, and Chusan. It is in this region we find that most of the slip was confined.

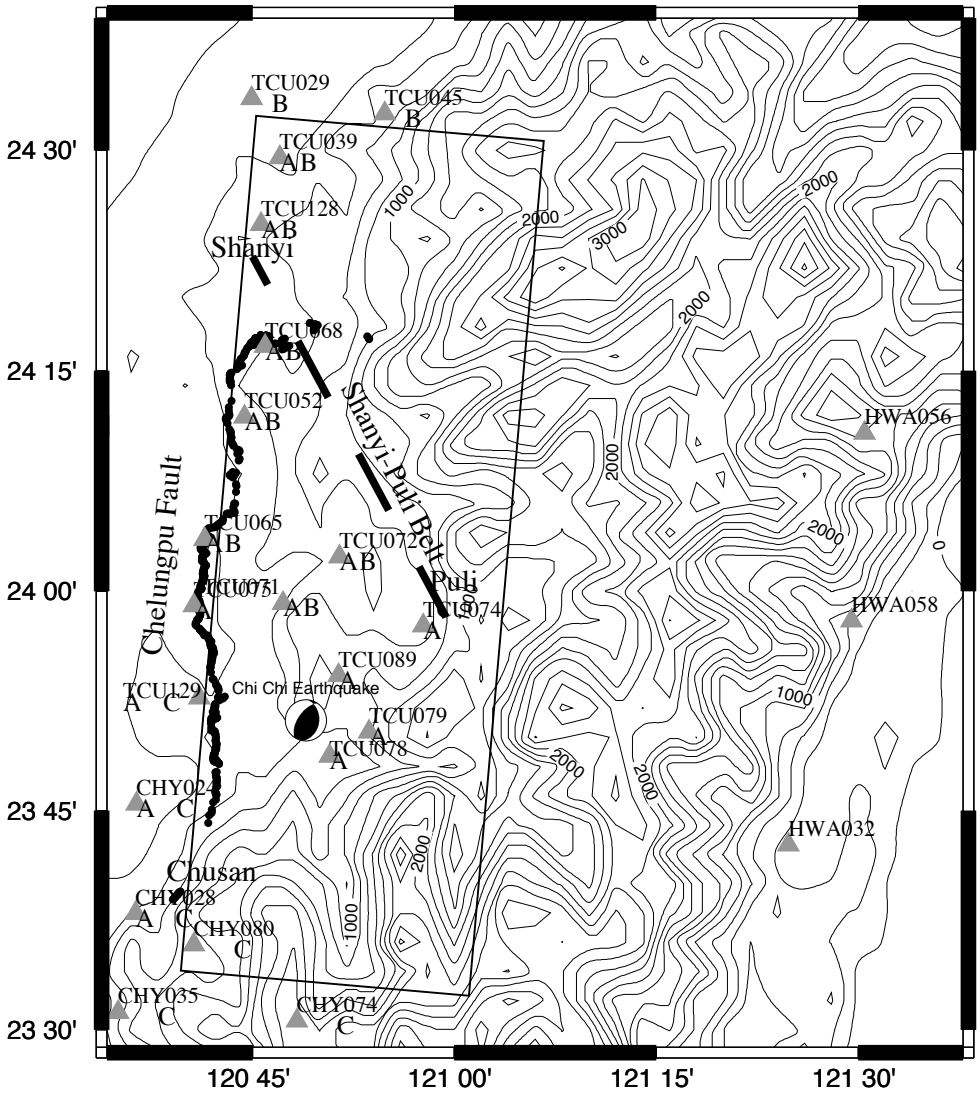
TCU029
B
TCU045
B
TCU039
AB
TCU128
AB
Shanyi
TCU068
AB
TCU052
AB
Shanyi-Puli Belt
Chelungpu Fault
TCU065
AB
TCU072
AB
Puli
TCU075
AB
TCU074
A
TCU089
A
TCU129
A C
Chi Chi Earthquake
TCU079
A
TCU078
A
CHY022
A C
Chusan
CHY028
A C
CHY080
C
CHY035
C
CHY074
C
HWA056
HWA058
HWA032
1000
2000
3000
0
24 30'
24 15'
24 00'
23 45'
23 30'
120 45'
121 00'
121 15'
121 30'

Figure 3.1b. The circles display the spatial distributions of HPGA and HPGV. The sizes of the circles are scaled according to the corresponding HPGA/HPGV values. The highest HPGA was recorded near the epicenter in the southern part of the surface rupture. There is a notable 200 cm/sec^2 increase in average HPGA at stations located close to the fault on the hanging block. The highest HPGV was located near the northern end of the surface rupture. The HPGV pattern clearly shows the effects of northward directivity. Examples of stations where lateral heterogeneity has a strong affect are shown by arrows.

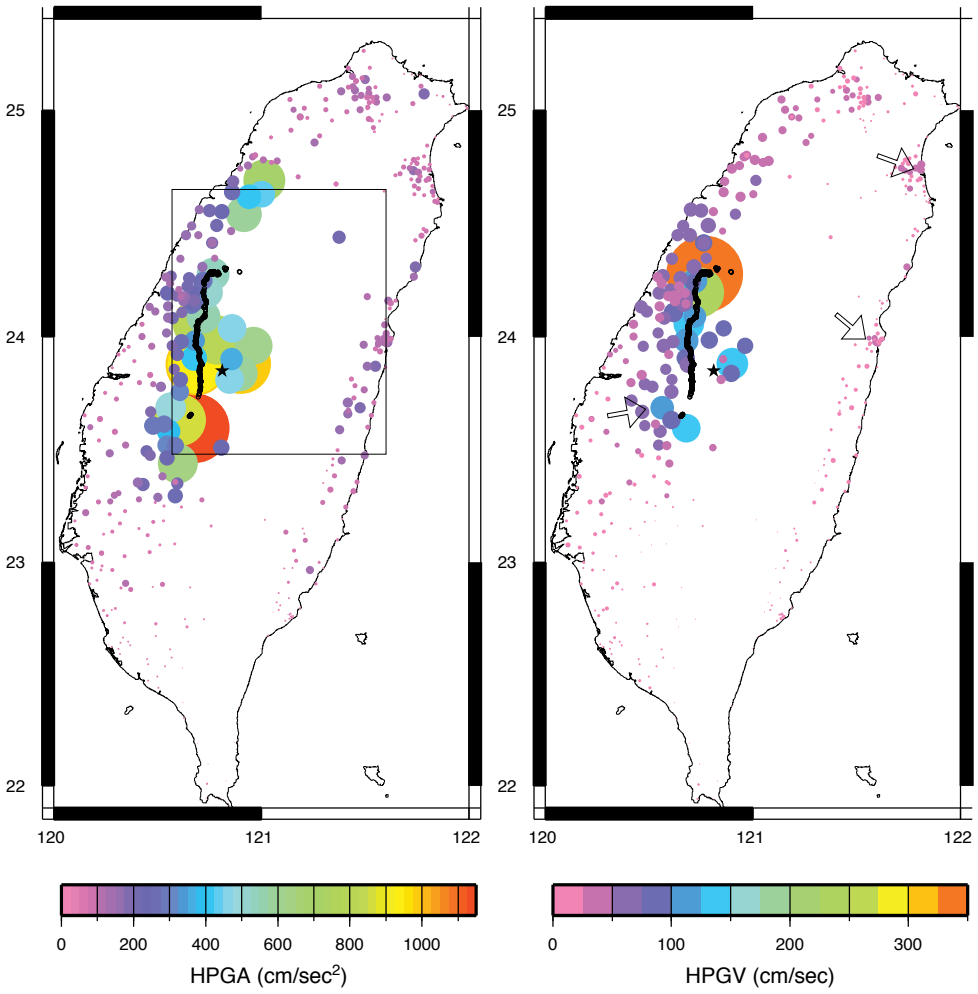
25
24
23
22
120
121
122
0
200
400
600
800
1000
HPGA (cm/sec^2)
25
24
23
22
120
121
122
0
100
200
300
HPGV (cm/sec)

Figure 3.2. A common-shot-gather plot was used to check for possible timing errors of the 21 stations we used for the finite source inversion. These waveforms are unfiltered vertical acceleration data. Each trace is scaled to emphasize the beginning of the record. The first P wave arrival-time curve is derived from the velocity model we used to calculate Green functions. The mean difference between the observed first arrivals and the traveltime curve is -0.1 ± 1.4 sec demonstrating that these stations do not have any serious timing errors.

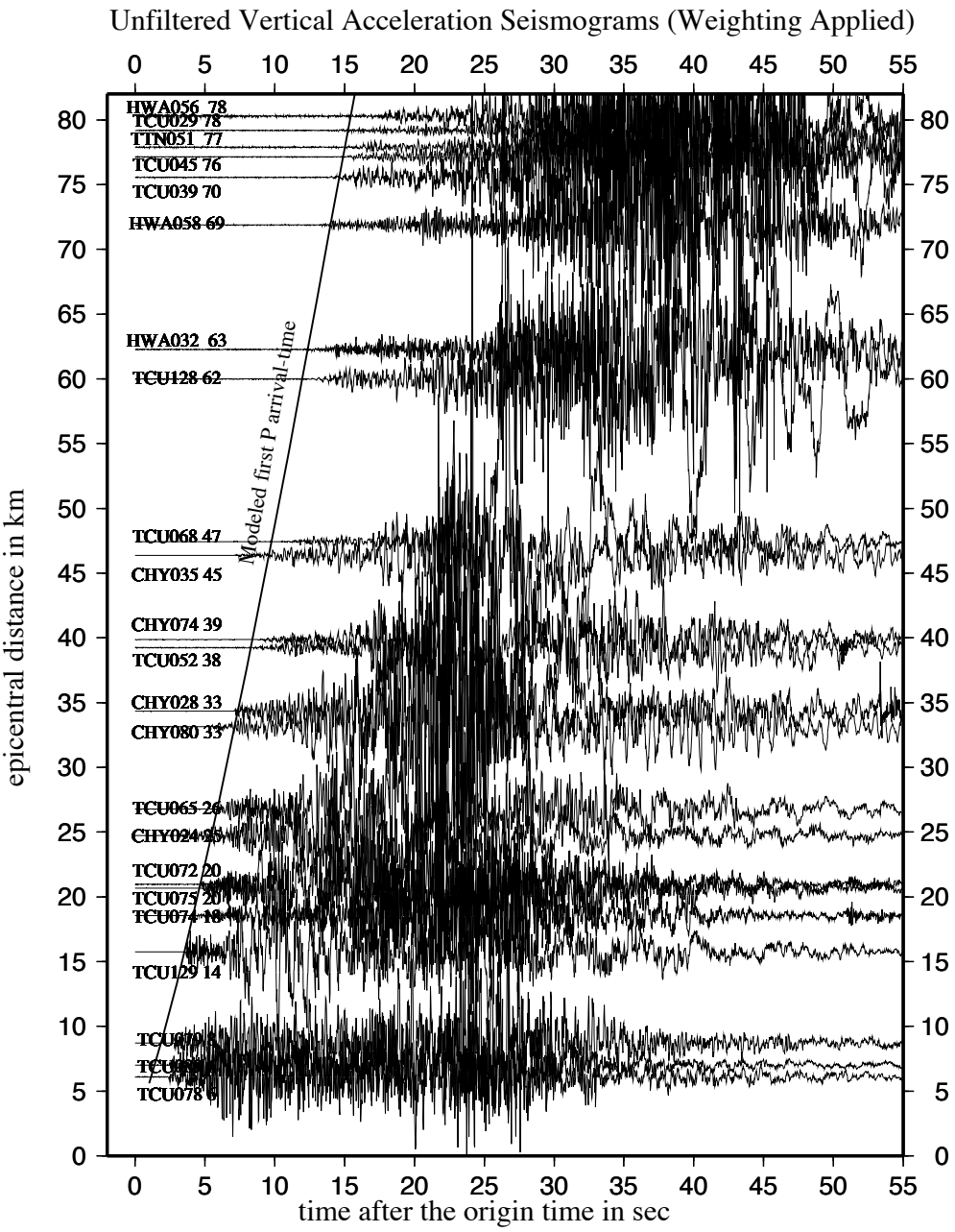
Unfiltered Vertical Acceleration Seismograms (Weighting Applied)
epicentral distance in km
time after the origin time in sec
Modeled first P arrival-time
HWA056 78
TCU029 78
TTN051 77
TCU045 76
TCU039 70
HWA058 69
HWA032 63
TCU128 62
TCU068 47
CHY035 45
CHY074 39
TCU052 38
CHY028 33
CHY080 33
TCU065 26
CHY024 25
TCU072 20
TCU075 20
TCU074 18
TCU129 14
TCU078 6

Figure 3.3. Best inverted slip model. A star denotes the hypocenter. There are five major asperities: asperity A is mainly dip-slip within the triangular zone bounded by the towns of Shanyi, Puli, and Chusan; asperity B is oblique-slip along the Shanyi-Puli belt; asperity C is trending NW-SE with oblique slip. Asperity D is dip-slip near Puli; and asperity E is strike-slip near the NE corner. Based on our analysis, the slip pattern from asperities A, B, C are well constrained but asperities D, E are inconclusive. Our preferred model only consists of asperities A, B, and C. A) dip-slip component, B) strike-slip component, C) vector plot showing the magnitude of total slip and the slip direction. Four locations where the dislocation rise time is investigated are labeled.

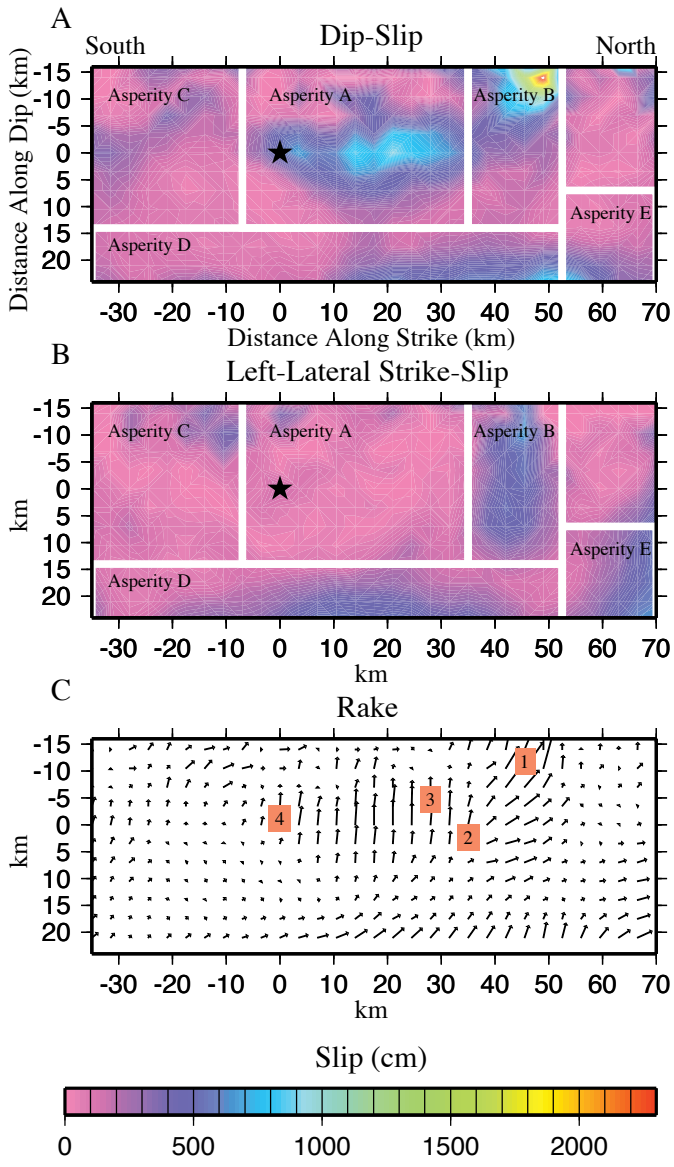
A
Dip-Slip
South
North
Distance Along Dip (km)
Asperity C
Asperity A
Asperity B
Asperity E
Asperity D
Distance Along Strike (km)
B
Left-Lateral Strike-Slip
km
C
Rake
1
2
3
4
Slip (cm)
0
500
1000
1500
2000

Figure 3.4. Rake sensitivity tests. For the inversion that only allowed up-dip slip we obtain a good fit and a variance reduction (VR) of 80%, compared with 87% for our best model. For this case, slip was resolved only in asperities A and B. For the inversion that only allowed left-lateral strike-slip we obtain a VR of 60% and slip is largely at the bottom of the fault plane.

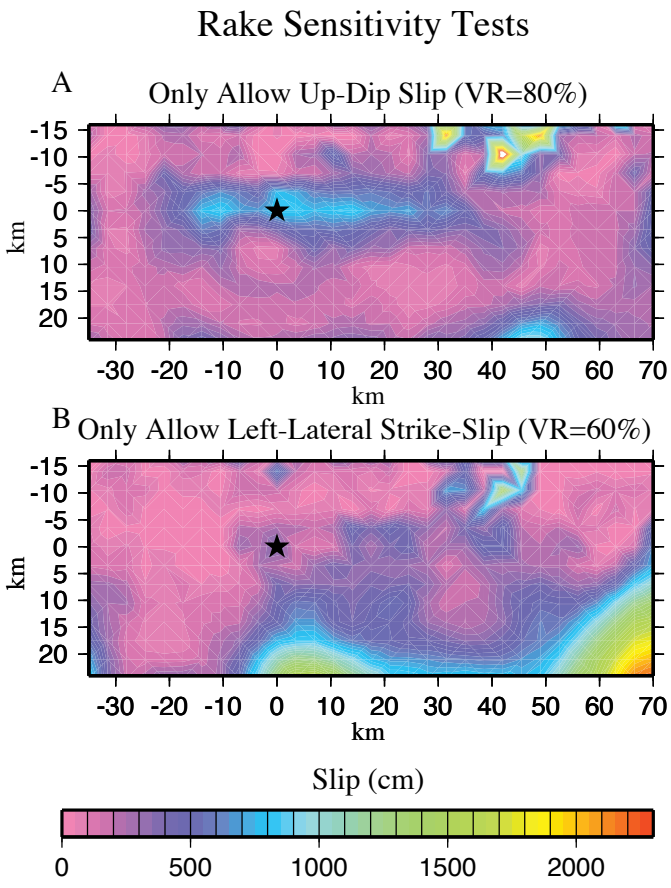
Rake Sensitivity Tests
A
Only Allow Up-Dip Slip (VR=80%)
-15
-10
-5
0
5
10
15
20
km
-30 -20 -10 0 10 20 30 40 50 60 70
km
B
Only Allow Left-Lateral Strike-Slip (VR=60%)
-15
-10
-5
0
5
10
15
20
km
-30 -20 -10 0 10 20 30 40 50 60 70
km
Slip (cm)
0
500
1000
1500
2000

Figure 3.5. Rupture velocity sensitivity. Rupture velocity is tested from 1.7 km/sec to 3.2 km/sec. Our preferred model has a rupture velocity of 2.6 km/sec.

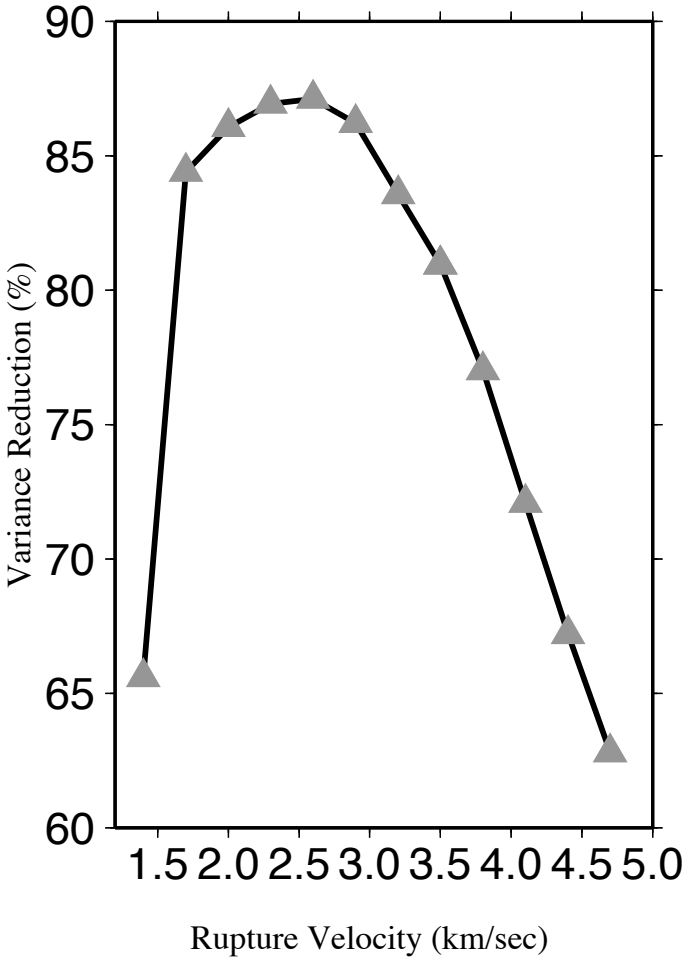
90
85
80
75
70
65
60
Variance Reduction (%)
1.5 2.0 2.5 3.0 3.5 4.0 4.5 5.0
Rupture Velocity (km/sec)

Figure 3.6. Synthetic velocity waveform (dashed lines) simulated using only asperity A. Solid traces are the recorded data. Most of the stations within the latitudes of 23.75 and 24.15 are mainly controlled by asperity A, especially TCU052 and 065. See Figure 3.1a for station locations.

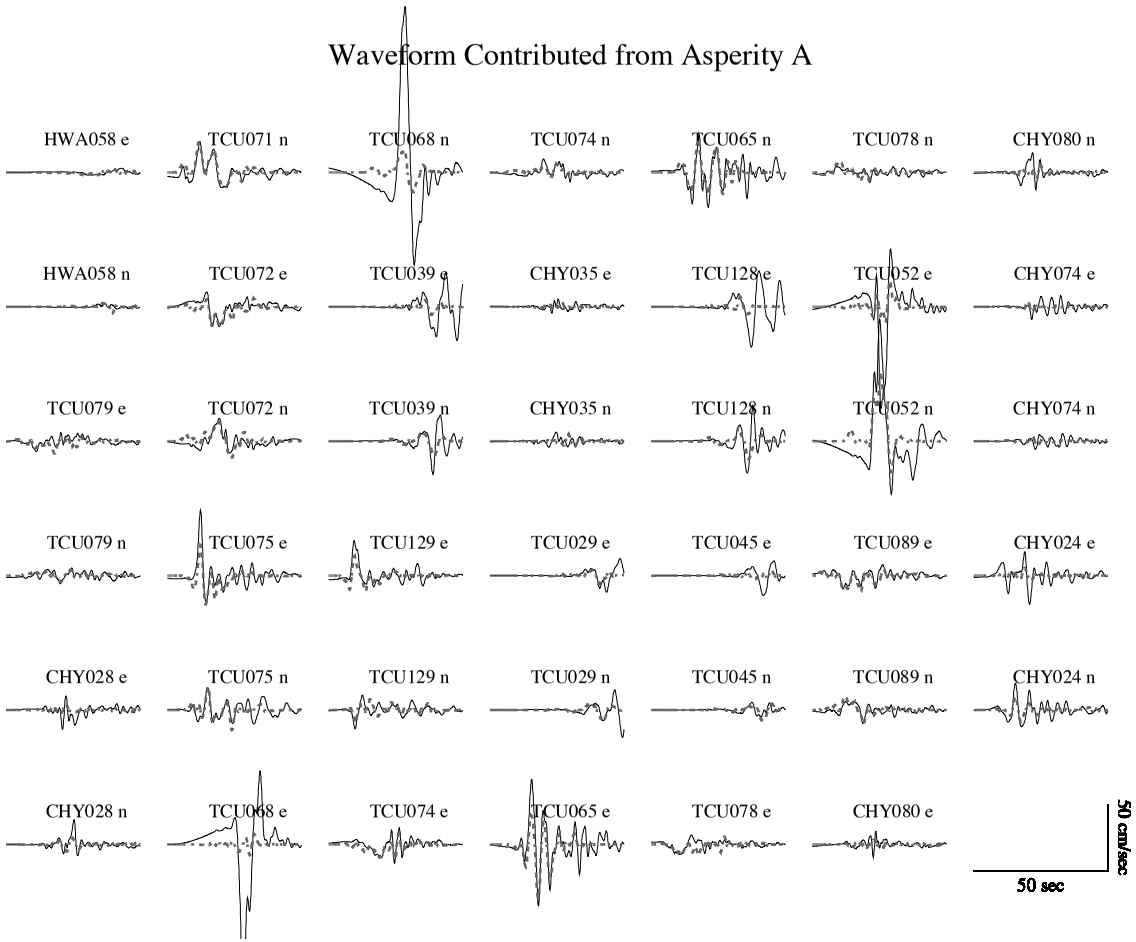
Waveform Contributed from Asperity A
HWA058 e
TCU071 n
TCU068 n
TCU074 n
TCU065 n
TCU078 n
CHY080 n
HWA058 n
TCU072 e
TCU039 e
CHY035 e
TCU128 e
TCU052 e
CHY074 e
TCU079 e
TCU072 n
TCU039 n
CHY035 n
TCU128 n
TCU052 n
CHY074 n
TCU079 n
TCU075 e
TCU129 e
TCU029 e
TCU045 e
TCU089 e
CHY024 e
CHY028 e
TCU075 n
TCU129 n
TCU029 n
TCU045 n
TCU089 n
CHY024 n
CHY028 n
TCU068 e
TCU074 e
TCU065 e
TCU078 e
CHY080 e
50 cm/sec
50 sec

Figure 3.7. Synthetic velocity waveform (dashed lines) simulated using only asperity B. Solid traces show data. Note that this asperity contributed major portion of the waveform at TCU068 and TCU052. Because there is a large strike-slip component at shallow depth, the synthetics show a very strong northward directivity effect. The stations that are north of this asperity have larger amplitudes than to the south at similar distance (e.g. TCU128 N component vs. TCU065 N component). This asperity contributed to the later portion of the waveform for many stations (e.g. TCU079, TCU075, TCU071, TCU065). See Figure 3.1a for the station locations.

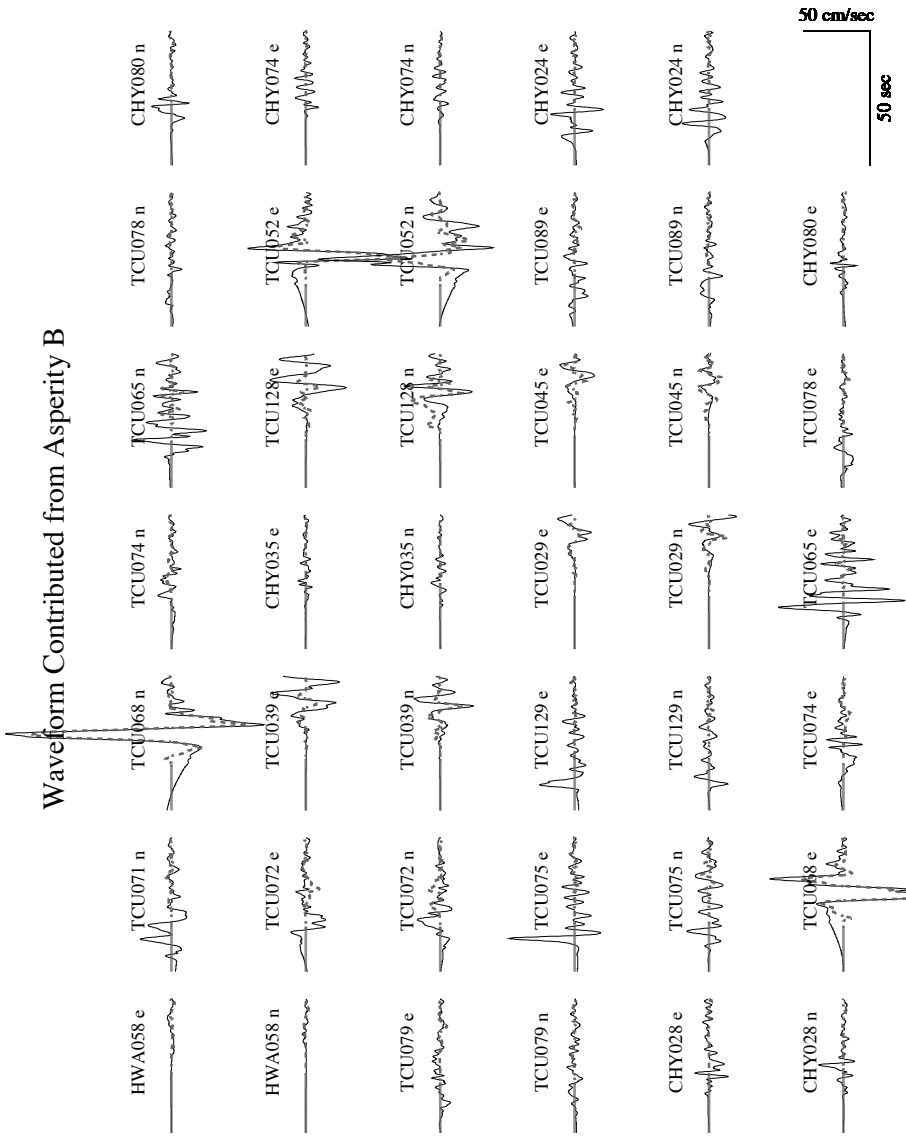
Waveform Contributed from Asperity B
HWA058 e
TCU071 n
TCU068 n
TCU074 n
TCU065 n
TCU078 n
CHY080 n
HWA058 n
TCU072 e
TCU039 e
CHY035 e
TCU128 e
TCU052 e
CHY074 e
TCU079 e
TCU072 n
TCU039 n
CHY035 n
TCU128 n
TCU052 n
CHY074 n
TCU079 n
TCU075 e
TCU129 e
TCU029 e
TCU045 e
TCU089 e
CHY024 e
CHY028 e
TCU075 n
TCU129 n
TCU029 n
TCU045 n
TCU089 n
CHY024 n
CHY028 n
TCU068 e
TCU074 e
TCU065 e
TCU078 e
CHY080 e
50 cm/sec
50 sec

Figure 3.8. Synthetic waveforms (dashed lines) from the model without asperities D and E. The fit is very good and the variance reduction between the synthetic and the observed data is 85%, compared with the variance reduction 87% obtained when the entire model is used. Thus 98% of the data is fit by waves radiated from asperities A-C. Asperities D-E are poorly resolved. Note the synthetics systematically under-predicted the first eastward pulse at stations located on the footwall near the surface rupture (TCU065, TCU075, TCU129).

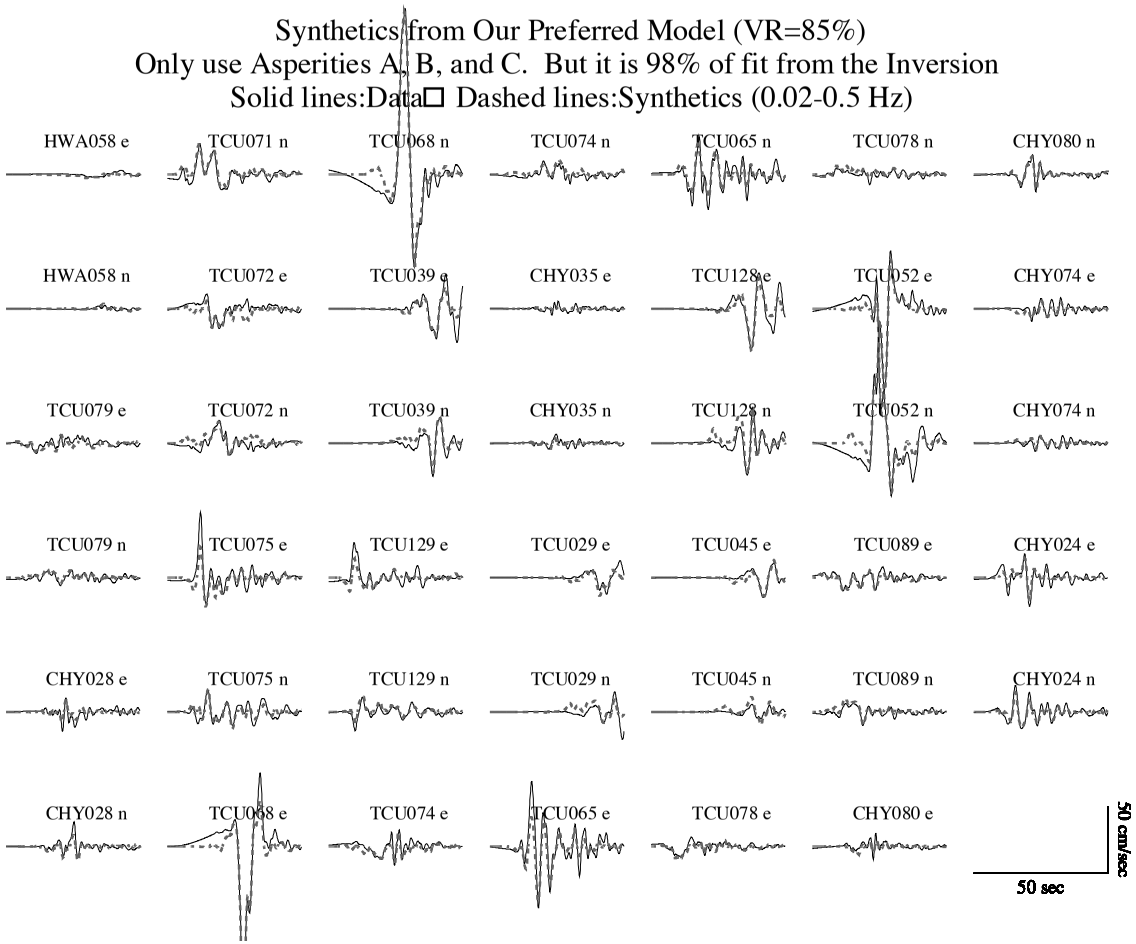
Synthetics from Our Preferred Model (VR=85%)
Only use Asperities A, B, and C. But it is 98% of fit from the Inversion
Solid lines:Data Dashed lines:Synthetics (0.02-0.5 Hz)
HWA058 e
TCU071 n
TCU068 n
TCU074 n
TCU065 n
TCU078 n
CHY080 n
HWA058 n
TCU072 e
TCU039 e
CHY035 e
TCU128 e
TCU052 e
CHY074 e
TCU079 e
TCU072 n
TCU039 n
CHY035 n
TCU128 n
TCU052 n
CHY074 n
TCU079 n
TCU075 e
TCU129 e
TCU029 e
TCU045 e
TCU089 e
CHY024 e
CHY028 e
TCU075 n
TCU129 n
TCU029 n
TCU045 n
TCU089 n
CHY024 n
CHY028 n
TCU068 e
TCU074 e
TCU065 e
TCU078 e
CHY080 e
50 cm/sec
50 sec

Figure 3.9. Slip vectors from the ten time windows (without asperities D and E). Asperity A has mainly dip-slip that started at the first two time windows. It then subsided for 7.5 sec before the second pulse started. Asperity B shows a rotation of rake from strike-slip to dip-slip to strike-slip, which might be related to a dynamic stress change during the rupture process, and low initial stress (Guatteri and Spudich, 1998). Asperity C shows mainly oblique slip.

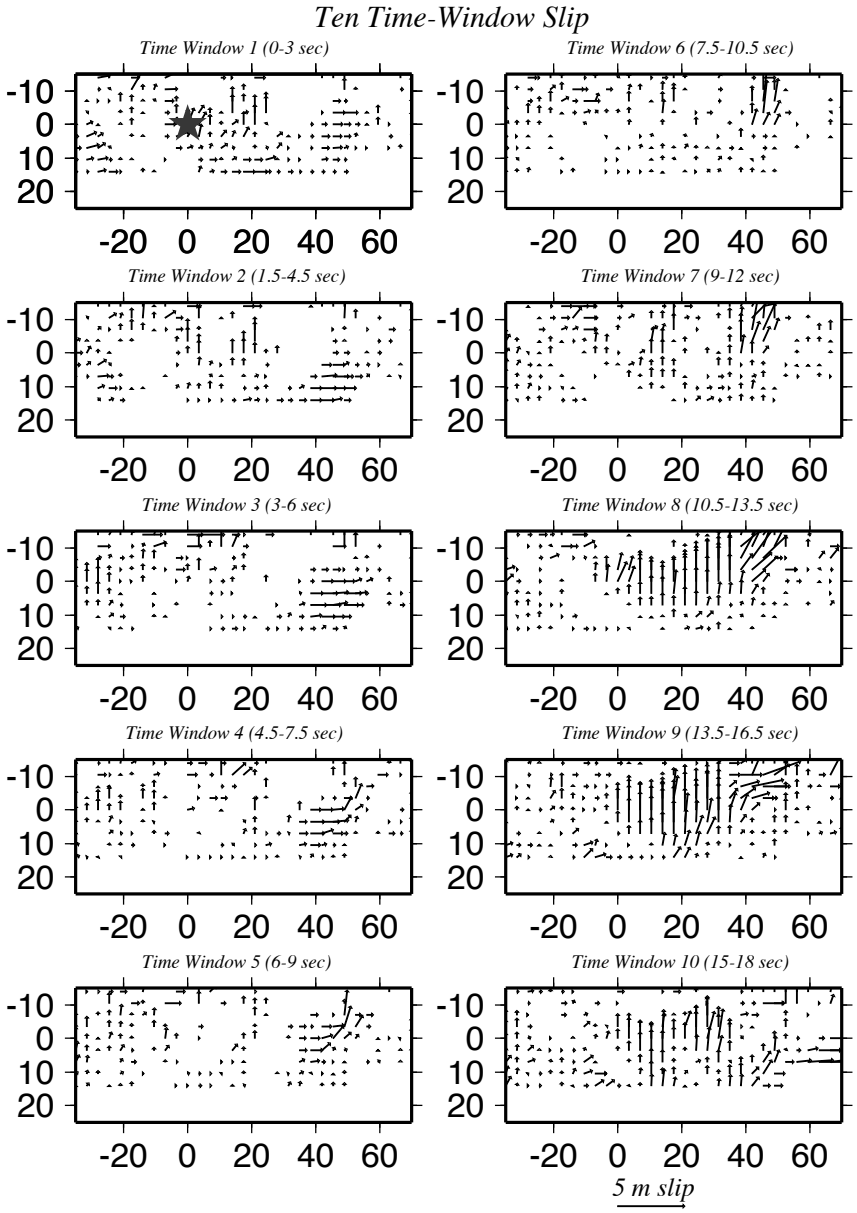
Ten Time-Window Slip
Time Window 1 (0-3 sec)
Time Window 6 (7.5-10.5 sec)
Time Window 2 (1.5-4.5 sec)
Time Window 7 (9-12 sec)
Time Window 3 (3-6 sec)
Time Window 8 (10.5-13.5 sec)
Time Window 4 (4.5-7.5 sec)
Time Window 9 (13.5-16.5 sec)
Time Window 5 (6-9 sec)
Time Window 10 (15-18 sec)
-10
0
10
20
-20
0
20
40
60
5 m slip

Figure 3.10. Dislocation rise time functions from the four fault locations labeled on Figure 3.3. Most of the subfaults showed a delay of about 9 sec before the main rupture occurred, with the exception of the hypocenter, where there are two pulses (D). The particle velocity varies at different locations. Overall, asperity A has a lower particle velocity (< 1.2 m/sec) while asperity B has a higher particle velocity (greater than 2 m/sec).

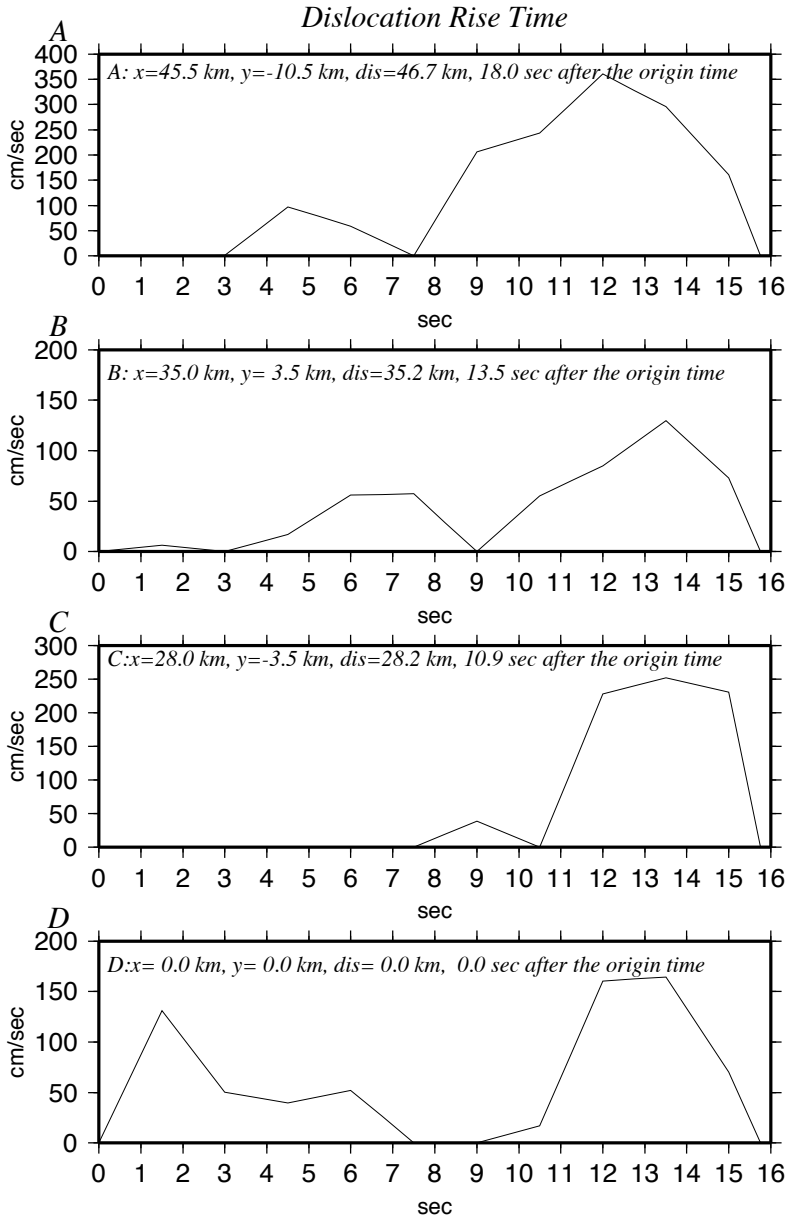
Dislocation Rise Time
A
A: x=45.5 km, y=-10.5 km, dis=46.7 km, 18.0 sec after the origin time
cm/sec
sec
B
B: x=35.0 km, y= 3.5 km, dis=35.2 km, 13.5 sec after the origin time
cm/sec
sec
C
C:x=28.0 km, y=-3.5 km, dis=28.2 km, 10.9 sec after the origin time
cm/sec
sec
D
D:x= 0.0 km, y= 0.0 km, dis= 0.0 km, 0.0 sec after the origin time
cm/sec
sec

Figure 3.11. (A). Average moment rate function showing that the major moment was released over a period of 30 sec and peaked between 19 and 25 sec after the origin time. The rupture duration for each subfault (B) was calculated as the time span in which a subfault has continuous slip greater than 50 cm. The rupture time (C) calculated from the first time window that has greater than 50 cm slip. The delay for that particular time window from the origin time was added to the time it took for the waveform front to reach the subfault with a velocity of 2.6 km/sec. This showed a retardation of rupture when the rupture reached Asperity B and the belt between Puli and Chusan. The rupture front is also seen to slow at shallow depth.

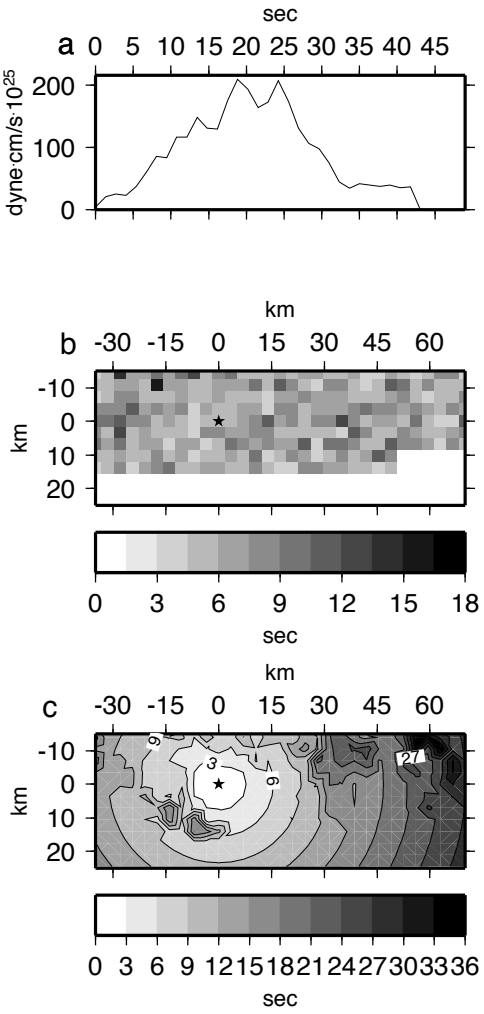
a
sec
0 5 10 15 20 25 30 35 40 45
dyne·cm/s·10^25
200
100
0
b
km
-30 -15 0 15 30 45 60
-10
0
10
20
km
0 3 6 9 12 15 18
sec
c
km
-30 -15 0 15 30 45 60
-10
0
10
20
km
3
6
9
27
0 3 6 9 12 15 18 21 24 27 30 33 36
sec

Table 3.1

1D velocity model used for Green's function calculation

Thickness (km)	*Depth (km)*	*Vp (km/s)*	*Vs (km/s)*	*Density (g/cm^3)*	*Qp*	*Qs*
2.2	2.2	4.5	2.6	1.8	200	100
2.2	4.4	4.85	2.8	2.05	600	300
2.2	6.6	5.3	3.06	2.25	600	300
2.2	8.8	5.6	3.23	2.39	600	300
4.5	13.3	5.84	3.37	2.5	600	300
4.5	17.8	6.13	3.54	2.64	600	300
7.5	25.3	6.28	3.63	2.7	600	300
8.5	33.8	6.6	3.81	2.85	600	300
5	38.3	6.87	3.97	2.97	600	300
21.5	60.3	7.43	4.29	3.3	600	300
25	85.3	7.8	4.5	3.3	600	300

Chapter 4

Finite Fault Inversion of the September 25, 1999 (Mw=6.4) Taiwan Earthquake: Implications for GPS displacements of Chi-Chi, Taiwan Earthquake Sequence

4.1 Abstract.

The September 25, 1999 Chi-Chi Taiwan aftershock (Mw=6.4) occurred on a down dip extension of the fault that ruptured in the mainshock. Strong motion data were used to invert for the finite-source process and test for the causative fault plane. We performed a grid-search over a range of focal mechanisms and found a preferred model (strike=5^o, dip=30^o, slip=100^o) different from teleseismic studies (strike=28 ± 10^o, dip=$27\pm5\ ^o$, slip=106 ± 9^o) but similar to the mainshock (strike=5^o, dip=34^o, slip=65^o). The aftershock asperity has a dimension of 10 km by 10 km with a maximum slip of ~ 1.8 m and a static stress drop of 8 MPa. We forward-predict the GPS displacements and found up to 0.033 m of surface horizontal displacements at some GPS sites, indicating that studies of post-seismic deformation may need to account for the effects of large aftershocks.

4.2 Introduction

Taiwan is one of the most seismically active regions in the world. Several geodynamic models have been proposed to explain the mountain-building process in this region. Among them, Willett (1999) has proposed that the mountain region of Taiwan is underlain by a major shallow-dipping, west-vergent detachment to the west and a steeper east-vergent backthrust to the east. Strong linear seismicity in the vicinity of the proposed detachment has been observed (Kao and Chen, 2000). However, the pattern of seismicity to the east is diffuse and difficult to interpret.

The 1999, Chi-Chi, Taiwan earthquake (Mw=7.6) earthquake caused an 80-km-long surface rupture on a west-vergent thrust (Figure 4.1). Chi et al (2001) found that slip mainly occurred within a triangular zone bounded by the towns of Sanyi, Puli, and Chusan, and inferred that fault segmentation controlled the distribution of slip. More than six Mw=6 and greater aftershocks were recorded by a very dense strong motion network (Lee et al., 1999). Here we use these data to study the finite source rupture process for one of the largest aftershocks (23.86N, 121.01E) that occurred on 25 September, 1999 at 23:52:49.5 UTC.

This event was recorded by more than 200 stations, and provides a unique opportunity to study the fault geometry and the rupture process at a depth (~15 km) where seismic reflection data are currently unavailable. In particular, we hope to discriminate the causative fault plane from the auxiliary plane. There are 3 scenarios for the ruptured plane: down-dip extension of the mainshock on the detachment, backthrust

above the detachment, and a basement-involved fault below the detachment (Figure 4.1). Although the hypocenter is located in the vicinity of the proposed major shallow east-dipping fault, previous data could not exclude the possibility of a high-angle, west-dipping conjugate fault (backthrust). If true, a backthrust will give us an important constraint on the deep crustal geometry under Taiwan. In addition, recent seismicity studies (e.g. Carena et. al., EOS 82(47), p. 1176, 2001) show a steep, west-dipping fault below the detachment and the aftershock might have occurred on this fault, if the aftershock focal depth is actually deeper than reported. This scenario implies that large seismic strains can be stored in the footwall of the detachment and future geodynamic studies might need to consider a deformable footwall block that can generate Mw > 6 earthquakes. If the rupture was on the proposed detachment, we can delineate its attitude and slip distribution, which can be compared to the mainshock. These results will add to our knowledge about stress interactions between the mainshock and aftershocks, may be used to correct the observed deformation field for aftershock contamination, and help in the study of strong ground motion attenuation by providing source parameters of the large shock.

4.2 Method and Results

We used strong motion data from the Central Weather Bureau of Taiwan (Lee at al., 2001) to invert the representation theorem for finite source parameters by using the method of Hartzell and Heaton (1983). We used a linear least-squares inversion of observed velocity seismograms to compute the spatio-temporal slip distribution. To

improve inversion stability, we have applied the following additional constraints: slip-positivity, Laplacian smoothing, and moment minimization.

To reduce the computational cost for the inversion, we picked 11 out of the 200 stations that have high quality waveforms and provide a good azimuthal coverage. The original 50-sec, 3-component acceleration waveforms were integrated once and filtered between 0.02 and 0.5 Hz before being re-sampled at 10 sps. Compared with the predicted arrival times from the 1D velocity model we used, we were able to pick waveforms that show no clear timing errors. Thus we used the absolute time and did not apply any time shift. We have used a square fault model with 225 subfaults each with a dimension of 1.5 km by 1.5 km. We only allow the fault to slip in one direction (constant rake), due to the relatively smaller magnitude of this event. In this study, we use a single dislocation rise time function of 0.5 sec, consistent with Somerville et al. (1999). The time window is defined as an isosceles triangle. All subfault Green's functions are convolved with this source time history. A frequency-wave number methodology by Chandan Saikia (Saikia, 1994) was used to calculate a set of Green's functions based on a 1D velocity model by Rau and Wu (1995). More detailed information can be found in our previous paper on the mainshock (Chi et. al., 2001).

For near source waveforms, the inversion is very sensitive to the focal mechanism. Therefore, we have performed a grid-search over a range of focal parameters to find the optimal orientation using the variance reduction (VR)[VR= $1-(\sum(\text{synthetics-data})^2/\sum(\text{data})^2)$] measure (Figure 4.2). In total, 1036 inversions were performed. For the east-dipping plane, the ranges we have tested are strike: 0-40°; dip: 10-55°; rake: 85-125°; all with an increment of 5°; for the west-dipping plane, strike:

130-230°; dip: 30-80°; rake: 50-100°; all with an increment of 10°. The strike/dip/rake of 10°/30°/100° has the highest variance reduction of 74%. However, we chose 5°/30°/100° (variance reduction 73%) as our preferred model for its similarity to the proposed mainshock fault plane (5/34/65, Chang et al., 2000). As Figure 4.2 shows this mechanism is allowable given the uncertainty. We then tested a range of rupture velocities and found our preferred rupture velocity to be 2.6 km/s. The waveform fits are good for the first few seconds of the pulses (Figure 4.3). Some higher rupture velocity runs produce a higher variance reduction (Figure 4.2), however, the asperity patterns become less coherent. Smaller subfaults (1 km by 1 km) were also tested and the asperity patterns are similar. The reported focal depth is 15 km and we have tested a range of focal depths with an increment of 1 km and found that depths between 11 and 17 km all give similar waveform fits (VR greater than 70%) but the fits deteriorate rapidly outside this depth range. We have also tested the rupture velocity on focal mechanisms derived from teleseismic data (Figure 4.2) and found our preferred model generally gives 10% better variance reduction.

All of the inversions strongly suggest that the rupture occurred on the shallow east-dipping detachment. The variance reduction for the east-dipping fault is typically 25 % higher than the conjugate, steep, west-dipping fault (Figure 4.2). The rupture propagates to the southwest and updip occurring within an area of 10 km by 10 km. The maximum slip is ~180 cm and the moment release is 3.59e+18 N-m (Mw=6.4). The static stress drop of the primary asperity ranges from 2.2 to 8 MPa, if we use 0 and 0.3 m as the threshold for selecting the "ruptured" subfaults, respectively.

4.3 Interpretation and Conclusion:

One surprising outcome from this study is that the strike of our preferred focal mechanism (5°) is different from that of teleseismic results (28°). An initial teleseismic moment tensor inversion for the Chi-Chi mainshock also gave a strike of 26, compared with the strike of 5° derived from the mainshock surface rupture, thus this discrepancy could be systematic and relate to complex crustal velocity structures underneath Taiwan. The dip is 30° to the east. And our focal mechanism tests show that the variance reduction will drop 7% if we use a shallower dip of 10°, inferred from the reflection data collected ~10 km to the west (Wang et al., 2002). A focal depth of 15±4 km will put this aftershock on the down dip extension of the mainshock fault plane. However, it is also possible that the aftershock occurred on a steeper, step-down ramp of a detachment.

The aftershock's rupture extends the southern boundary of the mainshock asperity (Figure 4.1), which may be structurally controlled (Chi et al, 2001). For the mainshock, the slip in this region is mainly thrust with a small left-lateral component, constrained by the GPS data. On the other hand, for this aftershock, both the teleseismic and strong motion data indicate a thrust with a small right-lateral component. We have also tested left-lateral oblique slip in our inversion and found 10-20% decreases in variance reduction. The occurrence of this deep aftershock slip lends support for the relatively deep mainshock slip , though it is poorly constrained.

The relatively large moment release from this aftershock indicates that its effects should be incorporated into the ongoing aftershock/afterslip studies. An excellent GPS dataset has been collected in this region (Yu et al., 2001) and provides a unique opportunity to study the afterslip deformation. Depending on when the campaign GPS sites were reoccupied after the mainshock, some GPS signals might have recorded

deformation from aftershocks. Our results might help to recalibrate the coseismic/postseismic GPS data. Here we forward modeled the GPS displacements using our slip model in an elastic half space (c.f. Okada, 1992). For stations near the aftershock epicenter, most of the horizontal surface displacements are about 1/500 of the observed GPS data from the mainshock. The small displacements are due to the greater depth of this aftershock. However, the displacements can still be up to 3.3 cm at some GPS stations, and thus need to be taken into account in afterslip studies.

In conclusion, the Mw=6.4, 1999/09/25 aftershock has a focal mechanism of strike=5°, dip=30°, and rake=100°, based on the strong motion data. It occurred on a shallow, east-dipping fault having a similar attitude as the mainshock fault plane. It is not on a west-dipping backthrust above the detachment nor on a west-dipping fault plane below the detachment. Rather, it images the down dip extension of the mainshock plane or possibly a ramp in a detachment. The rupture velocity is about 2.6 km/s and the slip extended the southern boundary of the asperity from the mainshock. This event has a small right-lateral component, different from the small left-lateral component of the mainshock, suggesting stress redistribution after the mainshock or fault segmentation. We have used our slip model to forward calculate the GPS displacements and found they are relatively small compared with GPS displacements from the mainshock, however, they may be large enough to be important in aftershock/afterslip studies.

4.4 Acknowledgments

We thank Dave Schmidt for his constructive discussions. We also benefited from careful reviews and constructive criticism by Robert Graves and an anonymous reviewer. This research is partially funded by NSF Grant EAR-0105998.

Figure 4.1. (a) Location map. The large star shows the epicenter of the Chi-Chi mainshock and its surface rupture is shown as the thick solid lines. The small star is the epicenter of the 9/25 event from this study. The 11 stations we used to invert the 9/25 event are plotted as triangles. The dense vectors show the 9/25 slip derived from this study. The maximum slip is 1.8 m. The sparse vectors show the mainshock model (Chi et al., 2001), where the maximum slip is ~10 m. (b) A schematic cross section along AA', showing 3 possible 9/25 rupture scenarios as discussed in the text.

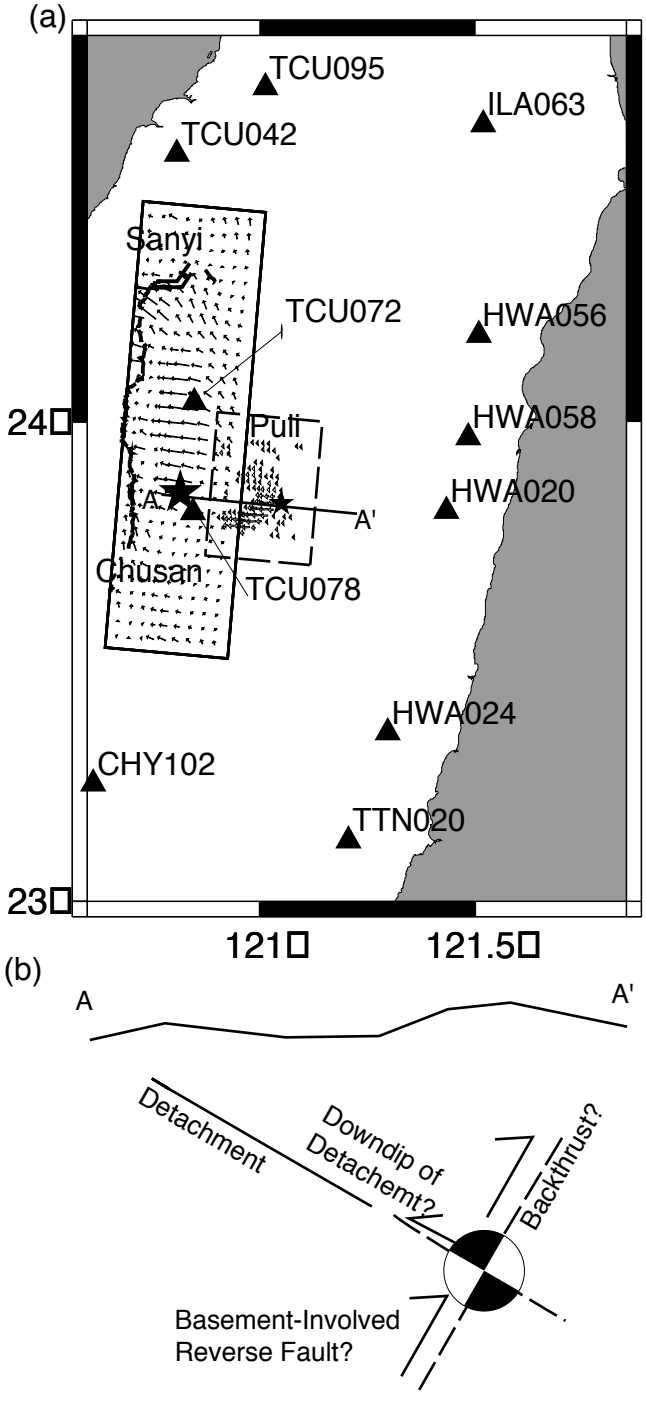
(a)
TCU095
ILA063
TCU042
Sanyi
TCU072
HWA056
24°
Puli
HWA058
A
A'
HWA020
Chusan
TCU078
HWA024
CHY102
TTN020
23°
121°
121.5°
(b)
A
A'
Detachment
Downdip of
Detachemt?
Backthrust?
Basement-Involved
Reverse Fault?

Figure 4.2. (a) Lower hemispheric stereonet plot showing the P axes of the focal mechanisms tested in our inversions. The color scale shows % variance reduction. The circles and the triangles are the east-dipping and west-dipping fault planes, respectively. The star shows the preferred solution (azimuth: 260; plunge: 16). The rectangles show the teleseismic focal mechanisms. The east-dipping planes give 10-20% improvements in variance reduction compared to the conjugate west-dipping planes. (b) Rupture velocity tests using different focal mechanisms. The solid-lines and dashed-lines show the results from east-dipping and west-dipping faults respectively. Overall the east-dipping faults give 10% better variance reduction than the conjugate west-dipping faults. Yellow lines are for the mechanism of Kao and Chen (2000), greens lines for the ERI, University of Tokyo mechanism, and orange lines are for the Harvard CMT mechanism. All of these mechanisms are derived from teleseismic data. The blue line shows the rupture velocity test using our preferred focal mechanism.

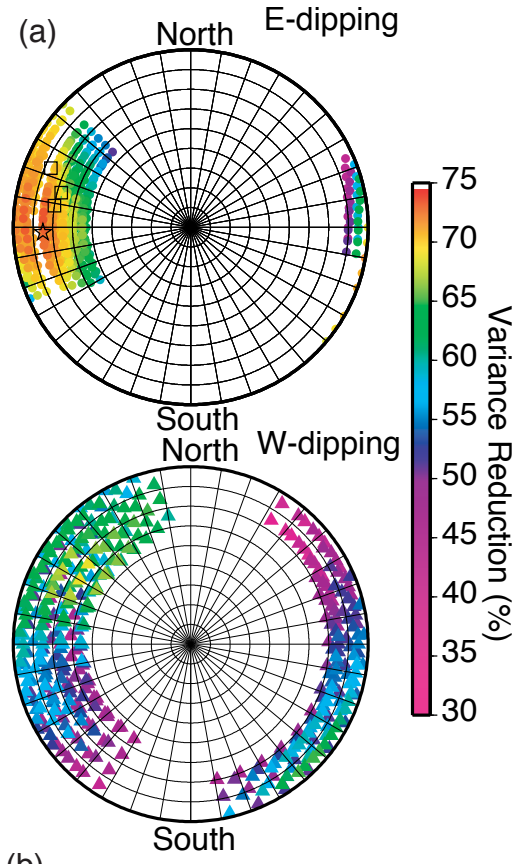

(b)

Rupture Velocity Sensitivity Test
Yellow: KAO (32/32/102; 198/59/83)
Green: ERI (34/25/115; 187/67/79)
Orange: CMT (18/25/102; 185/66/85)
Blue: This Study (5/30/100; 198/59/83)

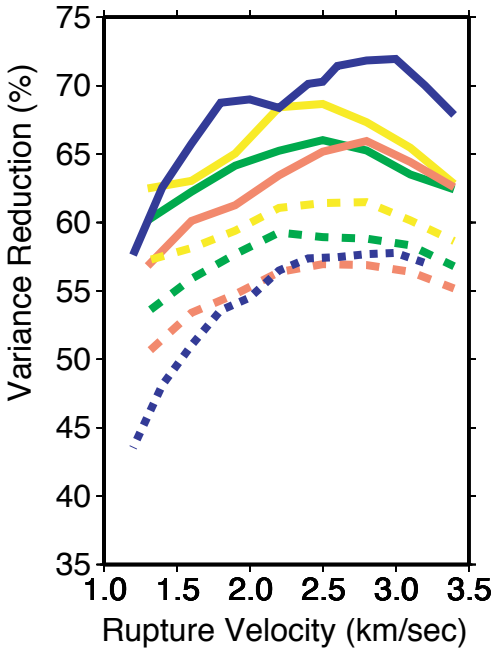

Figure 4.3. Synthetic (red lines) and observed (blue lines) velocity waveforms. The largest amplitude for the observed waveform in mm/s is marked above each waveform. Note the large ground motion at TCU078 compared with that of HWA020.

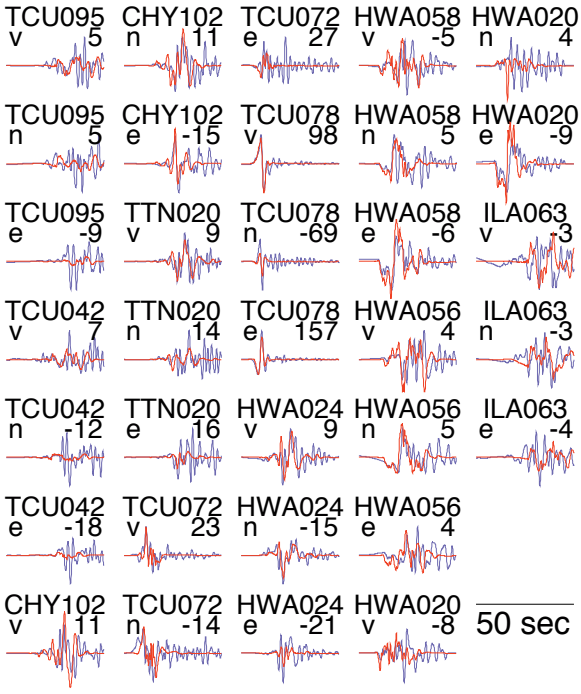
TCU095 v 5
CHY102 n 11
TCU072 e 27
HWA058 v -5
HWA020 n 4
TCU095 n 5
CHY102 e -15
TCU078 v 98
HWA058 n 5
HWA020 e -9
TCU095 e -9
TTN020 v 9
TCU078 n -69
HWA058 e -6
ILA063 v -3
TCU042 v 7
TTN020 n 14
TCU078 e 157
HWA056 v 4
ILA063 n -3
TCU042 n -12
TTN020 e 16
HWA024 v 9
HWA056 n 5
ILA063 e -4
TCU042 e -18
TCU072 v 23
HWA024 n -15
HWA056 e 4
CHY102 v 11
TCU072 n -14
HWA024 e -21
HWA020 v -8
50 sec

Table 4.1: 1D velocity model used for Green's function

Thickness	***Depth***	***Vp***	***Vs***	***Density***	***Qp***	***Qs***
km	***km***	***km/s***	***km/s***	***g/cm^3***		
2.2	**2.2**	**4.5**	**2.6**	**1.8**	**200**	**100**
2.2	**4.4**	**4.85**	**2.8**	**2.05**	**600**	**300**
2.2	**6.6**	**5.3**	**3.06**	**2.25**	**600**	**300**
2.2	**8.8**	**5.6**	**3.23**	**2.39**	**600**	**300**
4.5	**13.3**	**5.84**	**3.37**	**2.5**	**600**	**300**
4.5	**17.8**	**6.13**	**3.54**	**2.64**	**600**	**300**
7.5	**25.3**	**6.28**	**3.63**	**2.7**	**600**	**300**
8.5	**33.8**	**6.6**	**3.81**	**2.85**	**600**	**300**
5	**38.3**	**6.87**	**3.97**	**2.97**	**600**	**300**
21.5	**60.3**	**7.43**	**4.29**	**3.3**	**600**	**300**
25	**85.3**	**7.8**	**4.5**	**3.3**	**600**	**300**

Chapter 5

Seismic Hazard Mitigation and Crustal Deformation: Results from Finite Source Process of Six Mw greater than 5.8 Chi-Chi, Taiwan Aftershocks

5.1 Abstract

We inverted strong motion data for the finite source parameters of 6 large aftershocks of the 1999 Chi-Chi, Taiwan earthquake. For each event, we derived a preferred model by testing different focal mechanisms, hypocenters, rupture velocities, and dislocation rise times, as well as different combinations of stations in more than 1000 inversions. We documented how the fits between the waveforms and the corresponding synthetics deteriorated as the hypocenter and focal mechanism deviate from those of the preferred model. These results will help to determine how accurate these parameters must be if we wish to derive slip models in near real-time for generating shakemaps. If the deviation in focal mechanisms and hypocenters were less than 20^{o} and 5 km, respectively, we generally recovered 80% of the preferred model's synthetic waveform fit. Unlike the dislocation rise time, the rupture velocity used in the inversion had a strong influence on the waveform fits. We also used the slip models to study fault geometry. Two of the aftershocks ruptured on the southern extension of the mainshock

fault plane. One strike-slip aftershock nucleated within the basement but ruptured mainly within the overlying sedimentary strata, suggesting that seismogenic deformation in the basement can influence shallow structures. P-axes of the derived models have azimuths consistent with current plate motion. Finally, GPS displacement derived from the 6 slip models can explain 80% of the post-seismic deformation observed in the aftershock regions, indicating that studies of post-seismic deformation must take into account the cumulative effects of large, shallow aftershocks.

5.2 Introduction

More than 30,000 aftershocks occurred in the three months following the Chi-Chi, Taiwan earthquake (Mw=7.6). Among them, more than 6 aftershocks with Mw>5.8 were well-recorded by a strong motion network maintained by the Central Weather Bureau of Taiwan. They provided an unprecedented opportunity to study the finite source process of moderate sized earthquakes to 1) learn more about the spatial relationships of faults in the region, 2) to compare source parameters of the moderate to large aftershocks with those of the mainshock, and 3) to map the deep crustal structure of Taiwan.

Here we document finite source inversions and sensitivity tests for 6 of the aftershocks (table 5.1) for which strong motion data are available. Each aftershock was recorded by more than 200 strong motion stations. We use only data from stations that had no apparent timing errors and provide good azimuthal coverage (Figure 5.1). Using a preliminary slip model, for each event we tested a range of values for each of the source

parameters: the slip vector, fault orientation, location, hypocentral depth, rupture velocity, and dislocation rise time. In this modeling we assumed that the rupture velocity and dislocation rise time were constant and did not vary spatially. For each event, we performed more than 1000 sensitivity tests by varying the source parameters used in the inversions and we documented the influence these parameters have on the slip model and the waveform fits (table 5.2). To determine what the contributions of individual stations are and whether the results might be biased, we applied "Jackknife tests." That is we examined the fits of the waveforms from the inversions for which we excluded the data from one station at a time until we have tested all the stations in the preferred model. With these tests we were able to derive a preferred slip model that was stable and gave good waveform fits. As none of these aftershocks ruptured the surface, nor had rupture planes unambiguously defined by smaller aftershock seismicity, these inversions were also used to determine the orientation of the causative plane and to provide an estimate of the confidence in the chosen plane.

The Chi-Chi sequence also provides a great opportunity using earthquake sources to map the deep crustal structures of Taiwan. Several seismicity and moment tensor studies have already illuminated the geometry of important seismogenic faults at depth (e.g. Kao and Chen, 2000; Hirata et al., 2000, Carena et al., 2002, Chen et al., 2002). To make the tectonic interpretation easier, we want to connect these data "points" in three dimensions using the planes of the planar slip models derived from the results of our finite fault inversion. The mainshock and aftershock slip models then can also be used to calculate the static stress perturbation during the entire earthquake sequence.

All of these results are important for seismic mitigation. The causative faults derived from this study, all of which are blind, can be added to the map of active faults in Taiwan. The stress perturbation from mainshock and aftershocks can be used to recalibrate the post-seismic regional stress pattern. The slip models are important for studying earthquake source scaling relationships and attenuation relationships for engineering purposes. Also, the extensive sensitivity tests document how variations in the input source parameters affect the waveform fits derived from the finite fault inversions. As a result, these studies provide the criteria needed to evaluate the performance of the seismic network if we want to invert the finite fault parameters in real time and use the source model to forward-model the shakemaps, which can be used by the seismic response authorities for seismic mitigation purposes (e.g. Dreger and Kaverina, 2000).

5.3 Regional Tectonic Setting of Taiwan

Central Taiwan is located in the collision zone between the Luzon arc of Philippine Sea plate and the Chinese passive margin of the Eurasia plate. The relative plate motion is about 80 mm/yr in the N66^{o}W direction (Yu et al., 2001). Here the Chinese continental passive margin, with normal and strike-slip fault structures, enters into the convergent boundary where contractional processes dominate. Suppe et al. (1981) have proposed that most of the sediments above the basement are being

incorporated into the Taiwan fold and thrust belt by westward propagation of a low angle east-dipping decollement fault, beneath the mountain belt. However, the shortening style below the decollement is less understood. The basement may act as a relatively rigid body underthrusting the mountain belt (Suppe, 1981; Suppe, 1984) or it may deform internally to thicken the crust in Taiwan (Rau and Wu, 1995).

5.4 Chi-Chi, Taiwan, Earthquake and Its Aftershocks

Seismicity and moment tensor studies of the Chi-Chi earthquake sequence have already provided important constraints on the crustal geometry. Kao and Chen (2000) proposed that the aftershocks occurred on two parallel, low-angle east-dipping faults, one in the vicinity of the proposed decollement and a second 15 km below it (Figure 5.1b, inset). The decollement is also illuminated in an aftershock study by Hirata et al. (2000), although with a shallower dip. Carena et al. (2002) suggested a low-angle east-dipping detachment under most of central and eastern Taiwan, with a separate seismicity zone underneath the detachment dipping to the west. Chen et al. (2002) present evidence for this west-dipping seismic zone based on their relocations of events and the focal mechanisms they determine (c.f. the basement-involved west-dipping fault in Figure 5.1b). Overall, the aftershocks are well-located. However, the uncertainties in focal depths and the ambiguity in determining the causative fault planes from moment tensor or first-motion solutions have prompted different interpretations of the fault geometry. In addition, some of the large aftershocks in the vicinity of the decollement consistently have one nodal plane dipping 30^{o} to 40^{o} to the east (e.g. Kao and Chen, 2000), which is

steeper than the proposed shallowly dipping decollement. As a result, these aftershocks could have ruptured either on the shallowly east-dipping decollement, on the west-dipping backthrusts above the decollement, on the steeper east-dipping splay faults above the decollement, or even on steep west-dipping basement-involved reverse faults under the decollement (Figure 5.1b).

The finite-source process of the mainshock has been studied extensively using various combinations of strong motion, teleseismic, and GPS data (e.g. Yagi and Kikuchi, 2000; Kikuchi et al., 2000, 1999; Ma et al., 2000; Ma et al, 2001; Zeng and Chen, 2001, Mori et al., 2000; Ji et al., 2002; Wu et al., 2001; Chi et al., 2001; Lovenbruck et al., 2001). To a first order, the source models are all consistent, showing large slip to the north of the focus at shallow depths. Slip to the south tends to be less constrained. There is evidence that the extent of mainshock rupture may have been structurally controlled and Chi et al. (2001) suggest that the mainshock asperity terminated in the south along a lineation between the towns of Puli and Chusan (Figure 5.1).

Excellent GPS displacement data have been collected for the pre-event, coseismic, and postseismic epochs (Yu et al., 2001). More than 10 m of horizontal co-seismic displacement was found in the northern region of the surface rupture. There are also greater than 10 cm of displacement recorded 3 months after the mainshock, mostly in the southern section of the surface rupture (Hsu et al., 2001), where the large aftershocks occurred.

5.5 Strong Motion Data and Method

In this study we use strong motion data collected by the Central Weather Bureau (CWB) of Taiwan (Lee et al., 1999; Lee et al., 2001) and supplement it with data from the Institute of Earth Sciences (IES), Academia Sinica of Taiwan. Overall, more than 200 accelerometers with sample rates of either 200 or 250 sps, recorded each of the six large aftershocks. We have converted each waveform from digital counts to cm/s^2, removed the mean offset, integrated from acceleration to velocity, and bandpass filtered between 0.02 and 0.5 Hz with a four-pole acausal Butterworth filter before resampling the data to 10 sps.

Using a frequency-wave number code from Chandan Saikia (Saikia, 1994), we calculated a catalog of Green's functions for an average 1D velocity model (table 5.3) taken from a 3D tomographic study by Rau and Wu (1995). This 1D model had been tested in routine regional moment tensor studies of local and regional events (c.f. Kao and Chen, 2000) and performed well for the finite fault inversion of Chi-Chi mainshock (Chi et al., 2001). The Green's functions were subjected to the same signal processing.

We used strong motion data to invert the representation theorem, equation 1 (Aki and Richards, 1980), for parameters of the finite source using a method pioneered by Hartzell and Heaton (1983). The seismograms are used to calculate the spatio-temporal integration of slip distribution on a plane where,

$$u_n(x,t) = \int_{-\infty}^{\infty} d\tau \iint_{\Sigma} \left[u_i(\xi,\tau) \right] c_{ijpq} v_j \partial G_{np}\left(x, t-\tau, \xi, 0\right) / \partial \xi_q d\Sigma \qquad (1)$$

u_n nth component of observed velocity

c_{ijpq} fourth-order elasticity tensor

v_j fault orientation unit vector

G_{np} Green's function

x vector describing the relative location of the source and receiver

ξ, τ spatial and temporal variables of integration

In the equation, n refers to the ground motion component and i, j, p, and q are orientation indices. The quantity $u_i(\xi, \tau)c_{ijpq}v_j$ is equivalent to $m(\xi,\tau)$, the seismic moment tensor which changes in space and time. $u_i(\xi, \tau)$ is the spatio-temporal slip information to be determined by inverting the data.

We use a damped, linear least-squares inversion to determine the spatio-temporally discretized slip. For each grid point (subfault) on the gridded fault plane, we calculate the slip amplitude using a prescribed slip vector direction. We use a single time-window with a fixed dislocation rise time propagating away from the hypocenter with a spatially constant rupture velocity, due to the relatively small magnitude of the aftershocks compared with the mainshock. The absolute times of the waveforms were

used to align the data with the Green's functions in time. Laplacian smoothing and moment minimization constraints, as well as slip positivity, implemented using the non-negative least squares inversion of Lawson and Hanson (1974), are used as constraints to improve the stability of the inversions.

A range of values for the following source parameters (table 5.2) have been tested to see their effects on the inverted synthetics and to improve the waveform fits: hypocentral locations, rupture velocity, dislocation rise time, focal mechanism on both conjugate fault planes. By doing this we were able to identify which parameters have stronger influence on the inversions.

Due to the vast amount of strong motion data, and the uncertainty about the accuracy of the timing at some stations, we expended a great deal of effort to find the optimal station configuration. The waveform fits for the initial inversions are usually not good, especially if some seismograms have apparent timing errors or large amplitude phases due to crustal 3D velocity heterogeneity. The waveform fits also degraded if the source parameters used in the inversions were not close to those of the preferred model. To avoid timing problems, we picked stations with arrival times similar to the arrival time predicted by our 1D velocity model, as was done in Chi et al. (2001). Horizontal particle motion for each station was plotted in map view to help identify and avoid stations with abnormally large particle motion compared with neighboring stations (Figure 5.2). To characterize the ground motion in urban regions during the aftershocks, we also used these particle motion plots to document horizontal peak ground velocity

(HPGV) direction and the aspect ratio between the short and long axes (Figure 5.2). For each aftershock, we have tested all of the available moment tensor solutions, some of which have very different focal mechanisms and source depths. Using the reported moment magnitude, we parameterized the fault dimensions, and dislocation rise times using the relationships published by Sommerville et al. (1999). If necessary, we adjusted the fault dimensions for each individual aftershock. In some cases the dimension of the fault model was too small, so the slip terminated at the edge. We then had to increase the fault dimension. In other cases, when the initial dimensions of the fault were too large, some energy from later parts of the waveforms were mapped into the slip model, even though they might have been scattered wave fields and not related to the earthquake source. We then reduced the size of the fault.

Once we had an initial model with an optimal configuration of stations, we did a grid-search over a range of source parameters, including the direction of the slip vector, the fault orientation, the hypocentral location, the rupture velocity, and the dislocation rise time (table 5.2). We varied these source parameters one at a time, running the inversion using the new input parameter, and then studied the changes in slip model and waveform fits. Thus we were able to document the sensitivity of the synthetics and their fits to the waveforms to each of these parameters before selecting the preferred model. In doing so, we were able to improve the waveform fits and estimate the uncertainty in each of the preferred source parameters. For this purpose we define the error bounds as 10% of the variance reduction (VR)[VR= $1- (\sum(\text{synthetics-data})^2/\sum(\text{data})^2)$] from the preferred model. To test the contribution of some individual seismic stations to the

preferred model, we then excluded these stations and reran the inversions to document the change in the slip models and waveform fits. For each event, we did more than 1000 tests; each taking 10-20 minutes on a typical SUN workstation. We then assigned confidence levels for the preferred slip model based on waveform fits and by comparing the results with other geologic and geophysical data. While these sensitivity tests only covered a small portion of the total parameter space, this study represents the most thorough attempt to document such uncertainties in finite source inversions.

5.6 Finite Fault Inversion For Event 1 (09201757)

Event 1 occurred on 20 September 1999, 17:57:15.31 UTC, and was located at 121.01^{o}E, 23.94^{o}N at a depth of 8 km (Figure 5.1b). Its strike, dip, and rake are 200^{o}, 41^{o}, and 78^{o}, respectively. The moment and Mw are 7.15 x 10^{24} dyne-cm and 5.8, respectively. We have low confidence in the preferred model (Figure 5.3) for this event, which occurred 10 minutes after the mainshock at a time when many other aftershocks were occurring. Horizontal peak ground velocity (HPGV) at some stations is polarized E-W but most of the other stations do not have a consistent HPGV direction. A M_L=4.61 event occurred 23 km away and 1 sec before this event, thereby complicating the preliminary estimation of hypocentral parameters (Gensin Chang, personal communication, 2002), and thus the finite fault inversion. Sensitivity tests show that the 12 km by 4 km rupture patch is located near 121.04^{o}E, 23.97^{o}N. Its depths range from 6 to 8 km, shallower than the proposed decollement. Our slip model has a maximum slip of 46 cm while the static stress drop is 5.3 MPa. The variance reduction (VR) of the derived

preferred model determined using data from thirteen 3-component stations is 46%, slightly less than the VR of 48% for the east-dipping conjugate fault. We favor the west-dipping fault plane because it correlates well with the locations of the aftershocks (Figure 5.3). To identify stations that will help determine the causative fault plane, we forward-predicted ground motions using both conjugate fault slip models and found that both models can fit most of the near source stations relatively well, partly because three near source stations were used in the inversion to constrain the models. However, the two conjugate slip models produced very different synthetics east of the hypocenter in the mountainous regions where strong motion data are not currently available. Thus, good station coverage in the mountainous region above the decollement will be important for future finite source studies.

Using a 10% decrease in VR as the error threshold, we found that a location error less then 4 km still gave a good fit to the waveforms (Figure 1b). Within 20^o of error in focal mechanism is also acceptable, as shown in Figure 5.4. Possible focal depths range from 6 to 13 km, and rupture velocities from 1.3 to 2.6 km/s (Figure 5.5). Waveform fits are not very sensitive to dislocation rise time. Table 5.1 lists details of the source parameters and slip models of each of the events.

5.7 Finite Fault Inversion For Event 2 (09201803)

Event 2 occurred on 20 September 1999, 18:03:41.16 UTC and was located at 120.86^oE, 23.81^oN at a depth of 8 km (Figure 5.1b). The strike, dip, rake are 0^o, 10^o, and

80^o respectively. The moment and Mw are 2.53 x 10^{25} dyne-cm and 6.2, respectively. We assign a high level of confidence to the preferred model (Figure 5.6) for this event and the VR from the inversion of data of thirteen 3-component stations is 56%. The preferred model is strongly controlled by station TCU079 because the VR of the inversion removing this station from the optimal station configuration drops to 50%. The mapview plot of particle-motion shows a clear westward thrust radiation pattern. The back-azimuth direction is mostly sub-parallel to the HPGV direction. As a result, there is generally more E-W ground motion on the western coastal plains, which are densely populated. The particle motion shows an aspect ratio of 1:2 between the short and long axes. Some secondary phases, recorded 20 seconds after the origin time (i.e. at stations TCU078, TCU079, TCU089), could not be modeled in our inversions. These late arrivals do not contribute to the preferred slip model. The 10 km by 10 km slip patch is located near 120.82^{o}E and 23.79^{o}N at a depth of 6 to 8 km. Maximum slip is 231 cm and the static stress drop is 6.2 MPa. This aftershock ruptured along the southern end of mainshock asperity along the Puli-Chusan lineation proposed by Chi et al. (2001). In the cross section view, our slip model coincides with the shallowly east-dipping fault imaged by a recent reflection profile from Wang et al. (2002). Because the dip angle is very shallow, we suspect that there may be trade-offs between strike and rake. For example, a slip model with a strike and rake of 350^o and 80^o will be similar to that of 20^o and 110^o because the slip at each subfault of both models will have similar azimuths and the latitude and longitude. The low slip near the hypocenter (Figure 5.6) may be an artifact resulting from an incorrect origin time. However, we tested this by adding a delay of less than 1 sec to the reported origin time. While the slip became more concentrated near the

hypocenter, waveform fits were degraded. To be consistent with other events in this study, we continued to use the reported origin time. Sensitivity tests of focal depth, rupture velocity, and dislocation rise time have patterns similar to that of Event 1.

5.8 Finite Fault Inversion For Event 3 (09202146)

Event 3 occurred on 20 September 1999, 21:46:37.49 UTC at 120.82^{o}E, 23.60^{o}N at a focal depth of 18 km (Figure 5.1b). The strike, dip, and rake are 330^{o}, 89^{o}, and 15^{o}, respectively. The moment and Mw are 2.2 x 10^{25} dyne-cm and 6.2, respectively. We assign a high level of confidence to the preferred model for this event, which has a VR of 56% from the inversion of nine 3-component stations. Unlike the other thrust-type aftershocks, this strike-slip event has N-S oriented HPGV direction in the coastal plain, perpendicular to the back azimuth direction and consistent with a strike-slip radiation pattern for the S wave. The aspect ratio for the horizontal particle motion plot is about 1:3 to 1:4 at most stations. The 5 km by 25 km slip patch on a vertical plane mainly ruptured in sedimentary units at depths similar to that of the Event 2 slip patch. The maximum slip is 85 cm (Figure 5.7), and the static stress drop is 3.8 MPa, the lowest among the aftershocks we studied. Location tests show that hypocenters within an elongated region along the strike of the fault gave good waveform fits (Figure 5.1b). The preferred rake is similar to the dip of the decollement to the north, consistent with the kinematics north of this strike-slip fault. A depth of 18 km places the hypocenter in the basement.

We have studied the relationship between waveform fits and the hypocentral depth assigned in the inversions. For this event, the variance reduction decreased 10% when we used a hypocentral depth of shallower than10 km (Figure 5.5). In particular, the inversions with shallow hypocenters could not generate the large amplitude particle motion observed at stations CHY080 and CHY035. Our slip model is strongly controlled by station CHY080. When it is omitted from the inversion, the VR actually decreases by 12%. The amount of slip in the basement depends slightly on the level of smoothing and on moment minimization constraints, but the overall "belt-shaped" slip patterns in the basement are similar. The fault slip is near two of Taiwan's highest mountains, and the waveforms could be complicated due to scattering of the wavefield from the rough topography. This event occurred on a fault not previously mapped. However, this NW-EW striking fault is parallel to and located between two other faults shown on the geologic map (Central Geological Survey, 2000), which, like this slip model, are bounded at both ends by NE-SW trending faults.

5.9 Finite Fault Inversion For Event 4 (09220014)

Event 4 occurred on 22 September 1999, 00:14:40.77 UTC at 120.08^{o}E, 23.81^{o}N at a depth of 10 km (Figure 5.1b). The strike, dip, and rake are 165^{o}, 70^{o}, and 100^{o}, respectively. The moment and Mw are 2.5 x 10^{25} dyne-cm and 6.2, respectively. We assigned a low confidence level to the preferred model for this event. The VR for data from nine 3-component stations is 48% (Figure 5.8). Station configuration tests show that the slip model is not dominated by any one station. Its HPGV direction is mainly

EW in the western coastal plain. Most of the horizontal particle motion has an aspect ratio of 1:4. In contrast to most of the other aftershocks, some stations on the east coast of Taiwan recorded amplitudes larger than those of western stations at similar epicentral distances. A wide range of focal mechanisms have been reported for this event (table 5.1) and reported epicentral depths range from 12.4 to 29 km (Chen et al., 2002; ERI website; Harvard CMT; Kao and Angelier, 2001). Sensitivity tests show that the 6 km by 20 km slip patch is located near 121.04^{o}E, 23.85^{o}N with depths ranging from 13 to 24 km. This aftershock ruptured downdip into the basement. Our slip model has a maximum slip of 83 cm and a static stress drop of 4.6 MPa (Figure 5.8). It was difficult to interpret which of the conjugate fault planes ruptured due to the uncertainty in the focal depth of this event. The preferred models for both of the conjugate faults give VRs greater than 40%. But they favor different focal depths and rupture velocities (Figure 5.5). If the focus is deep and the rupture velocity very slow, it is possible to fit the waveforms well with the east-dipping fault. However smaller aftershocks correlate better with the deep west-dipping fault, not the east-dipping fault above the decollement. Our result is more consistent with the west-dipping seismicity below the decollement observed by Carena et al. (2002), and Chen et al. (2002). The strike of this slip model shows 30 degrees difference from that of seismicity from Carena et al. (2002) but is consistent with the focal mechanism of Chen et al. (2002).

5.10 Finite Fault Inversion For Event 5 (09252352)

Event 5 occurred on 25 September 1999, 23:52:49.51 UTC at 121.01^{o}E, 23.87^{o}N at a depth of 16 km (Figure 5.1). Its strike, dip, and rake, 5^{o}, 30^{o}, and 100^{o}, respectively, are very similar to those of the mainshock. The moment and Mw are 3.7 x 10^{25} dyne-cm and 6.3, respectively. We have high confidence in the preferred solution for this event because the VR from the inversion of data from eleven 3-component stations is 72% (Figure 5.9). The slip model is strongly controlled by station TCU078. Chi and Dreger (2002) published preliminary finite fault inversion results for this event. Here, we have performed additional sensitivity tests and included them for completeness. The HPGV direction is mainly E-W in the western coastal region, and the particle motion aspect ratio is mostly 1:4. Waveforms recorded southwest of the epicenter had large amplitudes. The 6 km by 22 km slip patch is near 121.00^{o}E, 23.81^{o}N with depths from 12 to 18 km. Our slip model has a 162 cm maximum slip and a static stress drop of 5.9 MPa (Figure 5.9). In map view and in cross section this event appears to be a down-dip extension of Event 2, although the dips of the two events are slightly different. Due to the uncertainty in depth and the steeper dip angle, this event may have been on a step down of the decollement or a splay fault above it. Both events ruptured along the Puli-Chusan Lineation and are sandwiched between aftershock seismicity to the south and mainshock rupture to the north.

5.11 Finite Fault Inversion For Event 6 (10220218)

Event 6 occurred on 22 October 1999, 02:18:56.93 UTC at 120.45^{o}E, 23.53^{o}N at a depth of 16 km (Figure 5.1b). It caused at least 12 buildings to collapse near the city of

Chai-Yi. The strike, dip, and rake are 20^o, 75^o, and 90^o, respectively. The moment and Mw are 1.7 x 10^{25} dyne-cm and 6.1, respectively. The VR is 60% from the inversions of data from fourteen 3-component stations. Because fits from both conjugate faults were equally good, we assigned a low level of confidence to the preferred model for this event. More than 30 strong motion stations at epicentral distance less than 25 km recorded this event, and at all azimuths.

The near source waveforms may have been complicated by 3D basin structures, which may explain the wide range of MT solutions and differences of up to 5 seconds in origin time reported by different agencies (table 5.1). Overall the HPGV direction is WNW-ESE east and west of the hypocenter and N-S for stations south of hypocenter. In a preliminary finite fault inversion using data from 6 strong motion stations, the west-dipping fault produced better variance reduction. By adding 8 additional stations in the course of station configuration tests, we found that the variance reduction of the west-dipping plane is slightly higher if the focal depth is about 8 km. However, the east-dipping plane also produced good waveform fits if we used a focal depth of 16 km (Figure 5.10). We picked the east-dipping fault plane as the preferred model only because the focal depths reported for this event are consistently around 16 km and regional geologic interpretation favors east-dipping faults.

5.12 Sensitivity of the Inversions to the Station Used and to Changes in the Source Parameters

Because more than 200 stations recorded each aftershock, the most challenging part of this study was to find the configuration of stations which gave good azimuthal coverage and enough waveforms with paths that could be represented by the simple 1D crustal model we used to calculate the Green's functions. Many of the strong motion stations may have timing problems (Lee et al., 2001) and may be affected by the 3D heterogeneity of velocity structures along the path. If we randomly selected 20-40 stations with good azimuthal coverage and inverted them, the resulting scalar moments were small and the variance reduction low. For this particular study, we chose to use between 9 and 14 stations. We picked the stations by trial and error and by eliminating stations with abnormal waveforms compared to neighboring stations. In particular, we chose stations based on their performance in initial inversions using preliminary source parameters derived from those reported by various agencies, thus the selection of stations may be biased if the reported source parameters are incorrect. To make our analysis more robust, we made a concerted effort to test any newly reported source parameters as they became available.

The focal mechanism is one of the most important source parameters in our inversion. We did a grid search on the focal mechanism parameters and found that, overall the waveform fits are strongly controlled by the dip angle. A deviation of 20^{o} will decrease the VR by 10% (Figure 5.4), e.g. VR will decrease from 50% to 40%. However, the single strike-slip event among these aftershocks is more sensitive to strike and rake than the thrust events. This may be related to the fact that the maximum amplitude of the shear wave radiation patterns coincides with the fault planes. As a

result, the large amplitude waveforms are up-dip of the thrust and along a strike-slip fault, and are sensitive to the dip of the thrust or the strike of the strike-slip fault, provided the hypocenter is fixed. For strike-slip faults, this poses only a small problem because their causative faults can usually be identified easily by aftershock distributions, which usually have epicentral locations that are more accurate than their depths. However, for blind thrusts, it is possible that discrepancies in the dip of preliminary focal mechanisms maybe up to 20^{o} and this could cause problems for routine finite source inversions that rely on an a priori knowledge of the fault orientation.

Good hypocentral information is also very important. We found that the epicentral location has a large influence on the waveform fits (Figure 5.1b). When we shifted the hypocenter by 5 km from the optimal hypocenter, the VR of the synthetics decreased about 10%. Except for Event 4, we also found that an error of 5 km in focal depth will reduce the VR by 10%. For comparison, the asperities we derived from this study have dimensions ranging from 5 km by 10 km to 6 km by 22 km. So the error bounds are roughly similar to the small dimension of the slip distribution.

More accurate focal depths would be helpful in cases where we not only want good waveform fits, but also want to determine the causative fault for thrust events such as these with Mw ranging from 5.8 to 6.3. Overall, the inversion will place the slip at a location and at an elapsed time from origin time (Figure 5.11). For updip or downdip ruptures this means that, for a fixed hypocentral location, one hypocenter will be shallower than the slip depth while the conjugate fault scenario will have a hypocenter

deeper than the slip depth. Provided that the Green's functions and the inversions have placed the slip patch at the correct location and depth, an accurately reported hypocentral depth will help determine which fault plane has ruptured. The locations of smaller events, aftershocks of the large aftershocks, can also help to constrain the causative plane.

From sensitivity tests we found that the optimal rupture velocity depends on the dip angle of the fault plane, and on the relative location of the hypocenter and major slip (Figure 5.11). Again we must assume that the origin time of the event and the Green's functions are correct. Then the inversion will place the slip at a specific location and at a specific time. To get good waveform fits, the optimal rupture velocity must be the ratio between the distance from the hypocenter to the slip (rupture distance) and the lapse time. For a fixed hypocentral location, the more steeply dipping fault of the two conjugate planes will have a longer rupture distance, and thus a higher optimal rupture velocity. This analysis suggests that the rupture velocity may help to further constrain the causative fault plane. Using Event 4 as an example, we found the slip model on a 70^{o} west-dipping fault plane gave a reasonable rupture velocity while the 20^{o} east-dipping fault plane gave a very low rupture velocity. This result is consistent with the interpretation that this event ruptured on the west-dipping fault.

Compared to the tests of focal mechanisms and hypocentral locations, we found that the inversions are not very sensitive to changes in the dislocation rise time. This is, in part, due to the relatively small size of the events and the low pass filter-corner applied

to the data and Green's functions. Empirical relationships indicate that the average rise times for such events should be short, at or below limit of resolution of our tests.

5.13 Implications for Seismic Hazard Mitigation

Recently there has been a push within the seismological community to produce maps of ground shaking intensity in near real time for emergency response purposes (e.g. Wald et al., 1999). In densely instrumented regions, such as Southern California, Japan, and Taiwan, these maps can be generated using ground-truth measurements. However, other approaches are needed for regions with sparse station coverage, including an approach to derive finite source parameters in near real time, then forward model the ground shaking in the regions of interest (e.g. Dreger and Kaverina (2000)). An initial set of good source parameters will dramatically reduce the time required to derive a slip model and enable us to generate synthetic ground shaking information in a timely fashion. It is also beneficial to have correct finite source information soon after the earthquake. The information then can help to identify the causative fault plane, design temporary portable seismic networks to monitor the aftershocks surrounding the main event, and forward calculate the stress perturbation due to the earthquake.

We found that it is important to identify several good stations, which can be used for initial finite source inversions. Using all of the available stations can sometimes overwhelm the inversion, and useful information in the waveforms may be suppressed due to timing problems and site effects.

To successfully predict ground motion we need to have good waveform fits at all azimuths from the hypocenter. From our sensitivity tests on Mw=5.8-6.3 earthquakes we found that this can be easily achieved if the hypocenter mislocation is less than 5 km and if the focal mechanisms are accurate to within 20^{o}. Such epicentral accuracies are found, for example, within the error estimates from 90% of the 1590 earthquakes (1998-2002) in the Northern California Earthquake Data Center Hypoinv2000 Catalog available at http://quake.geo.berkeley.edu/ncedc/catalog-search.html. Damaging earthquakes may have surface ruptures that can be reported within a short period of time.

5.14 Implications for Regional Tectonics

We have proposed that two of the aftershocks discussed here occurred in the vicinity of the proposed east-dipping decollement, one west-dipping backthrust event ruptured above the decollement, one strike-slip aftershock nucleated in the basement then ruptured through the overlying sedimentary layers, and two of the shocks occurred on basement-involved reverse faults (Figure 5.1b).

The two aftershocks in the vicinity of decollement ruptured along the Puli-Chusan lineation (Figure 5.11). In cross section these two aftershocks form a flat-ramp geometry. However, given the uncertainty in depth, Event 4 could have been at a shallower depth becoming a splay fault branching up from the decollement.

The west-dipping backthrust slip model above the decollement from Event 1 was assigned low level of confidence. Combined with the east-dipping decollement that ruptured during the mainshock, this west-dipping backthrust aftershock forms a pop-up structure, such as proposed to explain the pure shear type of microstructure deformation observed in the mountains to the north (Clark et al., 1993). Sandbox modeling by Lu et al. (2002) also predicted backthrusting in this region.

Two of the aftershocks show basement-involved reverse faulting. Although both of them were assigned low confidence levels, the deep focal depths determined from our analysis are robust, as inversions using shallow focal depths could not generate satisfactory waveform fits. The steep dip angles of our preferred fault models suggest that these events ruptured on pre-existing weak zones, presumably a steeply dipping normal fault along the passive margin. In fact, many studies have proposed reactivated normal faults in this region based on oil company reflection data and well log data (e.g. Suppe, 1984). Our results suggest that such structures may currently be seismogenic.

Though assigned a low confidence level, our slip model for Event 4 is a west-dipping fault under the decollement, which is consistent with the results from Carena et al. (2002) and Chen et al. (2002). Repeated west-dipping reverse faulting events under the decollement could uplift the western part of the decollement over a long period of time. Thus if the regional decollement is flat in this region (Carena et al., 2002) or only dips slightly to the south (Wang et al, 2002), this type of basement reverse faulting could

be a transient or young feature. Another possibility is a duplex style of deformation between two sub-horizontal main detachment faults. If the causative plane dips to the east, the preferred slip model will be more consistent with the sub-parallel fault model from Kao and Chen because the alternative preferred model has a focal depth of 25 km (Figure 5.1a).

Event 6 occurred on a basement-involved reverse fault under the eastern plains. Although at greater depth, basement faults in this region can pose significant seismic hazard because they lie directly beneath cities. The strike of this fault is sub-parallel to the topographic lineation further to the east (Figure 5.12). Like other basement-involved aftershocks in this study, this aftershock's fault plane may be controlled by the structures in the underthrusting passive margin. If the earthquake ruptured on the west-dipping fault plane, our analysis shows that the preferred focal depth is about 8 km, which is within the basement.

Event 3 is a strike-slip event initiated within the basement but the asperity is mostly concentrated at shallow depth along and above the proposed decollement. In fact the slip seems to have a rake consistent with the shallow dip of decollement 5 to 10 km to the north. Our result provides evidence of basement deformation propagating to the overlying sedimentary layers and generating large slip at shallow depth. If true, this will be one of the first studies that show deformation style above the decollement being influenced by active deformation within the basement. Because of the shallow asperity, we predicted that deformation may be detectable in GPS measurements.

Except for Event 4, the azimuths of the P axes derived from our preferred models are roughly about N70^{o}E (Figure 5.4), consistent with the current relative plate motion. However, the fault plane orientations of these 6 aftershocks are very different. This suggests that the kinematics of these large aftershocks is mainly controlled by tectonic stress, although they occurred on pre-existing weak zones that do not have similar attitudes. The triggering of the aftershocks may be closely related to stress perturbation due to the mainshock rupture, suggested by Kao and Angelier (2001) based on moment tensor data.

Post-seismic deformation has been studied extensively for recent large earthquakes (e.g. Bürgmann et al., 2002). There is an excellent post-seismic GPS dataset (Hsu et al., 2002) for the Chi-Chi earthquake sequence. Chi and Dreger (2002) documented the large contribution from Event 5 to the post-seismic deformation, composing up to 30% of the total post-seismic displacement at several stations near this event. Here we forward-predicted the GPS deformation using a half-space elastic structure (Okada, 1992) for the slip models of the 6 aftershocks. The cumulative aftershock-related displacement from these 6 aftershocks was as high as 10 cm at some GPS stations, explaining at least 80% of the post-seismic deformation observed in the southern half of the hanging block where these aftershocks occurred (Figure 5.13).

5.15 Conclusion

We have inverted strong motion data to determine the finite source parameters for six large aftershocks of the 1999 Chi-Chi, Taiwan earthquake sequence (Figure 5.12). Of these events, five showed dip-slip motion and one was strike-slip in nature. We tested more than 1000 inversions for each event and documented the variation in the waveform fit due to different input parameters, including changes in the station configuration, the focal mechanism, the hypocentral location, the rupture velocity, and the dislocation rise time. We then assigned confidence levels for each event based on these tests and by comparing the resulting slip models with other geologic and geophysical data.

Three of the aftershock slip models were assigned high levels of confidence due to good waveform fits and good correlation with results from reflection data, seismicity, and geologic maps. Particularly, the slip model for Event 2 correctly depicted the fault orientation imaged by recently released reflection data.

Except for one strike-slip event, which started deep, and one event located to the west in the footwall of the mainshock, the ruptures of the other events began in the vicinity of the decollement near the mainshock slip. We have high confidence in the slip models that ruptured updip on the decollement. However, there is also strong evidence of updip rupture to the east, forming a pop-up structure, or downdip rupture to the west below the decollement, suggesting some of the four aftershocks may not have ruptured on the proposed decollement.

We use the sensitivity test results to place bounds on the source parameter space that will give relatively good waveform fits. In another words, we have tested different input parameters to determine their influence on inversion results for these Mw 5.8-6.4 earthquakes in Taiwan region. We found that inversions using 10 stations usually gave stable results, provided there are no timing errors. Jack-knife tests show that with fewer stations we can still derive similar slip models, but the results are not as robust. The accuracies of the focal mechanism determinations have a strong influence on the waveform fits and the slip model. Particularly for the thrust events, the input dip angle must be correct to within 20^{o}, otherwise the variance reduction drops by as much as 10%. For the single strike-slip event, the strike must also be within 20^{o} of the true strike. Hypocentral locations must be within 5 km of the actual locations, which is close to the smaller dimension of the slip patches we modeled. In some cases we found that to correctly determine the causative fault, we need more precise hypocentral information. Our results suggest that the rupture velocity can trade-off with the dip angle of the causative fault plane chosen and that the inversions are not very sensitive to the dislocation rise time. Although these may not be general results, this study does show that there can be significant trade-offs between the fixed parameters of the inversion and that they can bias the results.

Our results provide more detailed spatial resolution of the slip compared with the moment tensor results. Two of the aftershocks ruptured along the Puli-Chusan lineation, where the mainshock rupture stopped. Three of the aftershocks show evidence of basement-involved deformation. In particular, we found a strike-slip event that nucleated

within the basement but the asperity is mainly located within the overlying sediments, strongly suggesting that basement structures play an important role in surface deformation. Five out of the 6 slip models have P-axes with azimuths consistent with current relative plate motion. However, the fault orientations of these aftershocks are very different. We interpreted this to mean that large aftershocks are triggered by the stress perturbation of the mainshock on pre-existing structures. However, the kinematics of the aftershocks remains consistent with regional tectonic stress.

5.15 Acknowledgments.

We thank Dr. Willie Lee for providing the strong motion data from Central Weather Bureau (CWB) of Taiwan and Dr. Win-Gee Huang for the strong motion data from IES, Academia Sinica of Taiwan. Dr. S.-B. Yu is thanked for providing post-seismic GPS data. We appreciate Dr. Honn Kao for his seismicity data. We thank CWB for providing their aftershock seismicity data and Dr. C.Y. Wang of National Central University for providing reflection data. We thank Dr. Peggy Hellweg and Dr. Donald Reed for their constructive comments. This research is funded by NSF Grant EAR-0000893 and PEER Lifelines 1E06.

Table 5.1: Source parameters and results of the inversions.

Event number	1	2	3	4	5	6
Origin Time	0920/17:57:15.310	0920/18:03:41.160	0920/21:46:37.490	0922/00:14:40.770	0925/23:52:49.509	1022/02:18:56.930
Long	121.01±0.03	120.86±0.03	120.82±0.04	121.08±0.04	121.01±0.03	120.45±0.03
Lat	23.94±0.02	23.81±0.05	23.60±0.04	23.81±0.06	23.87±0.04	23.53±0.04
Depth (km)	8±5	8±4	18±6	10±8	16±7	16±6
M_0 (dyne-cm)	7.15e+024	2.53e+25	2.2e+25	2.5e+25	3.7e+25	1.7e+25
Mw	5.8	6.2	6.2	6.2	6.3	6.1
Strike	200±25	0±20	330±15	165±25	5±15	20±30
Dip	41±25	10±20	89±10	70±25	30±10	75±10
Rake	78±25	80±20	15±15	100±25	100±10	90±15
S/D/R Mw						
Harvard CMT*	N/A	N/A	336/89/1 6.4	183/80/97 6.4	12/20/95 6.5	46/52/125 5.8
NEIC	N/A	N/A	N/A	187/69/108 6.3	N/A	26/55/103 5.9
ERI	N/A	N/A	N/A	175/85/88 6.4	35/25/115 6.4	5/44/74 5.9
BATS	N/A	329/35/59 6.2	242/55/-157 6.3	13/25/124 6.2	50/44/126 6.2	219/29/129 5.9
CHEN (M_L)	N/A	N/A	N/A	161/69/87 6.8	351/25/60 6.8	N/A
Vrup (km/s)	1.5 (1.3-2.6)	1.6 (1.3-3.5)	2.4 (2.0-2.8)	2.6 (2.0-3.0)	3.2 (1.8-3.6)	2.0 (1.6-2.3)
DRT (sec)	0.2 (0.1-0.6)	0.2 (0.1-0.8)	0.7 (0.2-0.9)	0.7 (0.1-0.9)	0.3 (0.1-0.9)	2.0 (1.6-2.3)
Max Slip (cm)	46	231	85	83	162	205
Str. Drop (MPa)	5.3	6.2	3.8	4.6	5.9	9.9
Asper. Dim	12 x 4	10 x 10	5 x 25	6 x 20	6 x 22	4 x 14
Fault Dim.	24 x 24	14 x 15	24 x 19	24 x 36	30 x 21	18 x 18
# of Stations	13	13	9	9	11	14
VR (%)	46	56	56	48	72	60
Confid. Level	low	high	high	low	high	low
CF S/D/R VR%	35/50/100 48	190/80/92 43	240/75/179 42	318/22/64 23	173/61/84 55	200/15/90 46

(S/D/R: Strike/Dip/Rake; Str. Drop: Stress Drop; Asperity Dimension and Fault Dimension are in km x km; VR: Variance Reduction; CF: conjugate Fault)

Table 5.2: Parameters Tested in the Inversions

Event number	1	2	3	4	5	6
Origin Time	0920/17:57:15.310	0920/18:03:41.160	0920/21:46:37.490	0922/00:14:40.770	0925/23:52:49.509	1022/02:18:56.930
Long	121.00-121.06 0.01	120.80-120.91 0.01	120.77-120.87 0.01	121.03-121.13 0.01	120.96-121.06 0.01	120.35-120.45 0.01
Lat	23.90-23.96 0.01	23.76-23.86 0.01	23.56-23.65 0.01	23.76-23.86 0.01	23.81-23.91 0.01	23.46-23.56 0.01
Depth (km)	2-30 2	2-30 2	2-24 2	6-34 2	2-30 2	6-26 2
Rup. Vel. (km/s)	0-3.2 0.1	1.0-3.2 0.2	1.0-2.8 0.1	1.0-3.6 0.2	0.2-3.6 0.2	1.0-4.0 0.1
DRT (s)	0.1-1.0 0.1	0.1-1.0 0.1	0.2-1.0 0.1	0.1-1.0 0.1	0.1-0.9 0.1	0.1-0.9 0.1
Strike E-dipping	320 330 340 350 0 10 20 25 30 35 40 50 60	355 0 5 10 15 20 25 30 35 40	310 320 325 330 335 340 350 0	330 340 350 0 10 20	0 5 10 15 20 15 30 35 40	0 10 20 30 40 50 60
Dip E-dipping	10 20 30 40 50 60 70 80	5 10 15 20 25 30 35	80 85 89	10 20 30 40 50 60	10 15 20 25 30 40 45 50 55	50 55 60 65 70 75 80 85
Rake E-dipping	60 70 80 90 100 110 120 130	70 80 85 90 100 110 120	-5 0 5 10 15 20 25 30	70 80 90 100 110 120	085 090 095 100 105 110 115 120 125	60 70 80 90 95 100 110 120 130
Strike W-dipping	150 160 170 180 190 200 210	170 180 190 200 210	185 190 200 210 220 230 240 250	140 145 150 155 160 165 170 190 195 200 205 210 215	160 170 180 190 200 210 220 230	170 180 190 200 210 220
Dip W-dipping	20 30 40 50 60 70 80	45 55 65 75 85	60 70 80 85	40 50 60 65 70 75 80 85	30 40 50 60 70 80	5 10 15 20 25 30 35 40 50
Rake W-dipping	40 50 60 70 80 90 100	70 80 90 100 110 120)	140 150 160 170 180	70 80 90 100 110 120	50 60 70 80 90 100	50 60 70 80 90 100 110 120

(For latitude, longitude, depth, rupture velocity, dislocation rise time, the formats are: minimum-maximum increment)

Table 5.3

1D velocity model used for Green's function calculation

Thickness (km)	***Depth (km)***	***Vp (km/s)***	***Vs (km/s)***	***Density (g/cm^3)***	***Qp***	***Qs***
2.2	**2.2**	**4.5**	**2.6**	**1.8**	**200**	**100**
2.2	**4.4**	**4.85**	**2.8**	**2.05**	**600**	**300**
2.2	**6.6**	**5.3**	**3.06**	**2.25**	**600**	**300**
2.2	**8.8**	**5.6**	**3.23**	**2.39**	**600**	**300**
4.5	**13.3**	**5.84**	**3.37**	**2.5**	**600**	**300**
4.5	**17.8**	**6.13**	**3.54**	**2.64**	**600**	**300**
7.5	**25.3**	**6.28**	**3.63**	**2.7**	**600**	**300**
8.5	**33.8**	**6.6**	**3.81**	**2.85**	**600**	**300**
5	**38.3**	**6.87**	**3.97**	**2.97**	**600**	**300**
21.5	**60.3**	**7.43**	**4.29**	**3.3**	**600**	**300**
25	**85.3**	**7.8**	**4.5**	**3.3**	**600**	**300**

Figure 5.1a. Location map. Stars show the locations of the 6 aftershocks. Triangles are the strong motion stations used in the finite source inversions. The numbers below each triangle are the event/events for which this station was used. Surface rupture from the mainshock is plotted for reference. The mainshock asperity is bounded by the towns Sanyi, Puli, and Chusan (Chi et al., 2001). The cross section in the upper left corner shows a schematic with moment tensor solutions for some events of the Chi-Chi earthquake sequence (Kao and Chen, 2000) near these 6 large aftershocks. Two models have been proposed to explain these moment tensor results. Both have an east-dipping decollement represented by the solid line. One model (model 1) proposes another east-dipping fault under the decollement (Kao and Chen, 2000) while another model (model 2) suggests that some of the seismicity below the decollement is on a west-dipping fault (Carena et al., 2002; Chen et al., 2002).

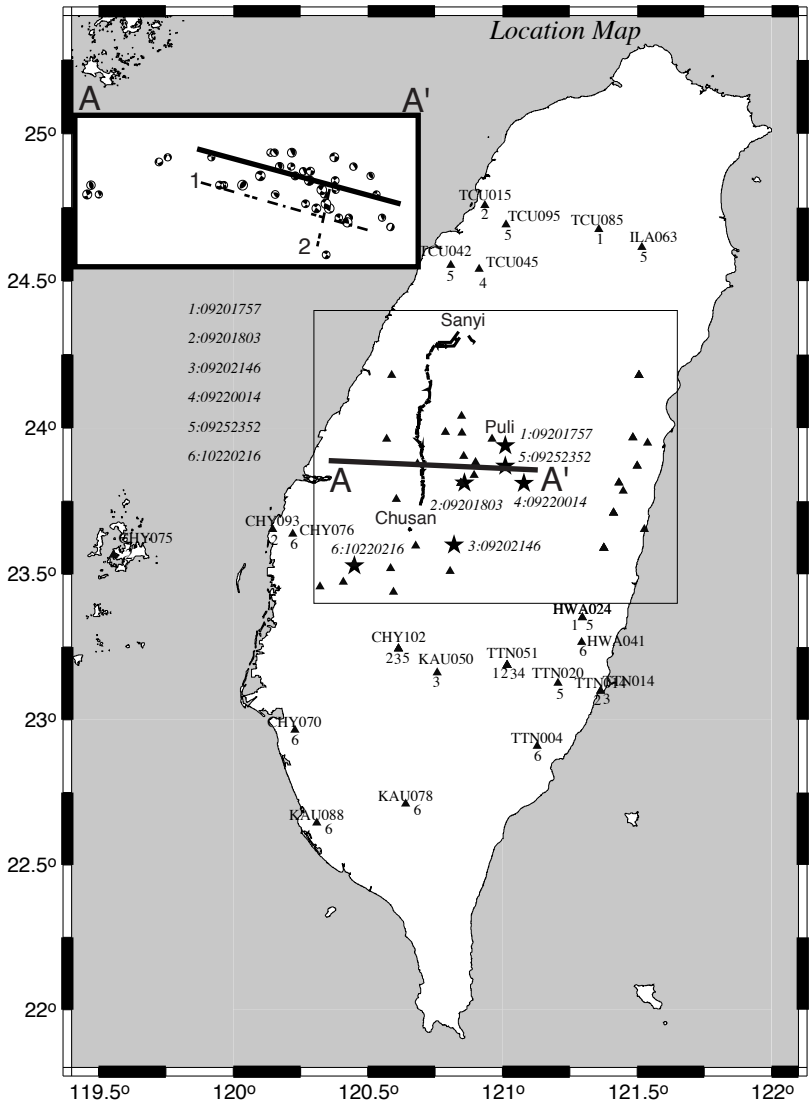
Location Map
A
A'
1
2
25º
24.5º
24º
23.5º
23º
22.5º
22º
119.5º
120º
120.5º
121º
121.5º
122º
TCU015
TCU095
TCU085
ILA063
TCU042
TCU045
1:09201757
2:09201803
3:09202146
4:09220014
5:09252352
6:10220216
Sanyi
Puli
Chusan
CHY093
CHY076
CHY075
CHY102
KAU050
TTN051
TTN020
TTN014
HWA024
HWA041
CHY070
TTN004
KAU078
KAU088

Figure 5.1b. An enlarge figure from portion of Figure 5.1a. The stars are the preferred epicenters, which may differ from epicenters reported in other studies. The dot color shows the variance reduction derived from inversions using that particular location as epicenter. It shows how rapidly the waveform fits, measured by variance reduction (VR), deteriorate if the epicentral information is incorrect. Results for Event 5 are shifted to the east for clear presentation. The blue rectangles are the fault dimensions of the preferred slip models. Note that Event 2 and Event 5 are located along the lineation defined by the towns Puli and Chusan. Chi et al. (2001) has proposed that mainshock rupture stopped along this lineation. The cross section in the upper right corner shows a schematic with possible rupture scenarios for the aftershocks we studied. Depending on the causative fault plane and its dip angle, these aftershocks appear to have ruptured on the decollement, an east-dipping splay fault, a backthrust, or a basement-involved fault.

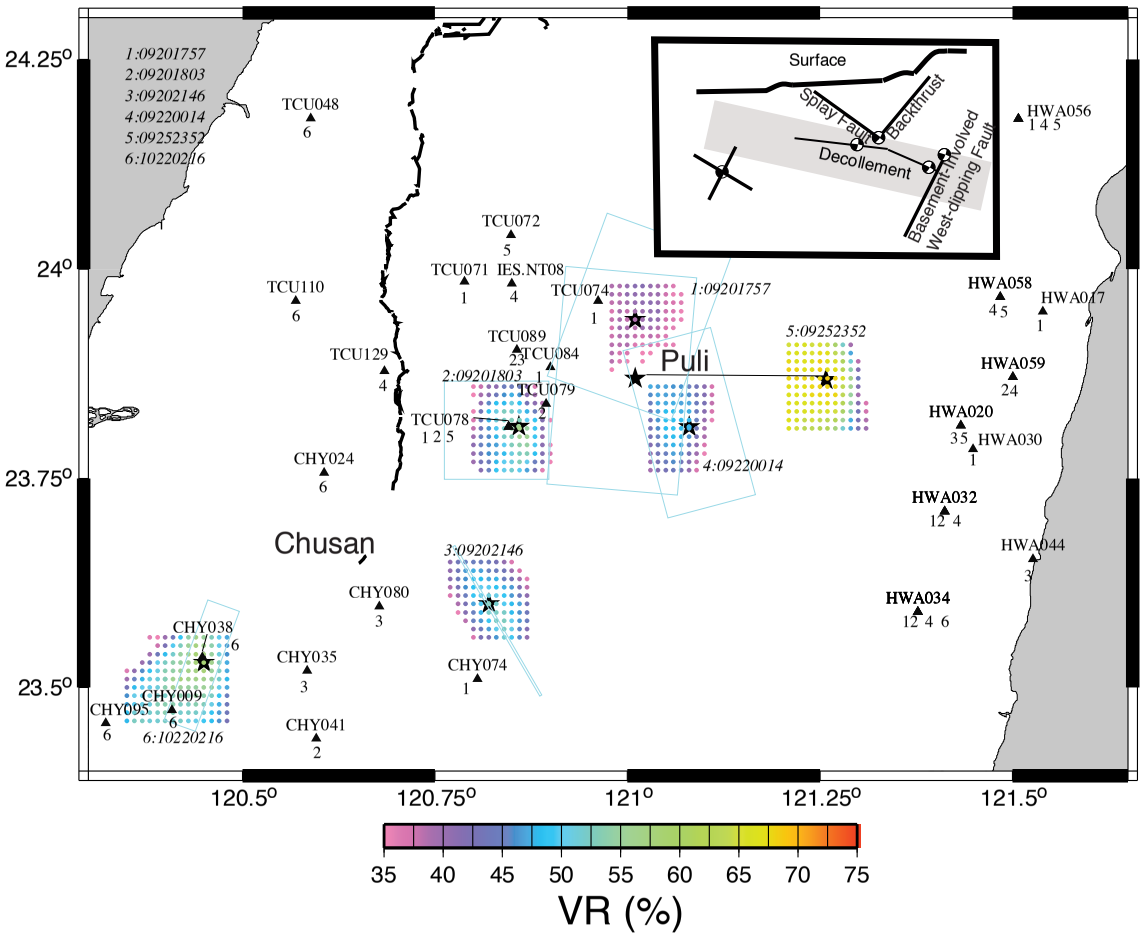
1:09201757
2:09201803
3:09202146
4:09220014
5:09252352
6:10220216
Surface
Splay Fault
Backthrust
Decollement
Basement-involved
West-dipping Fault
Puli
Chusan
TCU048
TCU072
TCU071
IES.NT08
TCU074
TCU110
TCU129
TCU089
TCU084
TCU079
TCU078
CHY024
CHY080
CHY035
CHY074
CHY041
CHY038
CHY009
CHY095
HWA056
HWA058
HWA017
HWA059
HWA020
HWA030
HWA032
HWA044
HWA034
24.25°
24°
23.75°
23.5°
120.5°
120.75°
121°
121.25°
121.5°
35 40 45 50 55 60 65 70 75
VR (%)

Figure 5.2. An example of the particle motion plots we generated to pick stations, to check the consistency of the waveforms with the focal mechanism, and to determine the direction of the horizontal peak ground velocity (HPGV) and the aspect ratio of the particle motion in the populated areas. Filtered observed horizontal waveforms of Event 2 (09201803) were plotted, because this event clearly shows the shear wave radiation pattern for a westward thrusting event. The star shows the hypocenter. The directions of the HPGV, dominated by shear waves and surface waves, are mostly parallel to the backazimuth directions, consistent with a thrust mechanism. A strike-slip mechanism on a vertical fault (e.g. Event 3 of this study) has HPGV directions perpendicular to the backazimuth directions. As a result, the urban region west of the aftershocks experienced mostly E-W strong motion during the thrust-type aftershocks. The aspect ratio is the ratio between the short axis and the long axis of the particle motion ellipse. Note the strong westward directivity of this event.

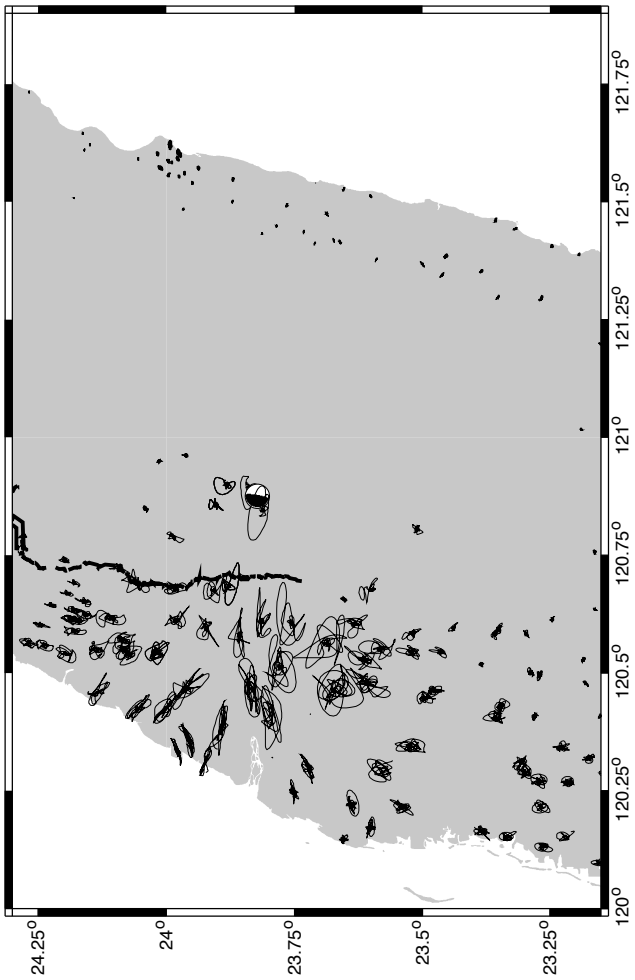
120°
120.25°
120.5°
120.75°
121°
121.25°
121.5°
121.75°
24.25°
24°
23.75°
23.5°
23.25°

Figure 5.3. The slip model for Event 1 (09201757) and its waveform fits. The VR of this slip model is 46% and we assigned low confidence level for this model. The star shows the location of the hypocenter which corresponds to a depth of 8 km and the empty circles are the aftershock seismicity within 5 km of the fault, based on data from the Central Weather Bureau and Kao and Chen (2000). We picked the west-dipping fault as the preferred model because, in addition to the good waveform fits, its slip patch correlates with aftershock seismicity. See Table 5.2 for parameters and results of this model. The lower panel shows the filtered velocity waveforms as solid lines and the synthetics as dashed lines. Each time series is 50 sec long and the amplitude of the largest waveform, E component of TCU074, is 0.0269 m/s.

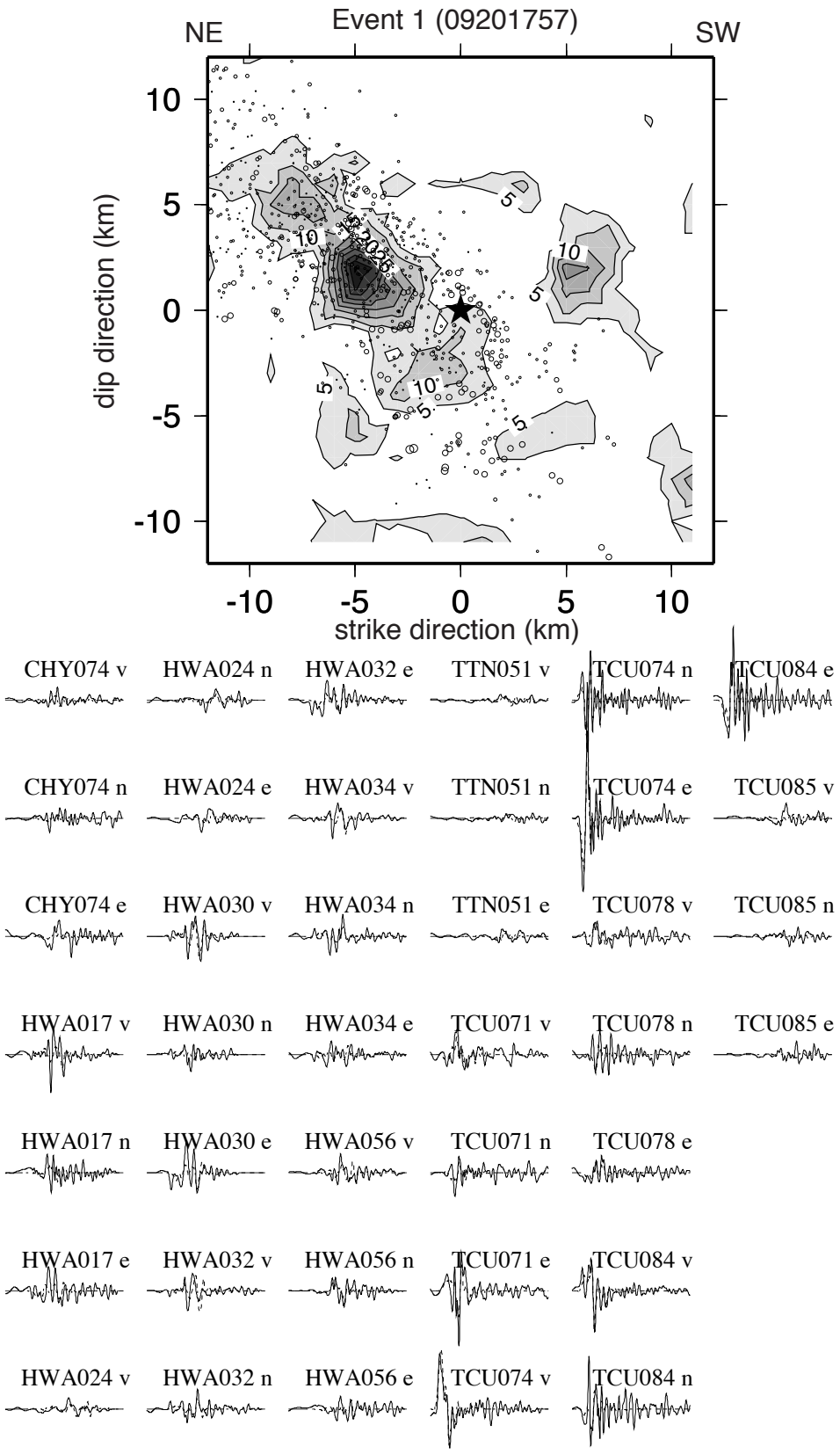
Event 1 (09201757)
NE
SW
dip direction (km)
strike direction (km)
10
5
0
-5
-10
-10
-5
0
5
10
CHY074 v
HWA024 n
HWA032 e
TTN051 v
TCU074 n
TCU084 e
CHY074 n
HWA024 e
HWA034 v
TTN051 n
TCU074 e
TCU085 v
CHY074 e
HWA030 v
HWA034 n
TTN051 e
TCU078 v
TCU085 n
HWA017 v
HWA030 n
HWA034 e
TCU071 v
TCU078 n
TCU085 e
HWA017 n
HWA030 e
HWA056 v
TCU071 n
TCU078 e
HWA017 e
HWA032 v
HWA056 n
TCU071 e
TCU084 v
HWA024 v
HWA032 n
HWA056 e
TCU074 v
TCU084 n

Figure 5.4. The results of sensitivity tests on the focal mechanism for each event. The P axis of each focal mechanism tested is plotted in lower hemisphere stereonet projection. The left stereonets show the east-dipping fault planes, the right ones the west-dipping planes. The color shows the variance reduction. Note VR deteriorates fastest when the plunge of the P axis changes, implying the waveform fits are most sensitive to the dip, and possibly rake, of the focal mechanism for the thrust events. For the strike-slip aftershock (Event 3), VR is more sensitive to strike. We interpreted this to be the result of the amplitude of the S wave radiation pattern, which controls the inversion results. The star shows the P axis of the preferred focal mechanism.

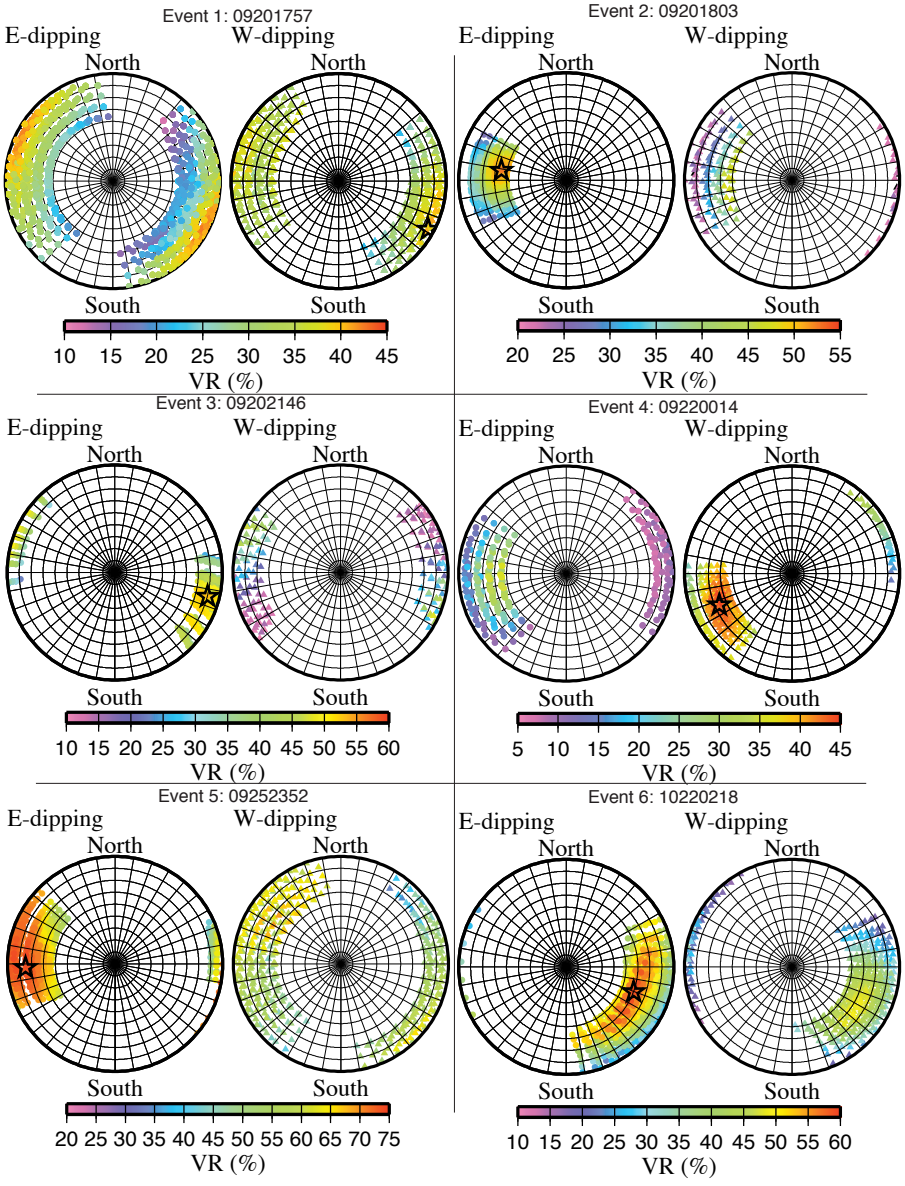
Event 1: 09201757
E-dipping
W-dipping
North
South
10 15 20 25 30 35 40 45
VR (%)
Event 2: 09201803
20 25 30 35 40 45 50 55
Event 3: 09202146
10 15 20 25 30 35 40 45 50 55 60
Event 4: 09220014
5 10 15 20 25 30 35 40 45
Event 5: 09252352
20 25 30 35 40 45 50 55 60 65 70 75
Event 6: 10220218
10 15 20 25 30 35 40 45 50 55 60

Figure 5.5. Variation in the waveform fit derived from sensitivity tests of focal depth, rupture velocity, and dislocation rise time (DRT). The solid lines show the east-dipping faults while the dashed lines are the conjugate west-dipping faults. For event 3 the solid lines are the NW-SE trending faults. Note that VR drops off quickly if the focal depth is more than 5 km from the preferred focal depth. VR is also sensitive to the rupture velocity but less sensitive to dislocation rise time. Event 4 shows evidence of the interrelationship between the causative fault plane, focal depth, and rupture velocity discussed in the text and Figure 5.10.

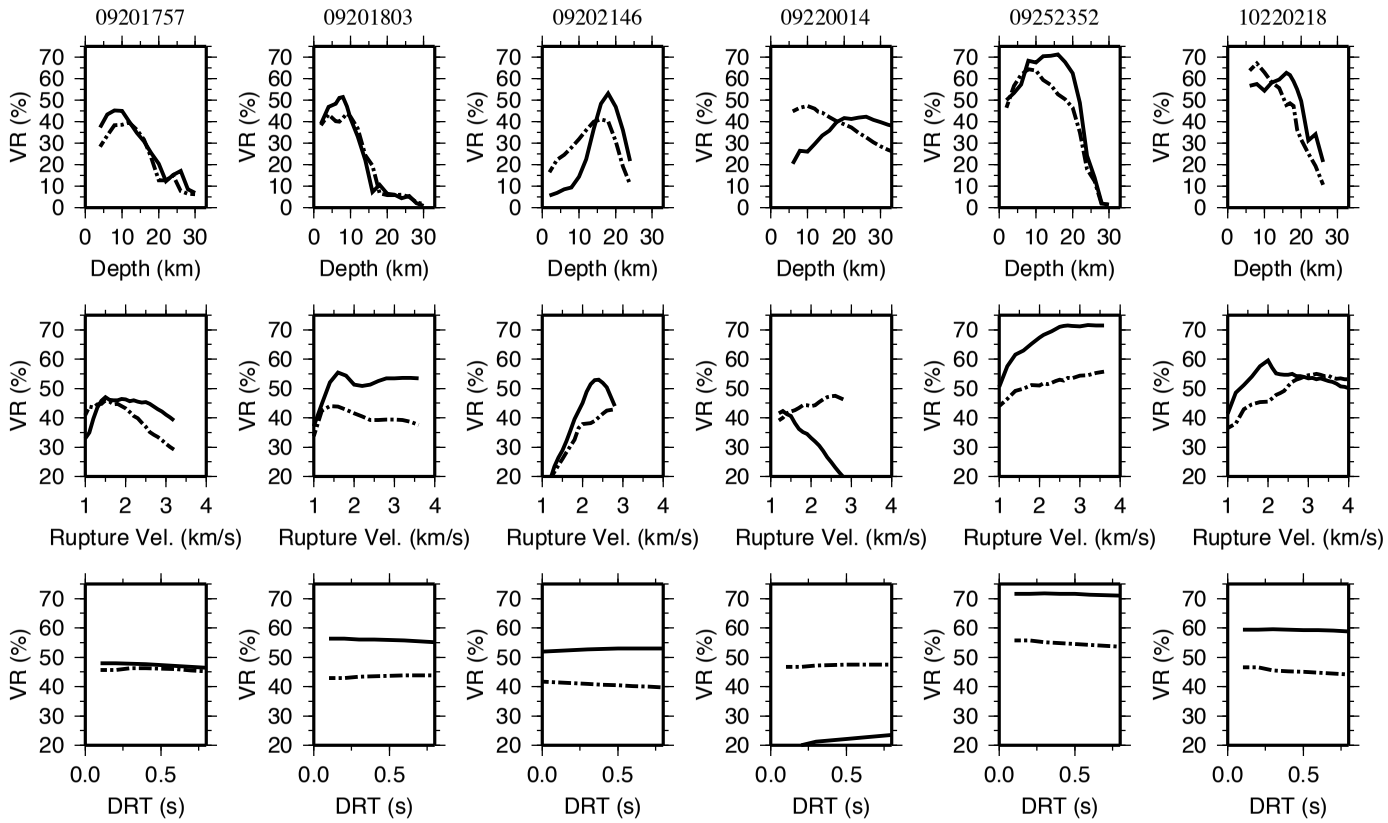
09201757
09201803
09202146
09220014
09252352
10220218
VR (%)
Depth (km)
Rupture Vel. (km/s)
DRT (s)

Figure 5.6. The slip model and waveform fits for Event 2 (09201803). The VR of this slip model is 56% and we assigned high level of confidence to this model. The aftershocks are located SW of this east-dipping asperity. The east components of stations TCU078 and TCU079 show strong directivity effects. The length of the waveforms is 50 sec and the largest amplitude of the waveform is -0.2127 m/s on the E component of TCU078.

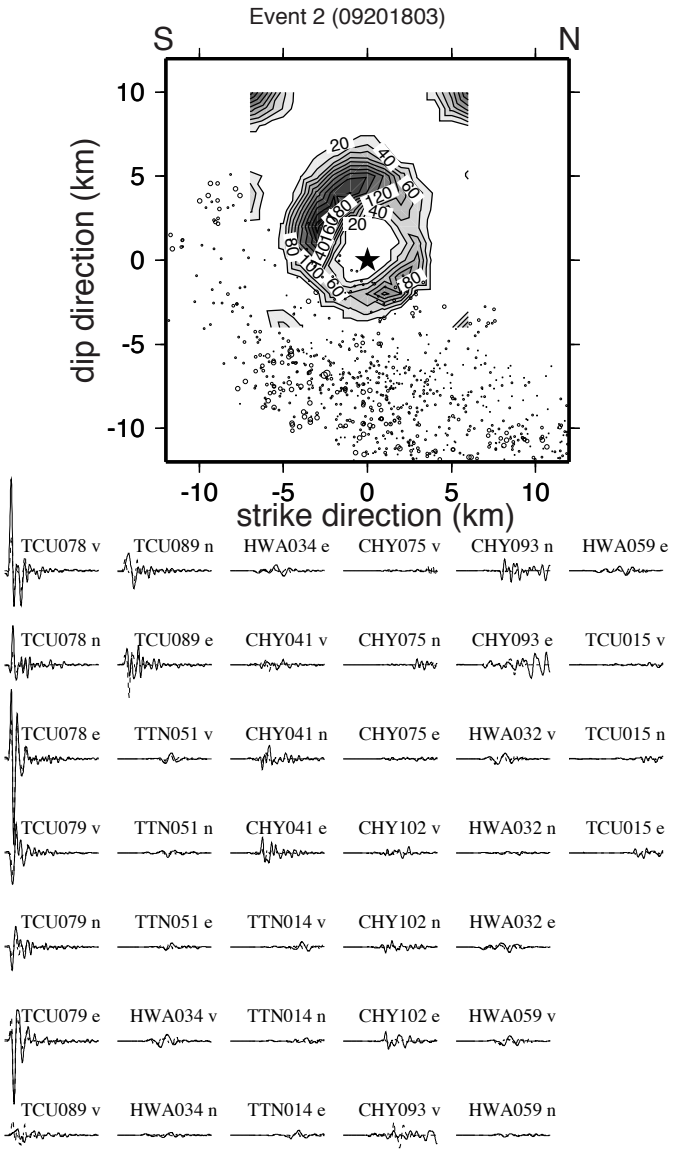
Event 2 (09201803)
S
N
dip direction (km)
strike direction (km)
10
5
0
-5
-10
20
40
60
80
100
120
140
160
180
TCU078 v
TCU089 n
HWA034 e
CHY075 v
CHY093 n
HWA059 e
TCU078 n
TCU089 e
CHY041 v
CHY075 n
CHY093 e
TCU015 v
TCU078 e
TTN051 v
CHY041 n
CHY075 e
HWA032 v
TCU015 n
TCU079 v
TTN051 n
CHY041 e
CHY102 v
HWA032 n
TCU015 e
TCU079 n
TTN051 e
TTN014 v
CHY102 n
HWA032 e
TCU079 e
HWA034 v
TTN014 n
CHY102 e
HWA059 v
TCU089 v
HWA034 n
TTN014 e
CHY093 v
HWA059 n

Figure 5.7. Slip model and waveform fits for Event 3 (09202146). The VR of this slip model is 56% and we assigned high confidence level to this model. The focal depth for this event is 18 km but the asperity mainly ruptures at shallow depth in sedimentary layers. This event shows strong evidence of active basement deformation affecting the shallow crust structures. The length of the waveforms is 50 sec and the largest amplitude of the waveform is -0.1046 m/s on the E component of CHY080.

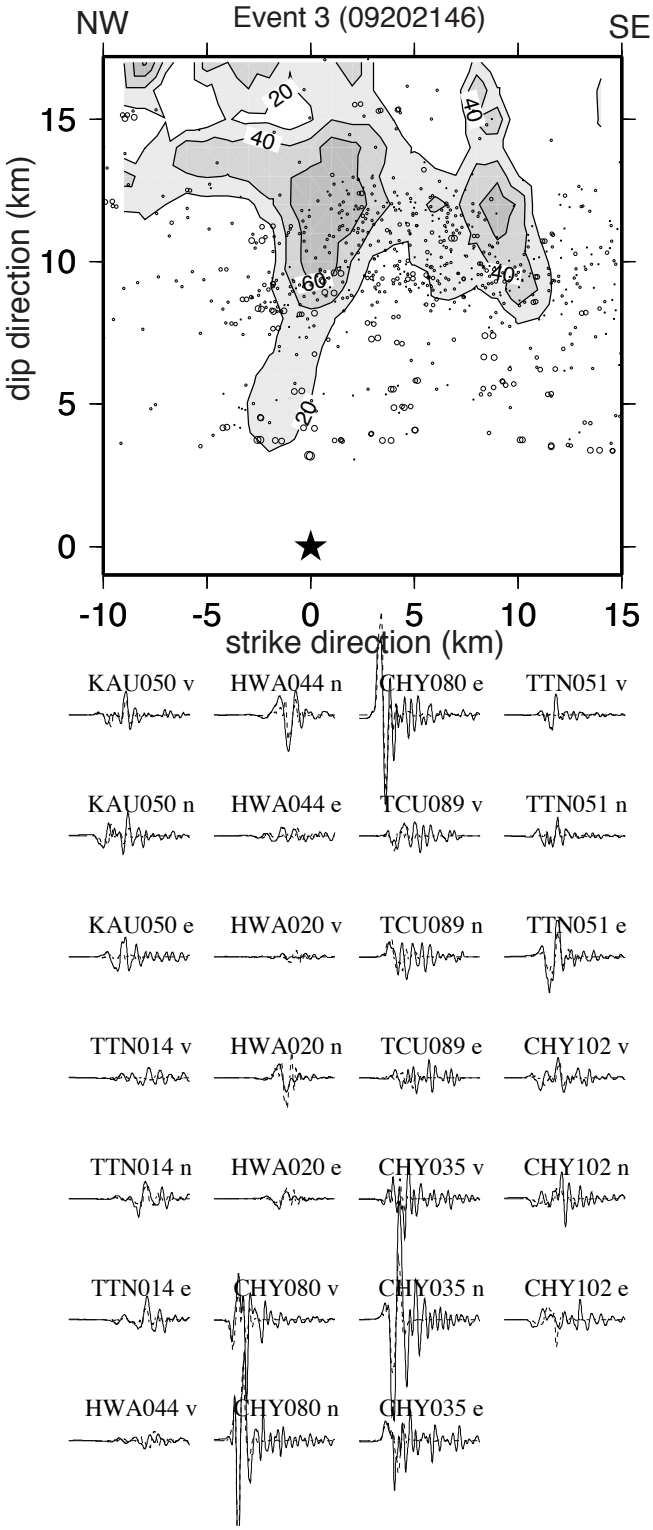
NW
Event 3 (09202146)
SE
dip direction (km)
strike direction (km)
15
10
5
0
-10
-5
0
5
10
15
20
40
60
KAU050 v
HWA044 n
CHY080 e
TTN051 v
KAU050 n
HWA044 e
TCU089 v
TTN051 n
KAU050 e
HWA020 v
TCU089 n
TTN051 e
TTN014 v
HWA020 n
TCU089 e
CHY102 v
TTN014 n
HWA020 e
CHY035 v
CHY102 n
TTN014 e
CHY080 v
CHY035 n
CHY102 e
HWA044 v
CHY080 n
CHY035 e

Figure 5.8. Slip model and waveform fits for Event 4 (09220014). The VR of this slip model is 48% and we assigned a low confidence level to this model. The aftershocks seem to surround the shallow part of the asperity. Many stations east of the epicenter (e.g. all the HWA stations) show surprisingly large amplitudes compared with the western stations, possibly due to a directivity effect from this west-dipping basement fault. The length of the waveforms is 50 sec and the largest amplitude of the waveform is 0.0196 m/s on the E component of TCU129.

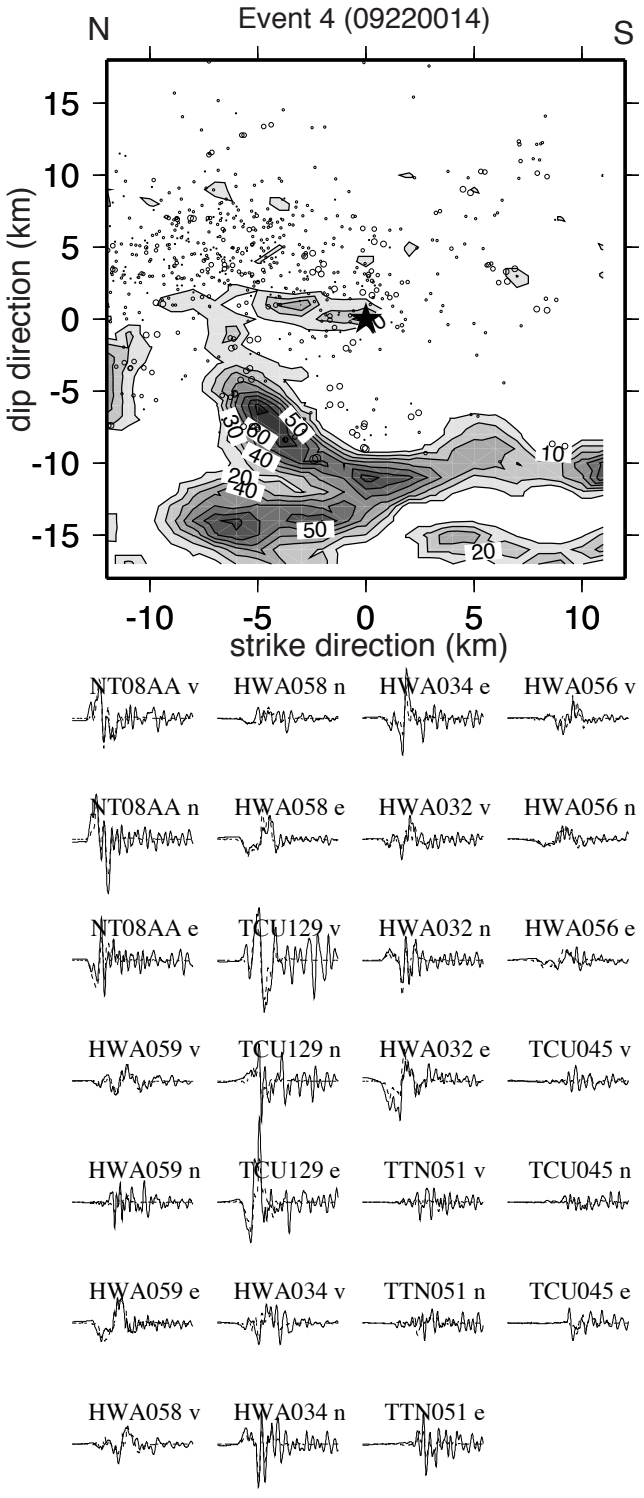
Event 4 (09220014)
N
S
dip direction (km)
strike direction (km)
15
10
5
0
-5
-10
-15
-10
-5
0
5
10
60
50
30
40
20
40
50
10
20
NT08AA v
HWA058 n
HWA034 e
HWA056 v
NT08AA n
HWA058 e
HWA032 v
HWA056 n
NT08AA e
TCU129 v
HWA032 n
HWA056 e
HWA059 v
TCU129 n
HWA032 e
TCU045 v
HWA059 n
TCU129 e
TTN051 v
TCU045 n
HWA059 e
HWA034 v
TTN051 n
TCU045 e
HWA058 v
HWA034 n
TTN051 e

Figure 5.9. Slip model and waveform fits for Event 5 (09252352). The VR of this slip model is 72% and we assigned a high confidence level for this model. The aftershocks are located south of the asperity. The length of the waveforms is 50 sec and the largest amplitude of the waveform is 0.1572 m/s on the E component of TCU078.

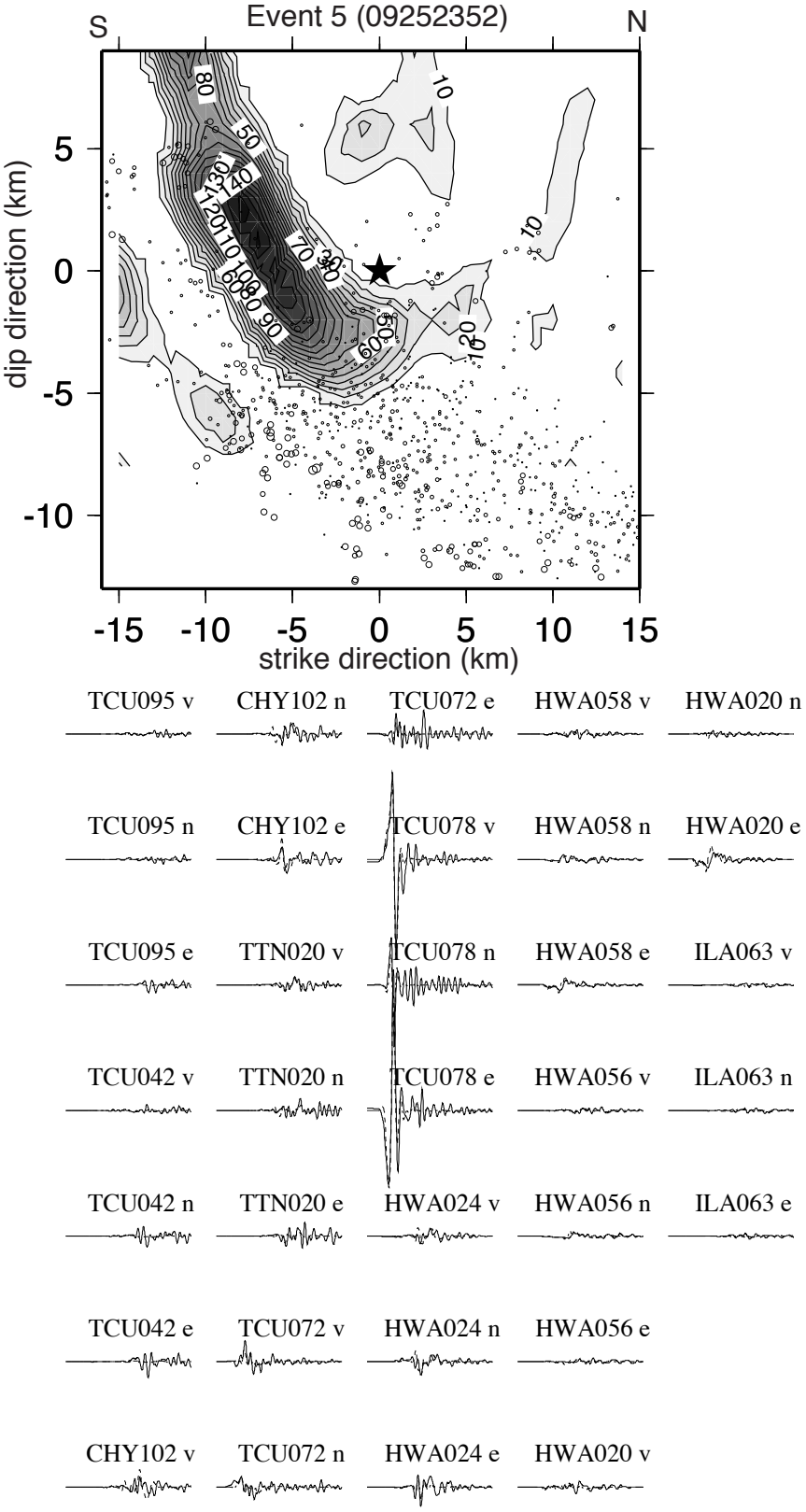
Event 5 (09252352)
S
N
dip direction (km)
strike direction (km)
-15
-10
-5
0
5
10
15
TCU095 v
CHY102 n
TCU072 e
HWA058 v
HWA020 n
TCU095 n
CHY102 e
TCU078 v
HWA058 n
HWA020 e
TCU095 e
TTN020 v
TCU078 n
HWA058 e
ILA063 v
TCU042 v
TTN020 n
TCU078 e
HWA056 v
ILA063 n
TCU042 n
TTN020 e
HWA024 v
HWA056 n
ILA063 e
TCU042 e
TCU072 v
HWA024 n
HWA056 e
CHY102 v
TCU072 n
HWA024 e
HWA020 v

Figure 5.10. Slip model and waveform fits for Event 6 (10220218). The VR of this slip model is 60%. Even though the waveform fits from 14 stations are very good we assigned a low confidence level for this model because we could not determine the causative fault plane conclusively. The aftershock seismicity is also scattered and hard to interpret. The length of the waveforms is 50 sec and the largest amplitude of the waveform is 0.1335 m/s on the E component of CHY009.

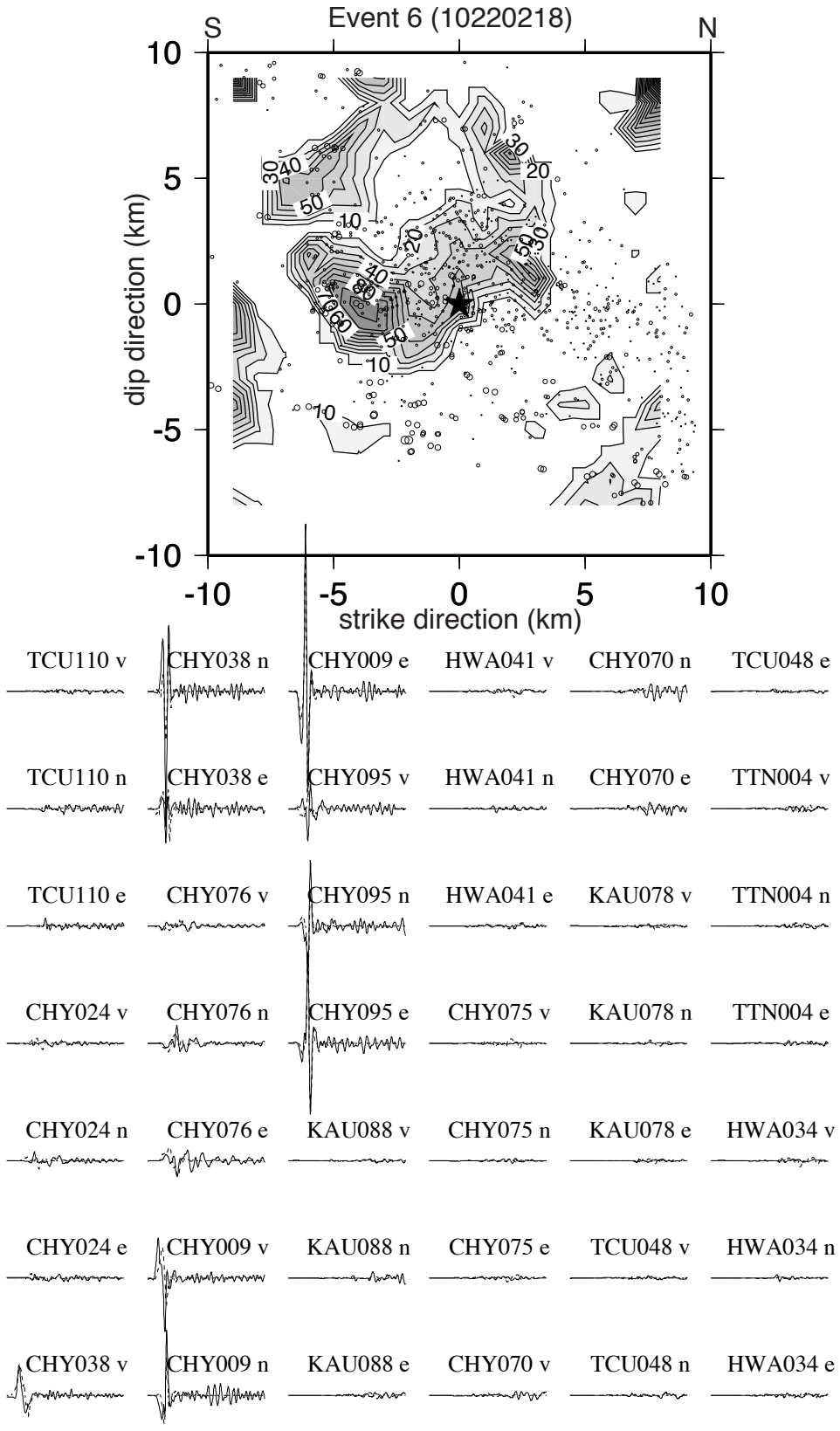
Event 6 (10220218)
S
N
10
5
0
-5
-10
dip direction (km)
-10
-5
0
5
10
strike direction (km)
TCU110 v
CHY038 n
CHY009 e
HWA041 v
CHY070 n
TCU048 e
TCU110 n
CHY038 e
CHY095 v
HWA041 n
CHY070 e
TTN004 v
TCU110 e
CHY076 v
CHY095 n
HWA041 e
KAU078 v
TTN004 n
CHY024 v
CHY076 n
CHY095 e
CHY075 v
KAU078 n
TTN004 e
CHY024 n
CHY076 e
KAU088 v
CHY075 n
KAU078 e
HWA034 v
CHY024 e
CHY009 v
KAU088 n
CHY075 e
TCU048 v
HWA034 n
CHY038 v
CHY009 n
KAU088 e
CHY070 v
TCU048 n
HWA034 e

Figure 5.11. Accurate hypocentral depth can help determine the causative fault plane because the conjugate faults may require very different hypocentral depths to fit the waveforms better. Assume we have the correct origin time, epicentral information, focal mechanism, and sufficient information carried in the waveforms to locate the slip in space ad time, a reliable hypocentral depth can help determine the causative plane. In this case, a very shallow hypocentral depth (hypocenter 1) will favor a down-dip rupture on the west-dipping fault plane. Also, the optimal rupture velocity on each of the conjugate faults can be used to infer the causative fault plane. That is, the dip of the causative fault plane will control the distance between the hypocenter and slip (rupture distances, marked as L1 and L2 in the figure), thus the preferred rupture velocity. In this case, the shallow east-dipping fault plane will have a shorter rupture distance, and thus a lower rupture velocity. For pure dip-slip rupture, the optimal rupture velocity for the steep-dipping plane divided by the optimal rupture velocity for the shallowly dipping plane is the cotangent of the dip of the shallower dipping fault. For slip not at the updip/downdip location, this becomes an apparent dip problem that involves a bit more algebraic manipulation.

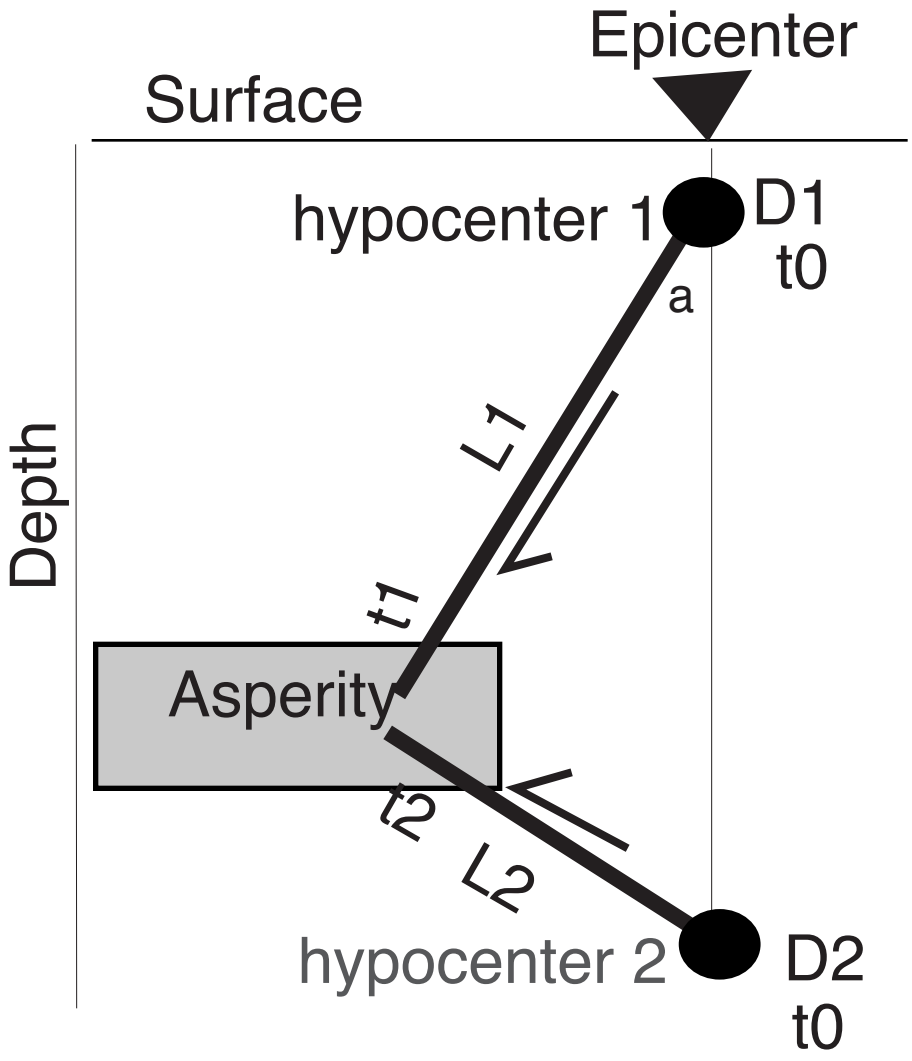

Rupture Vel. (Vr) = L/(t-t0)

$t1 = t2 \qquad \frac{L_1}{V_{r1}} = \frac{L_2}{V_{r2}}$

$\tan(a) = \frac{L_2}{L_1} = \frac{V_{r2}}{V_{r1}}$

Figure 5.12. The slip models from this study are plotted on the green topographic contour map. The red dots are the aftershock seismicity from Kao and Chen (2000) and the Central Weather Bureau. Note Event 5 ruptured just east of Event 2. Event 3 ruptured along NW trend in the aftershock seismicity. The cross section view of the slip model for Event 3 is plotted on the upper left corner.

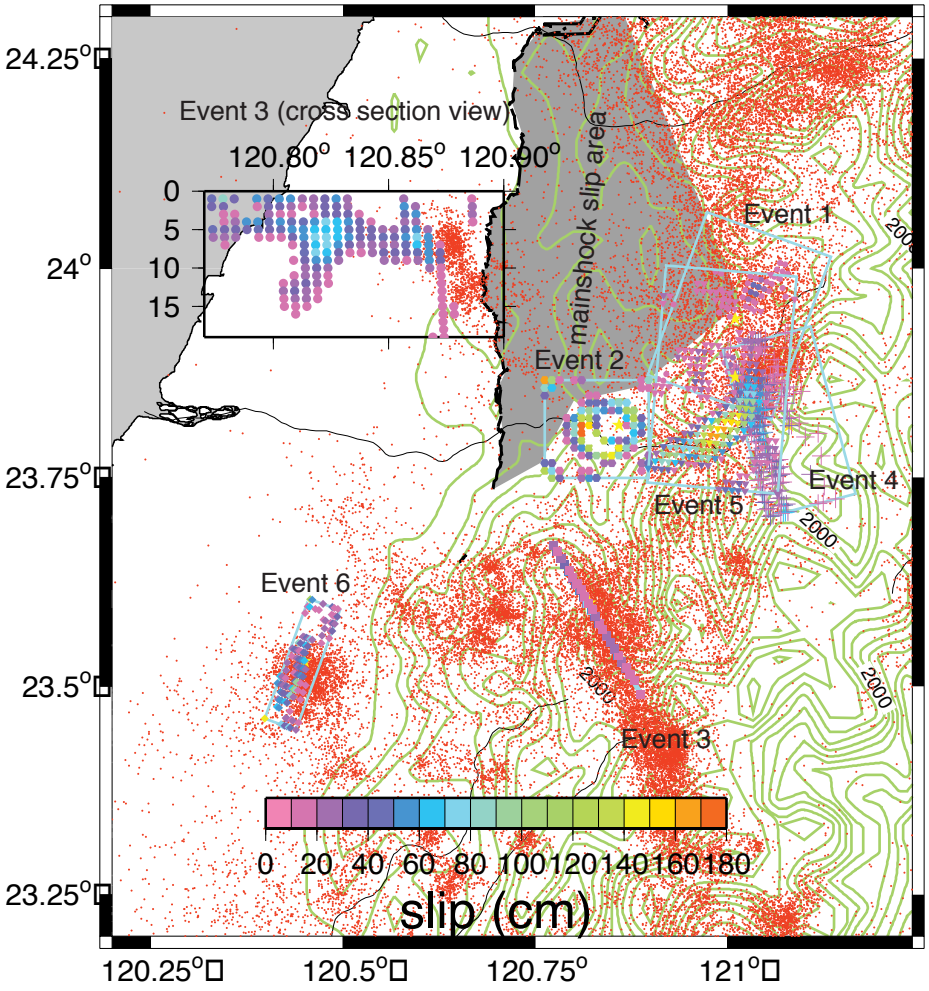
24.25°
24°
23.75°
23.5°
23.25°
120.25°
120.5°
120.75°
121°
Event 3 (cross section view)
120.80° 120.85° 120.90°
0
5
10
15
mainshock slip area
Event 1
Event 2
Event 3
Event 4
Event 5
Event 6
2000
0 20 40 60 80 100 120 140 160 180
slip (cm)

Figure 5.13. Post-seismic GPS displacement (Hsu et al., 2002) as large light-colored arrows. Cumulative synthetic GPS displacements derived from the 6 aftershock slip models using Okada's method (1992) as small black arrows. Note the cumulative GPS synthetics can explain at least 80% of the reported post-seismic GPS signals, especially in the southern part of the mainshock rupture where the aftershocks studied are located. One station near 120.76^{o}E and 23.7^{o}N shows opposite directions between the reported and forward-predicted GPS data. This station is near the nodal plane of the strike-slip aftershock (Event 3) so the discrepancy may be due to slight errors in its hypocenter or the strike of the fault.

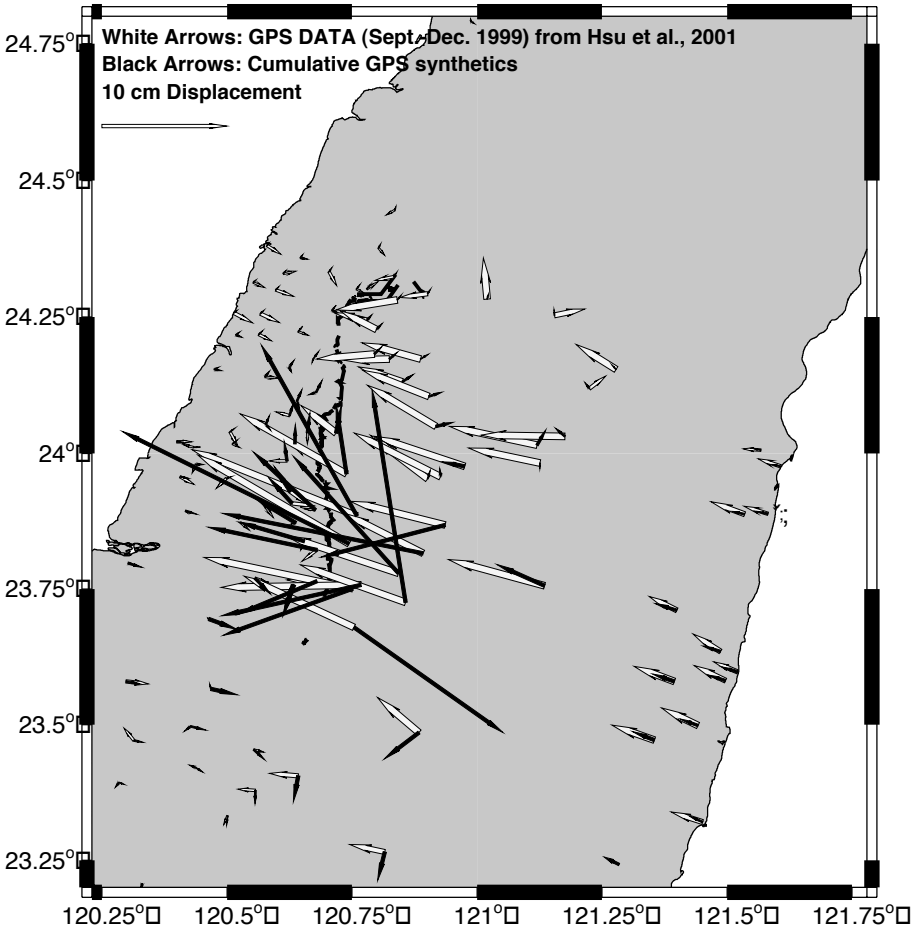
White Arrows: GPS DATA (Sept.-Dec. 1999) from Hsu et al., 2001
Black Arrows: Cumulative GPS synthetics
10 cm Displacement
24.75°
24.5°
24.25°
24°
23.75°
23.5°
23.25°
120.25°
120.5°
120.75°
121°
121.25°
121.5°
121.75°

Chapter 6

Conclusion

Seismic profiles, forward gravity modeling, and finite fault inversions were used to study the evolution of crustal deformation in and around Taiwan, from the subduction zone in the south to the collision zone in the central region. In the subduction zone (latitude=20^{o}N), we found that the gravity anomalies are consistent with those of a sedimentary accretionary prism. However, in order to match the 40 mgal increase in the gravity anomaly as the accretionary prism evolves from subduction into arc-continent collision at 21^{o}N, we find that 30% of the rear of the accretionary prism must be composed of materials with a density of 2.85 g/cm^{3}, which is greater than most sedimentary rocks. Based on the stratigraphy of the forearc basin, we interpret that tectonic wedging is a major mode of deformation along the rear of the accretionary prism (Figure 6.1). We propose that the floor thrust of the tectonic wedge might have been stepped down to incorporate forearc basement rocks into the rear of the accretionary prism, a subject of considerable debate in the more mature stages of the collision to the north.

To study active deformation in the collision, we inverted for finite source processes using the excellent strong motion data recorded during the 1999 Chi-Chi, Taiwan earthquake sequence. This unusually productive sequence of aftershocks consisted of six large aftershocks (Mw>5.8) and numerous small

events. This sequence occurred on faults that are part of the mature collision zone on land. Mainshock waveforms are best fit with a 30–degree eastward-dipping fault in the vicinity and up-dip of a proposed decollement. In map view, the slip of the mainshock lies within a triangle region bounded by the towns of Sanyi, Puli, and Chusan where the topography suggests that it occurred along a segment of the Chelungpu fault zone. Two of the aftershocks ruptured along the southern extension of the mainshock region. In cross section view (Figure 6.1), one strike-slip aftershock nucleated at basement depths, but ruptured upward and generated a large slip patch within the sedimentary strata, suggesting that basement structures can be seismogenic and can modify structures in overlying collision complex. This strike-slip event terminates near the southern end of the mainshock surface rupture. Two other aftershocks also occurred within the basement, although it was difficult to interpret which of the conjugate faults ruptured. One of the aftershocks appears to have ruptured on a westward-dipping fault beneath the decollement, consistent with the interpretation of other seismicity studies (c.f. Carena et al., 2002, Chen et al., 2002). Another aftershock occurred on an eastward-dipping reverse fault beneath an urban region. One aftershock was interpreted as having ruptured on a westward-dipping backthrust above the decollement, although its conjugate fault gives slightly better waveform fits. All of the shocks within the basement might have ruptured on structures that were generated during the rifting of the passive margin and became reactivated due to the current arc-continent collision.

The GPS displacements predicted from the slip models of the six aftershocks explain 80-percent of the post-seismic GPS signals near the aftershock region, strongly suggesting that large, shallow aftershocks contribute to post-seismic GPS signals. As a result, aftershock-induced post-seismic deformation needs to be included in interpretations of post-seismic deformation for the Chi-Chi, Taiwan sequence.

None of the aftershocks studied here resulted in observable surface rupture; all were the result of rupture on blind faults. These structures appear to be common in Taiwan and must be considered in regional seismic hazard studies, and the slip models derived from this study can be used to guide mapping of the active faults in Taiwan in the future. Currently other groups are using our slip models to study strong-motion attenuation for engineering purposes.

We have studied extensively how uncertainty or errors in the input source parameters deteriorate the waveform fits derived from the finite fault inversions. We found that for earthquakes with Mw ranging from 5.8 to 6.3, a hypocenter accuracy within 5 km will give at least 80% of the optimal waveform fits. For thrust events, a dip-angle accuracy within 20^{o} is required to generate 80% of the optimal waveform fits. But for strike-slip events, the accuracy of the strike is more important than that of dip angle. Rupture velocities depend strongly on the accuracy of the reported hypocenter location and the dip angle of the ruptured fault plane. The results of the sensitivity tests help in assessing the effects of

focal parameter errors on realtime application of finite-source inversion to forward predict near-fault strong ground motion (Dreger and Kaverina, 2000) as is now being undertaken to produce shakemaps.

We recommend that the remaining large aftershocks of the Chi-Chi earthquake and other Mw > 6 events in Taiwan should be studied using the method outlined here. Currently the strong motion data of at least 6 such events are available. The finite source processes of these earthquakes and full resolution and uncertainty analysis will help to establish a comprehensive stress perturbation model of Taiwan for the past few decades, following the approach of Stein (1999).

In summary, we have shown an increase in basement deformation from the subduction zone to the collision zone in the region offshore of Taiwan. Here, basement materials are brought to shallow depths through blind thrusts. These blind faults may pose significant seismic risk to the urban areas in Taiwan. In addition, the Chi-Chi mainshock ruptured in the vicinity of the proposed decollement, suggesting that the deformation on the trench side above the decollement can be approximated to a first order using the critical taper model. However, shallow crustal structures also might be modified by the seismogenic basement structures at depth, as suggested by the source models for the large Chi-Chi aftershocks.

Figure 6.1. The cross sectional structures of subduction zone, initial collision zone, and the collision zone in Taiwan regions derived from this study. From the results of reflection data and crustal density structures we found that the accretionary prism in the subduction zone is mostly sedimentary, but as the accretionary wedge evolves into initial collision, high-density materials are incorporated into the rear of the accretionary prism. In the collision zone on the trench side, we study the fault geometry derived from finite fault inversions of Chi-Chi, Taiwan earthquake sequence. The solid back beach balls are the moment tensors of some Chi-Chi aftershock sequence from Kao and Chen (2000). The fault planes or outline of aftershock slip are shown as solid colored lines. Each color represents one individual aftershock. The thick solid lines and the dashed lines are the interpreted aftershock slip regions with high and low confidence levels, respectively. The mainshock and 2 of the aftershocks ruptured near the vicinity of the decollement. One of those aftershocks (1999/09/20, 18:03, green-coded) matches with the result from recent reflection profile by Wang et al. (2002), shown on the upper left corner. Another aftershock ruptured downdip (1999/09/25, 23:52, magenta-coded). A strike slip aftershock (1999/9/20, 21:46, yellow-coded) ruptured within the basement but the major slip occurred above the decollement and is perpendicular to this cross section view. Three other slip models show strong evidence of ruptured in the basement or on a backthrust fault.

Collision Zone

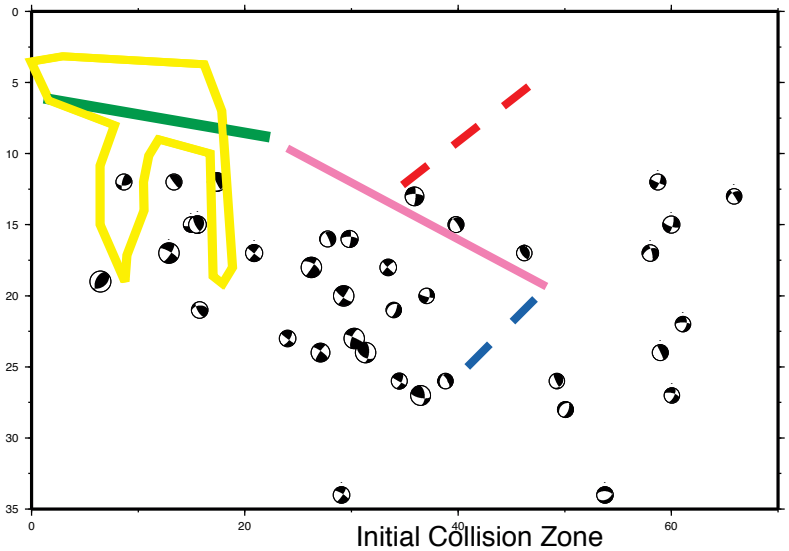

Initial Collision Zone

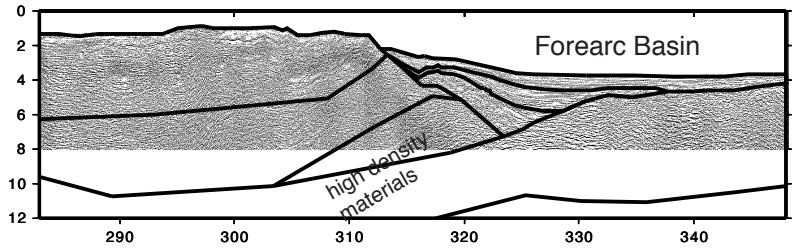

Subduction Zone

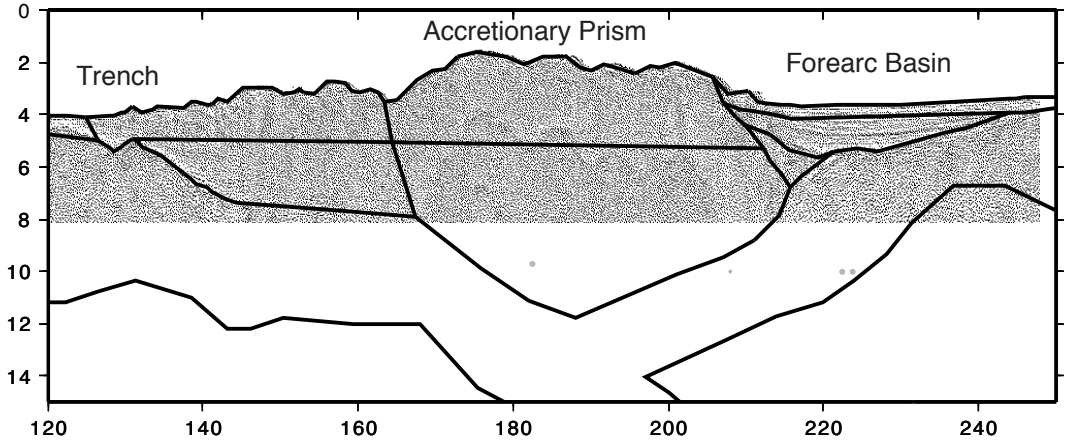

References:

Aki, K, and Richards, P.G., (1980) Quantitative seismology, 914 pp, W.H.Freeman & Co.

Anderson, R. N., DeLong, S., and Schwarz, W. M. (1978) Thermal model for subduction with dehydration in the downgoing slab: J. Geol., 86, 6, 731-739.

Angelier, J., Blanchet, R., Ho, C. S., and Le Pichon, X. (1984) Geodynamics of the Eurasia-Philippine Sea plate boundary: Tectonophysics, 125, ix-x.

Angelier, J., Chu, Hao-Tsu, and Lee, Jian-Cheng, (1997) Shear concentration in a collision zone; kinematics of the Chihshang Fault as revealed by outcrop-scale quantification of active faulting, Longitudinal Valley, eastern Taiwan: Tectonophysics, 274, 117-143.

Bauststa, B.C., Bautista, M.L.P., Oike, K., Wu, F.T., Punongbayan, R.S. (2001) A new insight on the geometry of subducting slabs in northern Luzon, Philippines: Tectonophysics, 339, 279-310.

Berndt, C., and Moore, G.F. (1999) Dependence of Multiple-attenuation techniques on the geologic setting: A case study from offshore Taiwan, The Leading Edge, 18, 1, 74-80.

Bowin, C., Lu, R.-S., Lee, C.-S., and Schouten, H. (1978) Plate convergence and accretion in Taiwan-Luzon region: American Association of Petroleum Geologists Bulletin, 62, 9, 1645-1672.

Bürgmann, Roland, S. Ergintav, P. Segall, E.H. Hearn, S.C. McClusky, R.E. Reilinger, H. Woith, J. Zschau, (2002) Time-dependent distributed afterslip

on and deep below the Izmit earthquake rupture, Bull. Seism. Soc. Am., 92, 126-137.

Byrne, T. (1998) Pre-collision kinematics and a possible modern analog for the Lichi and Kenting melanges, Taiwan, Journal of the Geological Society of China, 41(4), 535-550.

Byrne, T., and Crepsi, J. (1997a) Introduction to the Geology of Taiwan: field Guidebook for the International Conference and Sino-American Symposium on Tectonic of East Asia, 5-15.

Byrne, T., and Crepsi, J. (1997b) Kinematics of the Taiwan Arc-continent collision and implications for orogenic processes (abs.), International Conference and Sino-American Symposium on Tectonic of East Asia, p. 38.

CGS (1999) Special Report on Chi-Chi 921 Earthquake. Published by the Central Geological Survey of Taiwan, Dec. 1999, 315 pp. in Chinese.

Carena, Sara, John Suppe, and Honn Kao (2002) Active detachment of Taiwan illuminated by small earthquakes and its control of first-order topography, Geology (Boulder), 30(10), 935-938.

Central Geological Survey (2002) Geologic map of Taiwan, scale 1:500,000, Central Geological Survey, Ministry of Economic Affairs of Taiwan.

Chang, Chien-Hsin, Yi-Min Wu, Tzay-Chyn Chin, and Chien-Ying Wang (2000) Relocation of the 1999 Chi-Chi Earthquake in Taiwan, Terrestrial, Atmospheric and Oceanic Sciences (TAO), 11, 3, 581-590.

Chang, G., Y. M.Wu, and T. C. Shine (2000) Relocating the 1999 Chi-Chi Earthquake, Taiwan, Terrestrial, Atmospheric and Oceanic Sciences (TAO)

11, 581-590.

Chen, A. T., and Jaw, Y.-S. (1996) Velocity structure near northern Manila Trench; an OBS refraction study: Terrestrial, Atmospheric and Oceanic Sciences, 7, 3, 277-297.

Chen, A. T., and Nakamura, Y. (1998) Velocity structure beneath the eastern offshore region of Southern Taiwan based on OBS data: Terrestrial, Atmospheric and Oceanic Sciences (TAO), 9, 3, 409-424.

Chen, Kou-Cheng, Bor-Shouh Huang, Jeen-Hwa Wang, and Horng-Yuen Yen (2002) Conjugate thrust faulting associated with the 1999 Chi-Chi, Taiwan, earthquake sequence, Geophy. Res. Lett., 29(8), doi:10.1029/2001GL04250.

Cheng, W.B. (2000) Three-dimensional crustal structure around the source area of the 1999 Chi-Chi earthquake in Taiwan and its relation to the aftershock locations, Terrestrial, Atmospheric and Oceanic Sciences (TAO), 11, 643-660.

Cheng, Win-Bin, Wang, Chengsung, Shyu, Chuen-Tien, and Shin, Tzay-Chyn (1998) A Three-dimensional Vp Model of the Southeastern Taiwan Area and its Tectonic Implications: Terrestrial, Atmospheric and Oceanic Sciences (TAO), 9(3), 425-452.

Chi, W.-C., D. Dreger, W. Cheng, and S. Larsen (2000) Preliminary study of 3D structural effects on the ground shaking of the Taiwan Chi Chi earthquake, Eos Tran Am Geophys. U. 81, WP107.

Chi, Wu-Cheng and Doug Dreger (2002) Finite fault inversion of the September 25, 1999 (Mw=6.4) Taiwan Earthquake: Implications for GPS

displacements of Chi-Chi, Taiwan Earthquake sequence, Geophys. Res. Lett., 29(14), doi:10.1029/2002GL015237.

Chi, Wu-Cheng, D. Dreger (2001) and A. Kaverina, Finite-source modeling of the 1999 Taiwan (Chi-Chi) Earthquake derived from a dense strong-motion network, Bull. Seism. Soc. Am., 91, 1144-1157.

Chiu, H., and H. Huang (2000) Strong ground motions and earthquake damages observed from the Chi-Chi Earthquake, Eos Tran Am Geophys. U. 81, WP145.

Clark, M. B, D. Fisher, C.-Y. Lu, C.-H. Chen (1993) Kinematic analyses of the Hsuehshan Range, Taiwan; a large-scale pop-up structure Source, Tectonics, 12(1), 205-218.

Couzens, B. A., and Wiltschko, D. V. (1996) The control of mechanical stratigraphy on the formation of triangle zones: Bulletin of Canadian Petroleum Geology, 44(2), 165-179.

Crespi, J. M., Chan, Y.-C., and Swaim, M. S. (1996) Synorogenic extension and exhumation of the Taiwan hinterland: Geology (Boulder), 24(3), 247-250.

Davis, D., J. Suppe, and F.A. Dahlen (1983) Mechanics of fold-and-thrust belts and accretionary wedges, J. of Geophy. Res., 88, 1153-1172.

Dreger, D., and A. Kaverina (2000) Seismic remote sensing for the earthquake source process and near-source strong shaking: A case Study of the October 16, 1999 Hector Mine Earthquake, Geophysical Research Letters, 27(13), 1941-1944.

Fisher, D., Willett, S.D. (1998) Finite Strain, Kinematics and Wedge Dynamics of

Taiwan (abs.):Eos (Transactions, American Geophysical Union), 79, p. 918.

Flottmann, T, and Hand, M (1999) Folded basement-cored tectonic wedges along the northern edge of the Amadeus Basin, Central Australia: evalution of orogenic shortening, Journal of Structural Geology, 21, 399-412.

Freed, A.M., and J. Lin (2001) Delayed triggering of the 1999 Hector Mine earthquake by visocoelastic stress transfer, Nature, 411, 180-183.

Godfrey, N. J., Beaudoin, B. C., Klemperer, S. L., Levander, A., Luetgert, J., Meltzer, A., Mooney, W., and Trehu, A. (1997) Ophiolitic basement to the Great Valley forearc basin, California, from seismic and gravity data; implications for crustal growth at the North American continental margin: Geological Society of America Bulletin, v . 109(12), 1536-1562.

Guatteri, M., and P. Spudich (1998) Coseismic temporal changes of slip direction: The effect of absolute stress on dynamic rupture, Bull. Seism. Soc. Am., 88, 777-789.

Hacker, B. R. (1996) Eclogite formation and the rheology, buoyancy, seismicity, and H2O content of oceanic crust: Geophysical Monograph, 96, 337-346.

Hartzell, S.H., and T.H. Heaton (1983) Inversion of strong ground motion and teleseismic waveform data for the fault rupture history of the 1979 Imperial Valley, California, Earthquake, Bull. Seism. Soc. Am., 73, 1553-1583.

Hilde, T. W. C., and Lee, C. (1984) Origin and evolution of the West Philippine Basin; a new interpretation: Tectonophysics, 102, 85-104.

Hirata, Naoshi, Shin'ichi Sakai, Zen-Sen Liaw, Yi-Ben Tsai, and Shui-Beih Yu (2000) Aftershock observations of the 1999 Chi-Chi, Taiwan earthquake,

Bulletin of the Earthquake Research Institute, 75(1), 33-46.

Hirtzel, J. O. (1996) Evolution of a forearc basin in arc-continent collision, offshore Taiwan (Master's thesis thesis): San Jose State University. 41 p.

Hirtzel, J., Reed, D. L., Lundberg, N., and Liu, C. S. (1994) Seismic stratigraphic evolution of a forearc basin involved in arc-continent collision, offshore Taiwan(abs.):Eos (Transactions, American Geophysical Union), 75(44), F672.

Hsu, Shu-Kun, Liu, Char-Shine, Shyu, Shuen-Tien, Liu, Shao-Yung, Sibuet, Jean-Claude, Lallemand, Serge, Wang, Chengsung, and Reed, Don (1998) New Gravity and Magnetic anomaly maps in the Taiwan-Luzon region and their preliminary interpretation, Terrestrial, Atmospheric and Oceanic Sciences (TAO), 9(3), 509-532.

Hsu, Ya-Ju, Noa Bechor, Paul Segall, Shui-Beih Yu, Long-Chen Kuo, and Kuo-Fong Ma (2002) Rapid afterslip following the 1999 Chi-Chi, Taiwan Earthquake, Geophys. Res. Lett., 29(16), doi:10.1029/2002GL014967.

Hu, Jyr-Ching, Angelier, J., and Yu, Shui-Beih (1997) An interpretation of the active deformation of southern Taiwan based on numerical simulation and GPS studies, Tectonophysics, 274(1-3), 145-169.

Jachens, R.C., Griscom, A, and Roberts, C.W. (1995) Regional extent of Great Valley basement west of the Great Valley, California: Implications for extensive tectonic wedging in the California Coast Ranges, Journal of Geophysical Research, B, Solid Earth and Planets, 100(7), 12769-12790.

Jadoon, I. A. K., and Frisch, W. (1997) Hinterland-vergent tectonic wedge below

the Riwat Thrust, Himalayan foreland, Pakistan; implications for hydrocarbon exploration: American Association of Petroleum Geologists Bulletin, 81(3), 438-448.

Ji, Chen, Donald V. Helmberger, The-Ru Alex Song, Kuo-Fong Ma, David J. Wald (2001) Slip distribution and tectonic implication of the 1999 Chi-Chi, Taiwan, earthquake, Geophys. Res. Lett., 28(23), 4379-4382.

Kao, H and W.-P. Chen (2000) The Chi-Chi earthquake sequence: active, out-of-sequence thrust faulting in Taiwan, Science, 288, 346-2349.

Kao, Honn and Jacques Angelier (2001) The Chichi earthquake sequence, Taiwan: results from source parameter and stress tensor inversions, Sciences de la Terre et des Planetes (Earth and Planetary Sciences), 333(1), 65-80 (in French and English)

Kao, Honn, Huang, Gqo-Ching, Liu, Char-Shine (2000) Transition from oblique subduction to collision in the northern Luzon arc-Taiwan region: Constraints from bathymetry and seismic observations, J. Geophys. Res. 105, 3059-3080.

Kaverina, A., D. Dreger, and E. Price (2000) The combined inversion of seismic and geodetic data for the source process of the 16 October 1999 Mw 7.1 Hector Mine, California, earthquake, Bull. Seism. Soc. Am., 92(4), 1266-1280.

Kikuchi, Masayuki, Yuji Yagi, Yoshiko Yamanaka (2000) Source process of the Chi-Chi, Taiwan earthquake of September 21, 1999 inferred from teleseismic body waves, Bulletin of the Earthquake Research Institute,

75(1), 1-13.

Kuo, B.-Y., Liu, C. S., Jiang, S. T., Reed, D. L., and Lundberg, N. (1991) Crustal isostasy of the arc-continental collision zone in the southern offshore Taiwan: Bulletin of the Institute of Earth Sciences, Academia Sinica, 11, 68.

Lawson, C., and R. Hanson (1974) Solving Least Squares Problems, 337 pp., Prentice-Hall, Englewood Cliffs, N.J.

Lawton, D. C., Sukaramongkol, C., and Spratt, D. A. (1996) Seismic characterization of a "compound tectonic wedge" beneath the Rocky Mountain foreland basin, Alberta: Bulletin of Canadian Petroleum Geology, 44(2), 258-268.

Lee, Jian-Cheng, Angelier, J., and Chu, Hao-Tsu (1997) Polyphase history and kinematics of a complex major fault zone in the northern Taiwan mountain belt; the Lishan Fault: Tectonophysics, 274, 97-115.

Lee, S., K. Ma, J. Mori, and S. Yu (2000) Teleseismic and GPS data analysis of the 1999 Chi-Chi, Taiwan, Earthquake, Eos Tran Am Geophys. U. 81, WP105.

Lee, T.-Q., Kissel, C., Barrier, E., Laj C., and Chi, W.-R. (1991) Paleomagnetic evidence for a diachronic clockwise rotation of the Coastal Range, eastern Taiwan: Earth and Planetary Science Letters, 104(2-4), 245-257.

Lee, W. H.K., T.C. Shin, K.W. Kuo, K.C. Chen , and C.-F. Wu (2001) CWB free-field strong-motion data from the 21 September Chi-Chi, Taiwan, earthquake, Bull. Seism. Soc. Am., 91(5), 1370-1376.

Lee, W. H.K., T.C. Shin, K.W. Kuo, and K.C. Chen (1999) CWB free-field

strong-motion data from the 921 Chi-Chi Earthquake: Volume 1. digital acceleration files on CD-ROM, pre-publication Version (December 6, 1999), Seismology Center, Central Weather Bureau, Taipei, Taiwan.

Lieske, J., Jr., Lundberg, N., and Reed, D. L. (1992) Backthrusting in the submarine Taiwan orogeny; SeaMARC II and seismic reflection data: Acta Geologica Taiwanica, 30, 141-144.

Lin, C. (2000) Tectonic implication of both background seismicity and aftershocks of the 1999 Chi-Chi Earthquake, Eos Tran Am Geophys. U. 81, WP107.

Lin, C.-H., Yeh, Y.-H., Yen, H.-Y., Chen, K.-C., Huang, B.-S., Roecker, S. W., and Chiu, J.-M. (1998) Three-dimensional elastic wave velocity structure of the Hualien region of Taiwan; evidence of active crustal exhumation: Tectonics, 17, 1, 89-103.

Liu, C.-S., Lallemand, S. E., Lin, S.-J., Schnurle, P., and Reed, D. L. (1997) Forearc structures of the Ryukyu subduction-Taiwan collision zone from seismic reflection studies east of Taiwan(abs.):Eos (Transactions, American Geophysical Union), 78, F718.

Liu, Char-Shine, Liu, S. Y., Kao, Ban-Yuan, Lundberg, N., and Reed, D. L. (1992) Characteristics of the Gravity and Magnetic anomalies off southern Taiwan: Acta Geologica Taiwanica, 30, 123-130.

Liu, J.G., Lan, Ching-Ying, Suppe, John, and Ernst, W.G. (1977) The east Taiwan Ophiolite: Its occurrence, petrology, metamorphism and tectonic setting, Mining Research and Service Organization Special Report 1, Taipei,

Taiwan, ROC, 187 p.

Loevenbruck, Anne, Rodolphe Cattin, Xavier Le Pichon, Marie-Laure Courty, Shui-Beih Yu (2001) Seismic cycle in Taiwan derived from GPS measurements, Sciences de la Terre et des Planetes (Earth and Planetary Sciences), 333(1), 57-64 (in French and English)

Lu, C.-Y. and Jacques Malavieille (1994) Oblique convergence, indentation, and rotation tectonics in the Taiwan Mountain Belt: Insights from experimental modelling. Earth and Planetary Science Letters, 121(3-4), 477-497.

Lu, C.-Y., Angelier, J., Chu, H.-T., and Lee, J.-C. (1995) Contractional, transcurrent, rotational and extensional tectonics; examples from northern Taiwan: Tectonophysics, 246(1-3), 129-146.

Lu, Chia-Yu, Hao-Tsu Chu, Jian-Cheng Lee, Yu-Chang Chan, Kuo-Jian Chang, and Frederic Mouthereau (2002) The 1999 Chi-Chi Taiwan earthquake and basement impact thrust kinematics, Western Pacific Earth Sciences, 29(2), 181-190.

Lundberg, N., Reed, D. L., Liu, Char-Shine, and Lieske, J., Jr. (1997) Forearc-basin closure and arc accretion in the submarine suture zone south of Taiwan: Tectonophysics, 274, 5-23.

Lundberg, Neil (1992) Structural controls on orogenic sedimentation, submarine Taiwan collision, Acta Geologica Taiwanica, 30, 131-140.

Ma, K., and J. Mori (2000) Rupture process of the 1999 Chi-Chi, Taiwan Earthquake from direct observations and joint inversion of strong motion, GPS and teleseismic data, Eos Tran Am Geophys. U. 81, WP104.

Ma, Kuo-Fong, The-Ru The, Shiann-Jong Lee, and Hsiang-I Wu (2000) Spatial slip distribution of the September 20, 1999, Chi-Chi, Taiwan, earthquake (Mw 7.6); inverted from teleseismic data, Geophys. Res. Lett., 27(20), 3417-3420.

Ma, Kuo-fong, Jim Mori, Shiann-Jong Lee, and Shui-Beih Yu (2001) Spatial and temporal distribution of slip for the 1999 Chi-Chi, Taiwan, earthquake, Bull. Seism. Soc. Am., 91(5), 1069-1087.

Malavieille, J., Lallemand, S.E., Dominguez, S., Deschamps, A., Lu, Chia-Yu, Liu, Char-Shine, Schnurle, P., and the ACT Scientific Crew (2003) Geology of the Arc-Continent Collision in Taiwan: Marine Observations and Geodynamic Model, Bull. Geol. Soc. Am., in press.

Mitra, S., and Mount, V.S. (1998) foreland Basement-involved structures, American Association of Petroleum Geologists, 82(1), 70-109.

Moore, G.F., Taylor, B., Zhao, Z., Chi, W.-C., Reed, D.L., Lundberg, N., Liu, C.S. (1997) Structure of the China margin southwest of Taiwan form new multichannel seismic reflection data(abs.):Eos (Transactions, American Geophysical Union), 78, F658.

Mori, J. and K.-F. Ma (2000) Slip velocity estimates of the 1999 Chi-Chi, Taiwan Earthquake: New observations of fault dynamics, Eos Trans. AGU, U. 81, WP140.

Nakamura, Y., McIntosh, K., Wang, T. K., and Chen, A. T. (1996) Large offset offshore reflection/refraction data show detailed structure of transitional crust subducting underneath southern Taiwan(abs.):Eos (Transactions,

American Geophysical Union), 77, 46, F719.

Nguyen, T.A., Reed, D.L., Chi, Wu-Cheng (1998) New insights into forearc processes within the subduction-related portion of the offshore Taiwan Accretionary Prism, (abs.):Eos (Transactions, American Geophysical Union), 79, F45,887.

Okada, Y. (1992) Internal deformation due to shear and tensile faults in a half-space, Bull. Seism. Soc. Am., 82, 1018-1040.

Price, R. (1986) The southeastern Canadian Cordillera: Thrust faulting, tectonic wedging and delamination of the lithosphere, Journal of Structural Geology, 8, 3-4, 239-254.

Rau, R.-J. , and F. Wu (1995) Tomographic imaging of lithospheric structures under Taiwan, Earth and Planetary Science Letters, 133, 517-532.

Rau, R.-J. and F. Wu (1998) Active tectonics of Taiwan Orogeny from focal mechanisms of small-to-moderate-sized earthquakes, Terrestrial, Atmospheric and Oceanic Sciences (TAO), 9(4), 755-778.

Reed, D. L., Chi, Wu-Cheng, Lundberg, N., Liu, Char-Shine, Stennis, S., and Chuang, F. (1994) The offshore Taiwan accretionary prism; implications for regional and focused fluid flow, in Geological Society of America, 1994 annual meeting, Seattle, WA, USA, p. 271.

Reed, D. L., Chi, Wu-Cheng, Moore, G. F., Berndt, C., Zhao, Z., Lundberg, N., Nakamura, Y., McIntosh, K., and Liu, C. S. (1996) TAICRUST; imaging forearc deformation during arc accretion (abs.):Eos (Transactions, American Geophysical Union), p. 719.

Reed, D. L., Lundberg, N., Liu, Char-Shine, and Kuo, B.-Y. (1992) Structural relations along the margins of the offshore Taiwan accretionary wedge; implication for accretion and crustal kinematics: Acta Geologica Taiwanica, 30, 105-122.

Reed, D. L., and Silver, E. A. (1995) Sediment dispersal and accretionary growth of the North Panama deformed belt: Special Paper Geological Society of America, 295, 213-223.

Reed, D.L., Lundberg, N., Chi, Wu-Cheng, Silver, E.A., Liu, C.-S., Moore, G.F. (1999) Modern arc-continent collisions of the pacific rim: Implications for the development and demise of forearc basins, in in Geological Society of America, 1999 annual meeting, Berkeley, CA , USA, p. A-87.

Roering, J. J., Cooke, M. L., and Pollard, D. D. (1997) Why blind thrust faults do not propagate to the Earth's surface; numerical modeling of coseismic deformation associated with thrust-related anticlines: Journal of Geophysical Research, B, Solid Earth and Planets, 102(6), 11,901-11,912.

Saikia, C.K. (1994) Modified frequency-wave-number algorithm for regional seismograms using Filon's quadrature-modeling of L(g) waves in eastern North America, Geophys. J. Int., 118, 142-158.

Silver, E. A., Abbott, L., Kirchoff-Stein, K. S., Reed, D., and Bernstein, B. (1990) Collision propagation in Papua New Guinea and Solomon Sea, in Fifth Circum-Pacific Energy and Mineral Resources Conference, Honolulu, HI, USA, p. 1001.

Silver, E.A., and Reed, D. (1988) Backthrusting in accretionary wedges, Journal

of Geophysical Research, 93(4), 3116-3126.

Sommerville, P, K. Irikura, R. Graves, S. Sawada, D. Wald, N. Abrahamson, Y. Iwasaki, T. Kagawa, N. Smith, and A. Kowada (1999) Characterizing crustal earthquake slip models for the prediction of strong ground motion, Seism. Res. Lett., 70(1), 59-80.

Stein, R. (1999) The role of stress transfer in earthquake occurrence, Nature, 403(6762), 605-609.

Suppe, J. (1981) Mechanics of mountain-building and metamorphism in Taiwan: Memoir of the Geological Society of China, 4, 67-89.

Suppe, John, (1984) Kinematics of arc-continent collision, flipping of subduction, and back-arc spreading near Taiwan: Memoir of the Geological Society of China, 6, 21-33.

Suppe, John (1984) Seismic interpretation of the compressively reactivated normal fault near Hsinchu, western Taiwan, Petroleum Geology of Taiwan, 20, 85-96.

Suppe, J., (1988) Tectonics of arc-continent collision on both sides of the South China Sea: Taiwan and Mindoro, Acta Geologica Taiwanica, 26, 1-18.

Suppe, J., Sabat, F., Munoz, J. A., Poblet, J., Roca, E., and Verges, J. (1997) Bed-by-bed fold growth by kink-band migration; Sant Llorenc de Morunys, eastern Pyrenees: Journal of Structural Geology, 19, 443-461.

Tang, J.-C. and Chemenda, A.I. (2000) Numerical modeling of arc-continent collision: application to Taiwan, 325, 23-42.

Taylor, B., and Hayes, D. E., (1980) The tectonic evolution of the South China

Basin: Geophysical Monograph, 23, 89-104.

Teng, L. S. (1990) Tectonic evolution of late Cenozoic arc-continent collision in Taiwan: American Association of Petroleum Bulletin, 74(6), 1004-1005.

Torrini, R., Jr., and Speed, R. C. (1989) Tectonic wedging in the forearc basin-accretionary prism transition, Lesser Antilles forearc: Journal of Geophysical Research, B, Solid Earth and Planets, 94(8), 10,549-10,584.

Turcotte, D. L., and Schubert, G. (1982) Geodynamics: applications of continuum physics to geological problems, 450 pp, New York, NY, USA, John Wiley & Sons.

Unruh, J. R., Loewen, B. A., and Moores, E. M. (1995) Progressive arcward contraction of a Mesozoic-Tertiary forearc basin, southwestern Sacramento Valley, California, Geological Society of America, 107(1), 38-53.

Wakabayashi, J., and Unruh, J. R. (1995) Tectonic wedging, blueschist metamorphism, and exposure of blueschists; are they compatible? Geology (Boulder), 23(1), 85-88.

Wald, D., T.H. Heaton, and K.W. Hudnut (1996) The slip history of the 1994 Northridge, California, Earthquake determined from strong-motion, teleseismic, GPS, and Leveling Data, Bull. Seism. Soc. Am., 86, 49-70.

Wald, David J., V. Quitoriane, T.H. Heaton, H. Kanamori, C.W. Scrivner, and C.B. Worden (1999) TriNet ``ShakeMaps": Rapid Generation of Instrumental Ground Motion and Intensity Maps for Earthquakes in Southern California, Earthquake Spectra, 15(3), 537-556.

Utilization of the Internet for rapid community intensity maps, Seism. Res. Lett.,

70(6), 680-693.

Wang, Chien-Ying, Chien-Li Li, Fu-Chen Su, Ming-Tar Leu, Ming-Shan We, Shao-Huei Lai, and Chir-Cherng Chern (2002) Structural mapping of the 1999 Chi-Chi earthquake fault, Taiwan by seismic reflection methods, TAO, 13(3), 211-226.

Wang, Wei-Hau and Chau-Huei Chen (2001) Static stress transferred by the 1999 Chi-Chi, Taiwan, earthquake; effects on the stability of the surrounding fault systems and aftershock triggering with a 3D fault-slip model, Bull. Seism. Soc. Am., 91(5), 1041-1052.

Ward, S.N. (2000) San Francisco Bay Area earthquake simulations: A step toward a standard physical earthquake model, Bull. Seism. Soc. Am. 90(2), 370-386.

Wentworth, C. M., Blake, M. C., Jr., Jones, D. L., Walter, A. W., and Zoback, M. D., (1984) Tectonic wedging associated with emplacement of the Franciscan assemblage, California Coast Ranges: Field Trip Guidebook Pacific Section, Society of Economic Paleontologists and Mineralogists, 43, 163-173.

Westbrook, G. K., Ladd, J. W., Buhl, P., Bangs, N., and Tiley, G. J. (1988) Cross section of an accretionary wedge; Barbados Ridge Complex: Geology (Boulder), 16(7), 631-635.

Willett, S.D., Hovius, N. (1998) Active Exhumation in Taiwan, Extension or Erosion? (abs.):Eos (Transactions, American Geophysical Union), 79, F918.

Willett, Sean D (1999) Rheological dependence of extension in wedge models of

convergent orogens, Tectonophysics, 305(4), 419-435.

Wu, C, M. Takeo, and S. Ide (2000) Source process of the Chi-Chi Earthquake, Eos Tran Am Geophys. U. 81, WP104.

Wu, C, M. Takeo, and S. Ide (2001) Source process of the Chi-Chi earthquake: a joint inversion of strong motion data and Global Positioning System data with a multifault model, Bull. Seism. Soc. Am., 91(5), 1128-1143.

Wu, F.T. and R.-J. Rau (1998) Seismotectonics and identification of potiontial seismic source zones in Taiwan, Terrestrial, Atmospheric and Oceanic Sciences (TAO), 9(4), 739-754.

Yagi, Y and M. Kikuchi (1999) Preliminary results of rupture process for the September 21, 1999 Chi -Chi Earthquake, URL: http://wwweic.eri.u-tokyo.ac.jp/yuji/taiwan/taiwan.html.

Yagi, Y and M. Kikuchi (2000) Source rupture process of the Chi-Chi, Taiwan, Earthquake of 1999, obtained by seismic wave and GPS data, Eos Trans. AGU, 81, WP104.

Yu, Shui-Beih, Chen, Horng-Yue, and Kuo, Long-Chen (1995) Velocity field of GPS stations in the Taiwan area: Tectonophysics, 274, 41-59.

Yu, Shui-Beih, Long-Chen Kuo, Ya-Ju Hsu, Hsuan-Han Su, Chi-Ching Liu, Chin-Shyong Hou, Jiin-Fa Lee, Teng-Chang Lai, Chih-Chung Liu, Cheng-Lun Liu, Teh-Fu Tseng; Chun-Shyong Tsai, and Tzay-Chyn Shin (2001) Preseismic deformation and coseismic displacements associated with the 1999 Chi-Chi, Taiwan, earthquake, Bull. Seism. Soc. Am., 91(5), 995-1012.

Zeng, Yeuhua and Chau-Huei Chen (2001) Fault rupture process of the 20

September 1999 Chi-Chi, Taiwan, earthquake, Bull. Seism. Soc. Am., 91(5), 1088-1098.